FUNDAMENTAL UNDERSTANDING OF THE UNSTEADY AERODYNAMICS OF CYCLOIDAL ROTORS IN HOVER AT ULTRA-LOW REYNOLDS NUMBERS

A Thesis

by

CAROLYN MARIE WALTHER

Submitted to the Office of Graduate and Professional Studies of
Texas A&M University
in partial fulfillment of the requirements for the degree of

MASTER OF SCIENCE

Chair of Committee,	Moble Benedict
Committee Members,	Thomas Strganac
	Gerald Morrison
Head of Department,	Rodney Bowersox

August 2017

Major Subject: Aerospace Engineering

ABSTRACT

This thesis provides a fundamental understanding of the unsteady aerodynamic phenomena on a cycloidal rotor blade operating at ultra-low Reynolds numbers (Re~18,000) by utilizing a combination of experimental (force and flowfield measurements) and computational (CFD) studies. For the first time ever, the instantaneous blade fluid dynamic forces on a rotating cyclorotor blade were measured, which, along with PIV-based flowfield measurements revealed the key fluid dynamic mechanisms acting on the blade. A 2D CFD analysis of the cycloidal rotor was developed and systematically validated using both force and flowfield measurements. Studies were performed with static pitching, and dynamic blade pitching for symmetric and asymmetric kinematics. Direct comparison of the static and dynamic pitch experimental results helped isolate the unsteady phenomena (such as dynamic stall, unsteady virtual camber, etc.) from the steady effects.

The dynamic blade force coefficients for symmetric pitching were almost double the static ones, clearly indicating the role of unsteady mechanisms on force production on cyclorotor blades. The blade lift monotonically increased even up to ±45° pitch amplitude due to dynamic stall phenomenon; however, as expected, for the static case, the flow separated from the leading edge after around 15° with a large laminar separation bubble (LSB) and eventually completely separated at higher pitch angles. For both static and dynamic pitching cases, there was significant asymmetry in the lift and drag coefficients between positive and negative pitch angles due to the flow curvature effects (virtual

camber). CFD flow solution and PIV measured flowfield correlated well, and both showed the formation and shedding of strong dynamic stall or leading edge vortices, especially at higher pitch amplitudes, which is the reason for the stall delay and force enhancement. Also, the dynamic stall process for symmetric and asymmetric pitching during the upper half of the trajectory was significantly different from the lower half even with symmetric blade pitch kinematics because of the reversal of dynamic virtual camber from the upper to the lower half. Even at such low Reynolds numbers the pressure forces, as opposed to viscous forces, were found to be dominant on the cyclorotor blade. The power required for rotation (rather than pitching power) was the domineering component of the total blade power for the dynamic pitching case. For asymmetric pitching, implementing higher pitch at the top and lower pitch at the bottom could counteract the inherent virtual camber effect and significantly improve the performance of a cyclorotor. CFD and the experimental forces and flowfield correlated well for asymmetric pitching, but there were some differences in the lower half where CFD seemed to overpredict the forces for reasons yet to be identified. The Reynolds number affects the dynamic stall processes and the forces produced by the blades.

DEDICATION

I would like to dedicate this thesis to my mom and dad, sister, and fiancé. My mom and dad have loved and supported me through all my endeavors. They have inspired me to work hard and step outside of my comfort zone. My sister, Rachel, has been such a good friend through some of the hardest times, and has always provided words of affirmation and encouragement when most needed. Finally, to my fiancé, Levi, I am especially grateful. He has been at my side during some of the toughest times of graduate school, and provided me great joy in even the most stressful moments.

All in all, I would not be where I am today without these people, and they will always hold a dear place in my heart. I love you all very much.

ACKNOWLEDGEMENTS

I would like to thank my committee chair, Dr. Benedict, and my committee members, Dr. Strganac and Dr. Morrison, for their guidance and support throughout the course of this research.

Thanks also go to my friends and colleagues, and the department faculty and staff for making my time at Texas A&M University a great experience. In particular, I would like to thank David Coleman, Farid Saemi, and Atanu Halder for their contributions to the project. David was very helpful when I first arrived at the Advanced Vertical Flight Lab by patiently teaching me how to operate the lab equipment, and serving as a mentor for academic endeavors in general. Farid served tirelessly by troubleshooting and assembling the electronics on the experimental setup, even with the many undergraduate classes he was taking; he will do an excellent job as he moves into academia as a graduate student. Atanu was extremely helpful with the dynamic virtual camber aspect of the study; he helped perform several of the computations that are presented in Chapter III.

CONTRIBUTORS AND FUNDING SOURCES

This work was supervised by a thesis committee consisting of Professor Benedict (chair) and Professor Strganac of the Department of Aerospace Engineering and Professor Morrison of the Department of Mechanical Engineering.

The CFD results in Chapter IV and Chapter V were provided by Vinod Lakshminarayan of the Science and Technology Corporation at Ames Research Center. All other work conducted for the thesis was completed by the student independently.

This research was supported by the U.S. Army's Micro Autonomous Systems and Technology–Collaborative Technology Alliance (MAST-CTA) with Chris Kroninger as Technical Monitor.

NOMENCLATURE

A	Rectangular projected rotor area
b	blade span
AR	Aspect ratio
c	Blade chord length
C_L	Coefficient of lift
C_D	Coefficient of drag
C_{MZ}	Pitching moment coefficient
C_P	Power coefficient
C_T	Thrust coefficient
d	Cyclorotor diameter
D	Drag force
FM	Figure of merit
L	Lift force
LE	Leading edge of blade
M_Z	Pitching moment
PIV	Particle image velocimetry
P_{IDEAL}	Ideal power
P_{PITCH}	Pitching power
P_{ROT}	Rotational power
P_{TOTAL}	Total power

R	Rotor radius
T	Thrust
TE	Trailing edge of blade
v_i	Induced velocity
β	Angle between chord and resultant force
Ω	Rotational speed of rotor
φ	Phase angle
Ψ	Azimuthal position of blade
θ	Blade pitch angle
$\dot{\theta}$	Blade pitch rate

TABLE OF CONTENTS

Page

Page

LIST OF FIGURES

Page

Page

Page

CHAPTER I

INTRODUCTION AND LITERATURE REVIEW

The development of efficient, maneuverable, gust tolerant, and sustained hover-capable micro air vehicle (MAV) platforms with expanded flight envelope is the key to the success of many missions in both military and civilian scenarios. In a military setting, MAVs can be used to perform reconnaissance missions by surveying enemy forces or dangerous areas, all the while remaining undetected and sparing a human life. For civilian applications, MAVs can be adapted to assist with fire and rescue missions, border surveillance, aerial photography, traffic monitoring, and many other scenarios.

During the past decade, there have been many studies on the experimental optimization of MAV-scale conventional rotors (Refs. 1 and 2). These studies helped improve the hover figure of merit of a micro-rotor from an initial value of 0.42 to 0.65. However, this maximum figure of merit is still far below the full-scale helicopter value (~0.85) and is attributed to low Reynolds number (10^4–10^5) aerodynamics, especially the low airfoil lift-to-drag ratios and the complex induced wake distribution below the rotor (Ref. 2). Therefore, the vehicles developed using these optimized rotors could only achieve a maximum hover endurance of 10 minutes which would make them incapable of any realistic missions (Refs. 1 and 2). This clearly indicates the need for a step improvement in hover efficiency, which could only be achieved through a radically different concept to fly at these low Reynolds numbers.

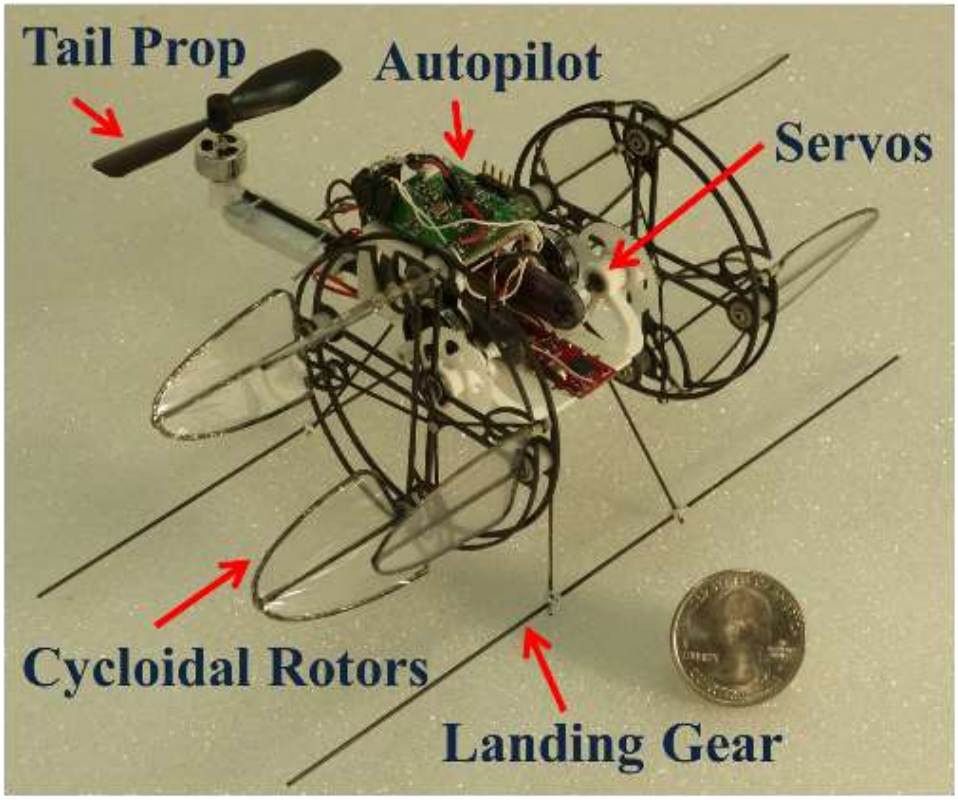

Fig. 1: 29-gram meso-scale cyclocopter.

A new revolutionary concept of a cyclocopter or a cycloidal rotor based aircraft (Fig. 1) is being investigated. A cycloidal rotor (or cyclorotor) is a rotating-wing system (Fig. 1) where the span of the blades runs parallel to the axis of its rotation. The pitch angle of each blade is varied cyclically by mechanical means such that each blade experiences positive geometric angles of attack at both the top and bottom halves of its circular trajectory (Fig. 2). The resulting time-varying lift and drag forces produced by each blade is resolved into the vertical and horizontal directions, as shown in Fig. 2. With this kind of cyclic blade kinematics, the blades produce a net thrust. Varying the amplitude

and phase of the cyclic blade pitch is used to change the magnitude and direction of the net thrust vector produced by the cyclorotor.

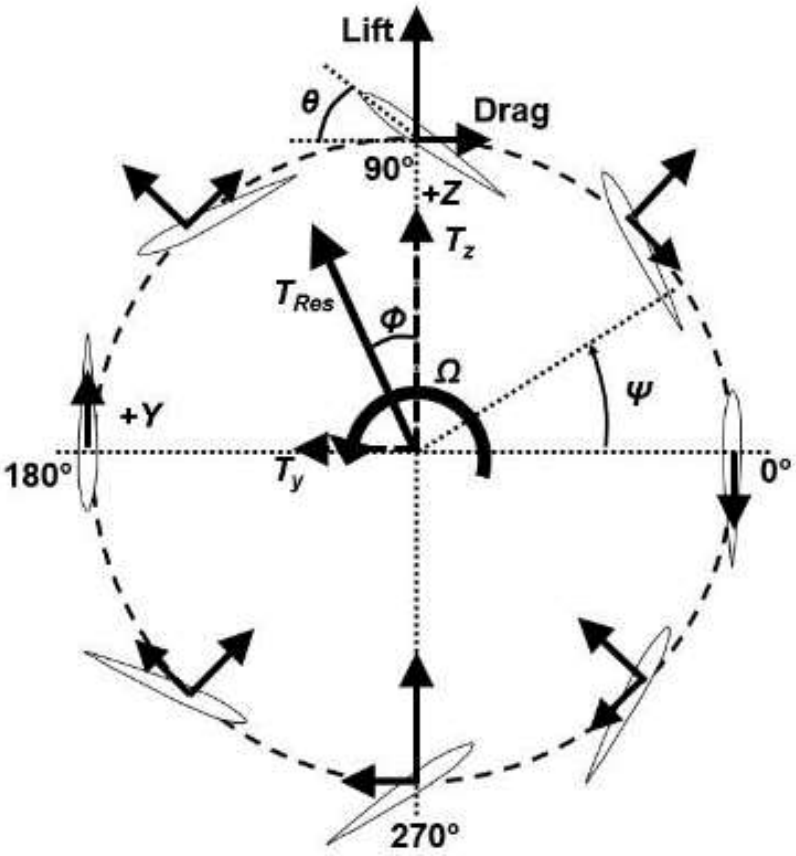

Fig. 2: Cyclorotor blade kinematics.

Pioneering research on the cyclorotor concept for micro air vehicle (MAV) applications has been conducted over the last ten years (Ref. 3 – 15). This body of work represents one of the most comprehensive evaluations ever conducted on cyclorotors at MAV scales and involved systematic performance measurements in both hover (Ref. 3 –

7) and in a wind tunnel (Refs. 8 – 10), flowfield studies using Particle Image Velocimetry (PIV) (Refs. 3 – 5), computational fluid dynamic (CFD) analysis (Refs. 8 and 9), and aeroelastic modeling (Ref. 11). These studies established a fundamental understanding of a cyclorotor's performance, and helped in formulating a set of design principles for an efficient cyclorotor operating at MAV-scale Reynolds numbers (Re<40,000).

Benedict performed extensive research on hover-capable MAVs though both experiments and analysis (Ref. 3). The experimental work consisted of both performance and flowfield measurements, and the analysis conducted was an unsteady aeroelastic analysis to predict the average aerodynamic performance and blade loads of a cyclorotor (Ref. 3). Systematic performance measurements resulted in the identification of an optimized cyclorotor, and the aeroelastic analysis emphasized the influence that blade pitch kinematics, unsteady aerodynamics and blade deflections have on blade loads (Ref. 3).

In Ref. 4 an optimized cyclorotor configuration was obtained through systematic experimental parametric studies. This study investigated the effects of rotational speed, amplitude of blade pitch, blade airfoil profile, and blade flexibility on cyclorotor performance, and PIV studies were conducted to gain understanding of the flowfield around the cyclorotor (Ref. 4). They found that a cyclorotor generates high values of thrust at very high blade pitch amplitudes. The PIV flowfield showed a pitch-rate induced stall delay on the blades at high pitch angles, and the formation of a leading edge vortex similar to a dynamic stall vortex which can increase the amount of thrust produced.

Further work on improving the aerodynamic performance of cyclorotors was performed by Benedict, Ramasamy, and Chopra (Ref. 5). They conducted more detailed parametric and flowfield studies, and found that power loading and rotor efficiency can be increased by using more blades (Ref. 5). The study showed that regardless of the number of blades used, a cyclorotor's performance improves at higher blade pitch angles (Ref. 5). The PIV measurements showed significant rotational flows inside the rotor, and wake interactions between the upper and lower halves of the rotor (Ref. 5). A key inference from this study was that blade camber and optimized blade kinematics, such as asymmetric pitching, can help mitigate the losses (Ref. 5).

Benedict, Jarugumilli, and Chopra performed additional parametric studies and compared the performance of a cyclorotor with a conventional rotor (Ref. 6). They found that an optimized cyclorotor has significantly higher power loading (almost 50% higher) when compared to a conventional rotor (Fig. 3) operating at the same disk loading (Ref. 6). The possible reasons for the improved performance could be the uniform spanwise load distribution on the cyclorotor blades and the favorable unsteady aerodynamic mechanisms. The parametric studies also involved an investigation into the dependence of a cyclorotor's performance on blade pitching amplitude for both symmetric and asymmetric pitching (Ref. 6). It was found that the power loading was higher for an asymmetric pitching case where the pitch angle was higher at the top than the bottom, when compared to symmetric pitching (Ref. 6). The highest power loading case was for a total peak-to-peak pitching angle of 70°, with a 45° pitch angle at the top and a 25° pitch angle at the bottom (Ref. 7). They also found that by shifting the pitching axis location

away from the leading edge, the performance improved (Ref. 7). For rotors with large chord-to-radius ratio in general, asymmetry in pitch angle and location of pitching axis significantly affect the aerodynamic performance due to flow curvature effects (virtual camber from curvilinear flow) (Ref. 7).

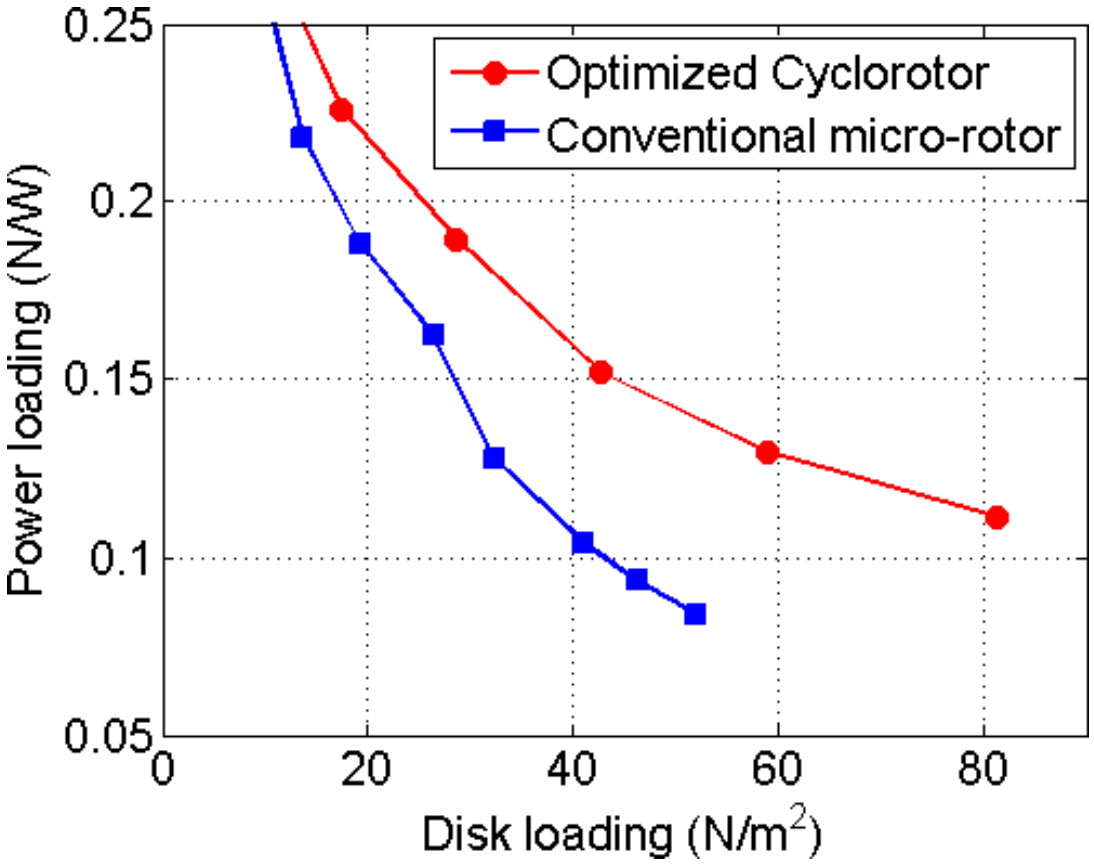

Fig. 3: Thrust/power of cyclorotor versus conventional rotor. (Ref. 6)

Systematic forward flight studies were also performed on a cyclorotor in an open-jet wind tunnel, where the pitching axis location and chord-to-radius radio were varied

(Ref. 8). One goal of these studies was to understand the effect that these parameters have on virtual camber (Ref. 8). Virtual camber is highly dependent on the two parameters, and is a key factor which affects the lift, thrust, and power consumed for a pitching blade (Ref. 8). It was shown that increasing the chord-to-radius ratio (which increases the virtual camber) and pitching the blade closer to the leading edge will increase the lift per unit area in a mostly linear fashion for constant rotational speed and wind speed (Ref. 8).

The forward flight studies also utilized a combination of time-resolved PIV measurements, time-averaged force measurements, and 2D CFD predicted flowfield to understand the flow physics for a cyclorotor (Ref. 9). Observations from the measured flowfield were compared with CFD predicted instantaneous forces and power to identify the role of periodic flow features in lift generation (Ref. 9). It was found that the upper half of the rotor experiences a region of power extraction, which is seen in the time-averaged flowfield where the magnitude of the flow velocity decreases (Ref. 9). This extraction region also appeared in the 2D CFD predicted instantaneous power (Ref. 9).

Forward flight studies conducted by Jarugumilli, Benedict, and Chopra involved an investigation into the effects of blade pitch amplitude and pitch phase angle on rotor lift, power, and propulsive force (Ref. 10). These studies provided a fundamental understanding of cyclorotor performance in steady and level flight (Ref. 10). For the maximum forward speed tested (13 m/s), the rotor operated at 1740 RPM (advance ratio = 0.94), and maintained sufficient lift for the twin-cyclocopter MAV used in the study (Ref. 10). In Fig. 4, one can see that the power required decreased by almost 40% from

hover to an advance ratio close to unity, which is remarkable for an MAV-scale rotor (Ref. 10).

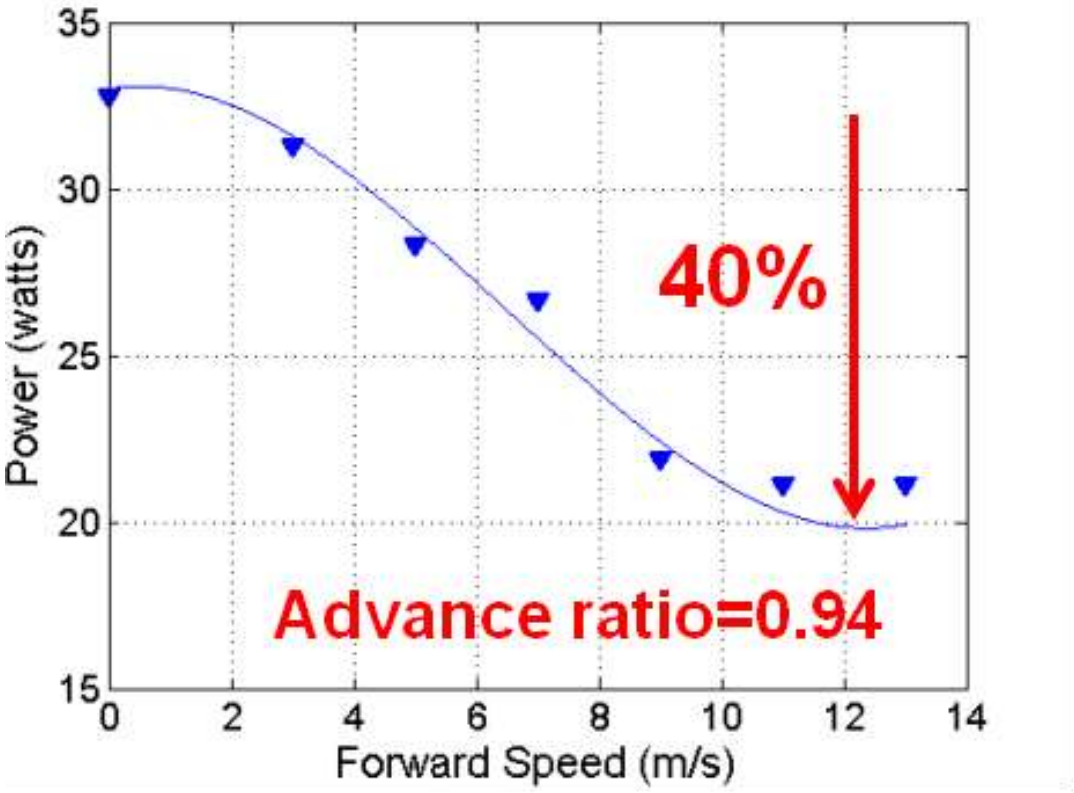

Fig. 4: Forward flight performance of a cyclorotor. (Ref. 10)

In another study conducted by Benedict, Chopra, Mattaboni, and Masarati, an aeroelastic model was used to predict the blade loads and averaged thrust of a MAV-scale cyclorotor (Ref. 11). The model utilized a beam-based finite element analysis with radial bending, tangential bending, and torsional degrees of freedom, and a multibody based

analysis for large deformations (Ref. 11). The goal of the study was to understand the effect of unsteady aerodynamics, blade kinematics, and blade flexibility on cyclorotor performance (Ref. 11). A key conclusion from the study was the need for a coupled aeroelastic analysis for predicting blade loads on a cyclorotor with flexible blades (Ref. 11). Blade deformations are influenced mainly by inertial forces, but aerodynamic forces still have a significant impact on them (Ref. 11). It was also found that lateral forces produced by a cyclorotor blade are due to mechanical lag in the blade kinematics and aerodynamic phase lag from the unsteady aerodynamics (Ref. 11).

This work, along with innovative vehicle design techniques and the development of novel autonomous flight control strategies, led to the first flying cyclorotor-based aircraft (Ref. 12). Benedict, Gupta, and Chopra designed, built, and successfully flight tested a twin-rotor cyclocopter in hover; this was the first stable flight of an untethered cyclocopter reported in literature (Ref. 12). The cyclocopter used a lightweight cyclorotor design that produced three times more thrust than its own weight (Ref. 12). The cyclorotor utilized a novel blade pitching mechanism that allowed for instantaneous thrust vectoring though phasing of the cyclic pitch with a servo and linkage system (Ref. 12).

Since this milestone, a wide range of hover-capable cyclorotor aircraft ranging in size from 29 to 800 grams were developed (Refs. 12 – 15), demonstrating conclusively the feasibility of the cyclorotor concept for MAV applications (Figs. 1 and 5).

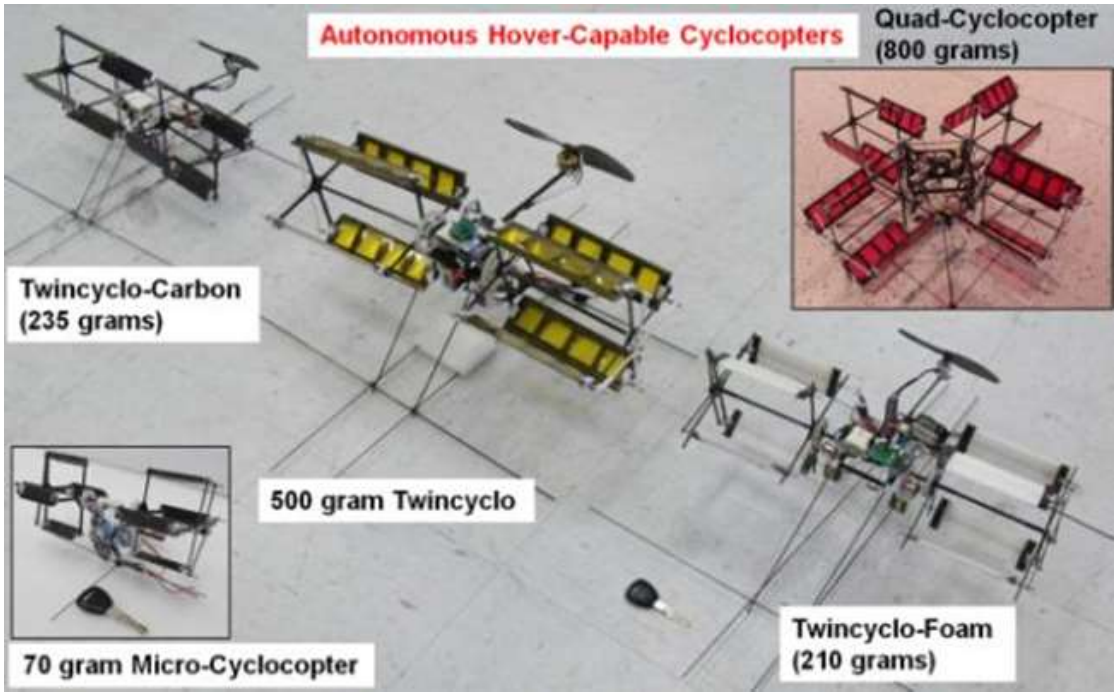

Fig. 5: Hover-capable cyclocopters developed in the past. (Refs. 12-15)

Further research focused on expanding the flight envelope of the cyclocopter to stable, high-speed, and level forward flight (Ref. 13). Forward flight control strategies were developed using independent pitch phasing and cyclorotor rotational speed control without relying on additional control through a traditional empennage system (Ref. 13). Although the cyclocopter is inherently unstable, a proportional-derivative (PD) controller for a feedback control system was developed and can successfully stabilize the vehicle (Ref. 13). It was found that phasing the cyclic pitch angle, which tilts the cyclorotor thrust vector, provides enough change in the propulsive force to increase forward flight speed (Ref. 13). Therefore, instead of pitching the vehicle forwards, tilting the cyclorotor thrust vector provides complete control authority of the forward velocity (Ref. 13).

Another study performed by Benedict, Mullins, Hrishikishavan, and Chopra detailed the vehicle design, control system development, and autonomous hover flight testing of a cyclocopter with a quad-rotor configuration using four cyclorotors in an axi-symmetric plus-shaped orientation where each rotor axis was orthogonal to its neighbor (Ref. 14). Each cyclorotor had independent rotational speed control and thrust vectoring capability, and the control strategy was implemented on a 3-gram autopilot which autonomously stabilized the vehicle using a feedback PD controller (Ref. 14).

Much of the prior research utilized a linkage pitching mechanism to actuate the blade kinematics in hover. Another mechanism was developed that used the pitching moment from the centrifugal force to pitch the blades along with a novel cam design to achieve the desired pitch kinematics (Ref. 15). A twin-rotor cyclocopter instrumented with this mechanism was designed and built by Adams, Benedict, Hrishikishavan, and Chopra (Ref. 15). Their experiments demonstrated that the new pitching mechanism could be adapted to generate cyclic pitching schedules needed for different advance ratios by altering the cam profile (Ref. 15). The mechanism was designed to actively vary the pitch amplitude and phasing during flight by translating the cam in orthogonal directions (Ref. 15). Through this study, the first flight-capable cyclocopter with cyclorotors having control over pitch amplitude and phase was reported in literature (Ref. 15).

It has been shown that a cyclorotor is more aerodynamically efficient than a conventional rotor at the same disk loading, and has benefits such as instantaneous thrust vectoring capability and the ability to transition from hover to high-speed forward flight seamlessly. There are several other advantages to a cyclorotor-based aircraft. For instance,

a twin-rotor cyclocopter (Fig. 1) has 5 control degrees of freedom (three RPMs and two thrust directions) (Refs. 13). As a result, the cyclocopter has greater actuation potential than a typically under-actuated system such as a quad-rotor. In other words, the cyclocopter can potentially command instantaneous accelerations in more directions than a quad-rotor. Another potential advantage of a cyclorotor, especially for indoor reconnaissance missions, is its lower acoustic signature when compared to conventional quad-rotors owing to the lower rotational speed. The only drawback of a cyclorotor is the rotor structural weight, which needs to be significantly reduced in the next generation of cyclocopter designs.

It is important to note that the key focus of the previous cyclorotor research was to understand the time-averaged rotor performance (lift, thrust, and power) in both hover and forward flight at moderately low Reynolds numbers (Re ~ 40,000) (Refs. 3 – 10). However, there is a significant dearth in the understanding of the unsteady blade aerodynamics, which is even more important at the ultra-low Reynolds numbers at which the next generation of meso-scale cyclocopters would operate. For a meso-scale cyclocopter shown in Fig. 1 (radius = 1 inch, weight = 29 grams), the operating Reynolds number is around 18,000. At these ultra-low Reynolds numbers, the steady airfoil performance (lift/drag) would be significantly lower compared to moderately low Reynolds numbers (Re ~ 40,000). Additionally, the flow will be extremely susceptible to separation and therefore, even the smallest perturbation could stall conventional rotor blades. In these types of conditions, we expect the unique unsteady aerodynamics of a cyclorotor to greatly enhance performance, similar to that of a flapping wing. This means,

understanding and utilizing the potential of blade unsteady aerodynamics becomes important at these extremely low Reynolds numbers. Therefore, if the focus of the previous research was on time-averaged performance, the goal of the present study is to understand unsteady blade aerodynamic loads in hover at much lower Reynolds numbers ($Re < 20,000$). Knowing the forces and flowfield at each instant of the blade trajectory can reveal key information about how the blade lift, drag and pitching moment are affected by blade pitching kinematics and unsteady flow curvature effects, which forms the motivation for the present work.

Obtaining the instantaneous unsteady forces is extremely challenging if the experiments are conducted in air because at high rotational speeds, the aerodynamic forces are corrupted by the large inertial forces. Therefore, the present study conducted at Texas A&M University utilizes a unique experimental setup to measure the instantaneous blade fluid dynamic forces and flowfield (PIV) on a hovering cyclorotor blade in water at matched Reynolds numbers. The experimental study is complemented by a 2D CFD analysis, which is systematically validated with both force and flowfield measurements. The goal of the proposed research is to measure, for the first time ever, the instantaneous blade forces on a cyclorotor blade at ultra-low Reynolds numbers ($Re \sim 18,000$) and high reduced frequencies ($k \sim 0.3$), and to utilize these results along with PIV flowfield measurements and CFD simulations to unravel the key fluid dynamic mechanisms on a cyclorotor blade.

The second chapter of this thesis will consist of an explanation of the methodology used for both the experimental and computational aspects of the study. The experimental

methodology will describe the setup and procedures used to carry out the tests, and the computational methodology will discuss the numerical methods utilized for the CFD calculations. Chapter 3 will include a discussion of the concept known as dynamic virtual camber, which is a phenomenon unique to a cyclorotor. Chapter 4 will consist of the results from the static pitch and symmetric dynamic pitching experiments, and Chapter 5 will include results from the asymmetric dynamic pitching and Reynolds number effect studies. The last chapter will contain a summary of the thesis work and the major conclusions drawn from the study.

CHAPTER II

METHODOLOGY

This chapter includes a discussion on the various methodologies used to conduct the research for this thesis. The experimental setup for both the force and flowfield measurements will be presented, and the procedure and calculations performed to obtain the final experimental results will be explained. The chapter will then conclude with a description of the computational methodology used to obtain the 2D CFD results for both force and flowfield.

Experimental Methodology

In order to gain understanding of the unsteady flow phenomena on a cyclorotor blade, the instantaneous blade forces are measured in water at matched Reynolds numbers. The reason for conducting these experiments in water is due to the ability to match the Reynolds numbers at significantly lower rotor speeds and higher fluid dynamic to inertial force ratio when compared to experiments in air. The forces are directly measured at the blade root using a miniature 6-component force balance.

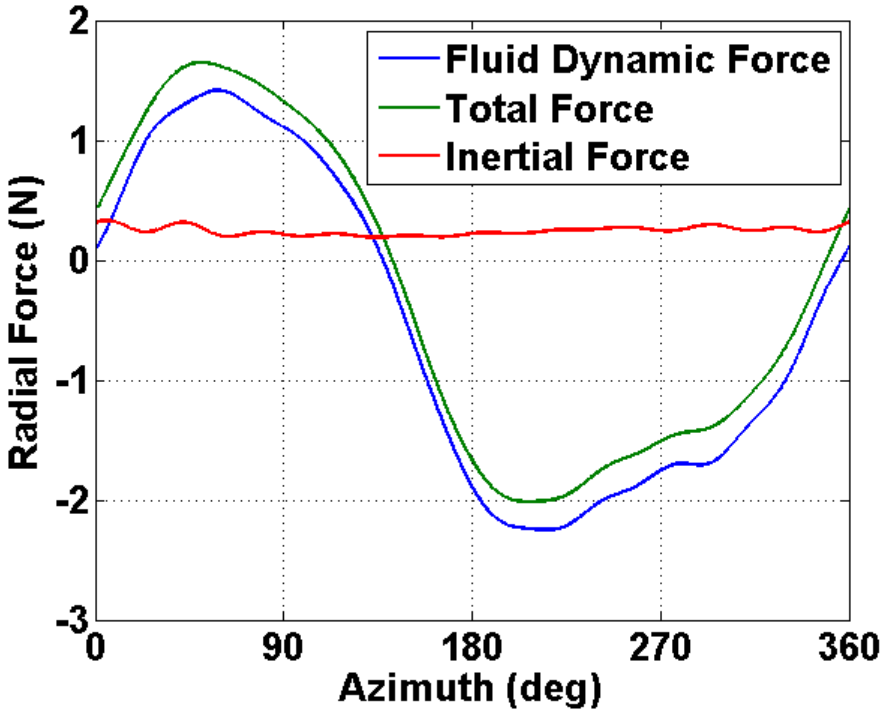

Fig. 6: Blade radial force versus azimuthal location.

To obtain just the fluid dynamic forces acting on the cyclorotor blade, the following procedure is followed: first, the total forces are acquired by performing the experiment in water; next, the inertial forces are obtained by repeating the same experiment in air; finally, to calculate the pure fluid dynamic forces, the inertial forces are subtracted from the total forces. Figure 6 shows the three forces in the radial direction as a function of blade azimuthal position. It can be seen that the inertial forces are only a small fraction of the total forces in water.

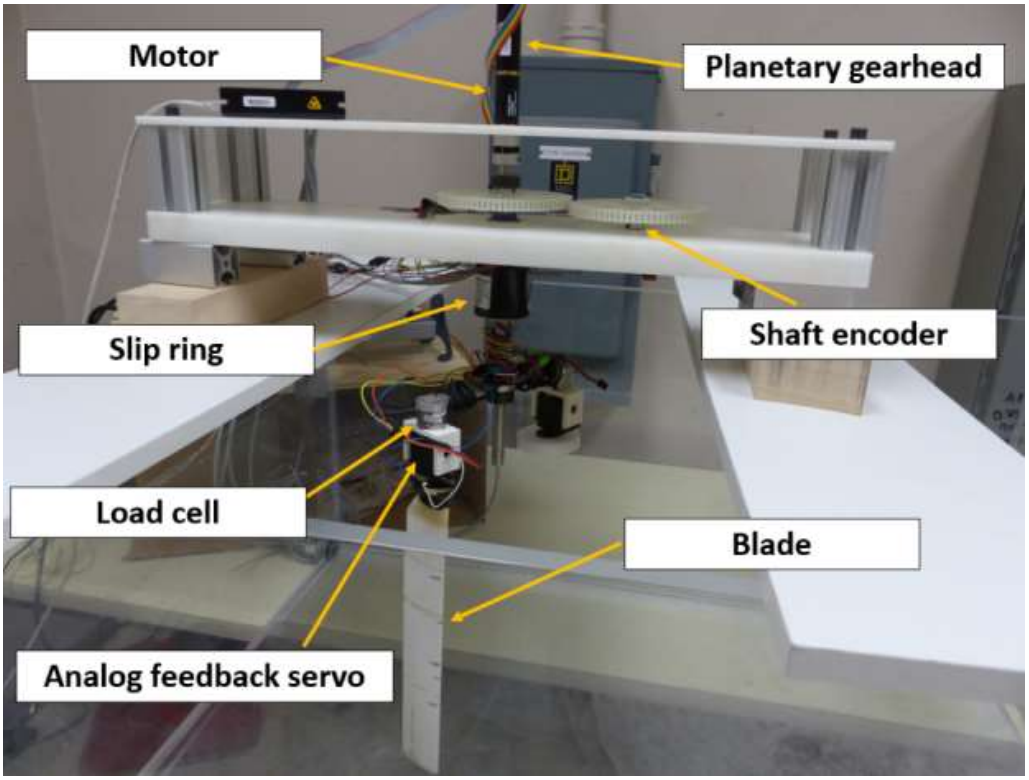

Fig. 7: Single-bladed cyclorotor test rig in water tank.

Experimental Setup

The experimental setup is shown in Fig. 7. For this experiment, the forces and moments are directly measured at the blade root using a miniature 6-component force balance (ATI Mini 27 Titanium). Instead of using the conventional four-bar based blade pitching mechanism, individual blade control (IBC) is implemented using an analog feedback servo. This allows to electronically couple the blade pitch angle with its azimuthal location (obtained using an encoder) by commanding the servo to provide the required blade pitch kinematics based on the feedback from the blade azimuthal position.

The electronic blade pitch control greatly simplifies the blade pitch mechanism. The cyclorotor is 1-bladed with a radius of 3.43 inches, and is rotated by a Maxon EC 22 brushless motor that is equipped with Hall-effect sensors for precise rpm control. The motor is mounted in series with a Maxon Planetary Gearhead with a reduction ratio of 370:1. A 12-channel slip ring is used to transmit the signals from the balance and servo in the rotating frame to the data acquisition equipment in the stationary frame. The tests are performed in a 3.2 ft X 1.6 ft X 2.4 ft rectangular tank, and with a rapid prototyped printed blade. The blade airfoil is a NACA 0015, and has a 12-inch span and 2-inch chord resulting in an effective aspect ratio of 12 (since there is only one free tip). The blade has been coated with shellac to seal any pores in the ABS plastic blade material resulting in water absorption that could corrupt the inertial force measurements.

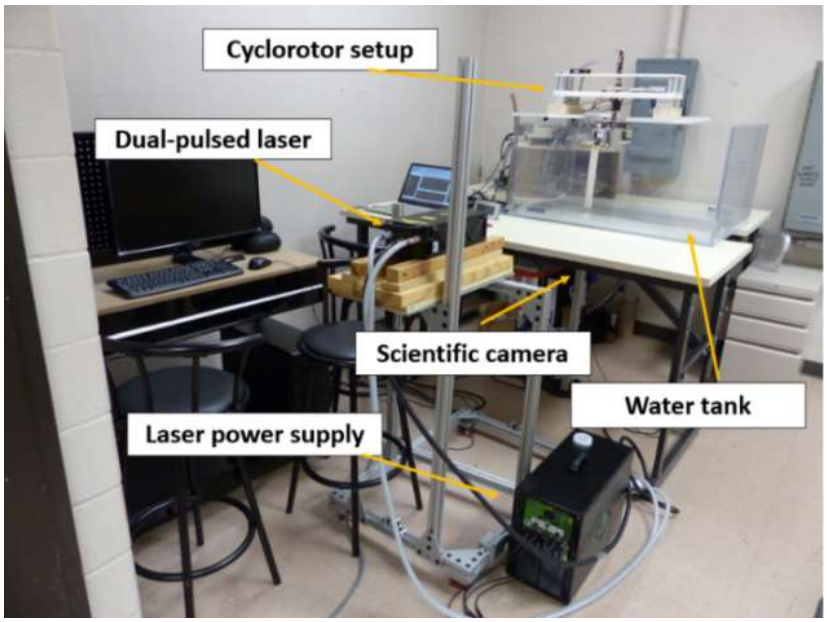

Fig. 8: PIV setup.

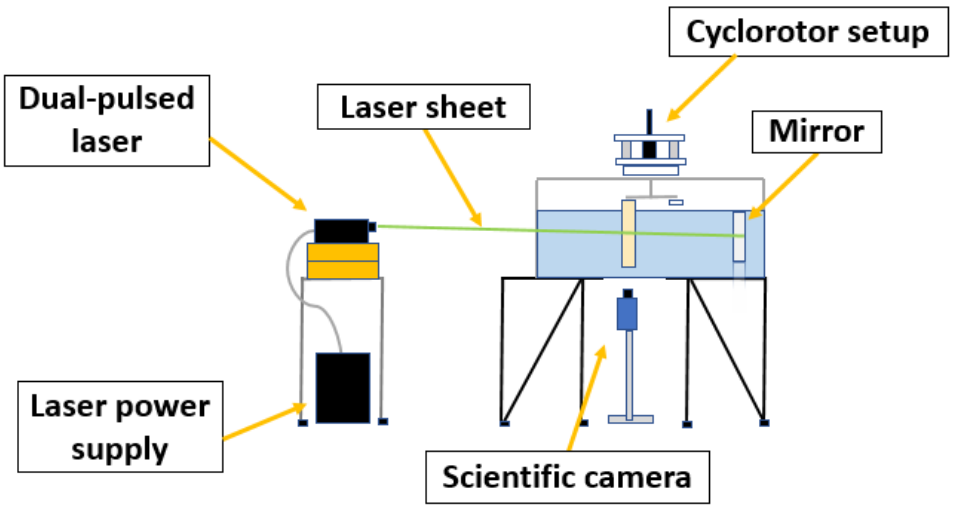

Fig. 9: Schematic of PIV setup.

For conducting detailed flowfield measurements, the same cyclorotor test-rig is implemented with a state-of-the-art PIV system shown in Fig. 8. This system includes an EverGreen dual pulsed laser and power supply, which have been positioned next to the tank. An LaVision Imager sCMOS scientific camera with 5.5 megapixel resolution has been mounted underneath the tank, and pointed normal to the blade tip. The laser has been mounted such that the laser sheet hits midspan on the blade, which allows for visualization of mostly 2-dimensional flow (schematic of the PIV setup shown in Fig. 9). The images are captured and processed using the LaVision DaVis 8 data acquisition and visualization software.

Blade Force and Moment Measurements

Blade forces and moments were measured for both static and dynamic pitch cases. For the static cases, as shown in Fig. 10, the blade pitch angle with respect to the tangent of its circular trajectory was held constant. The purpose of these tests was to understand the effect of static angle of attack and steady flow curvature effects such as virtual camber (explained in subsequent sections), due to the curvilinear nature of the flow experienced by the cyclorotor blades.

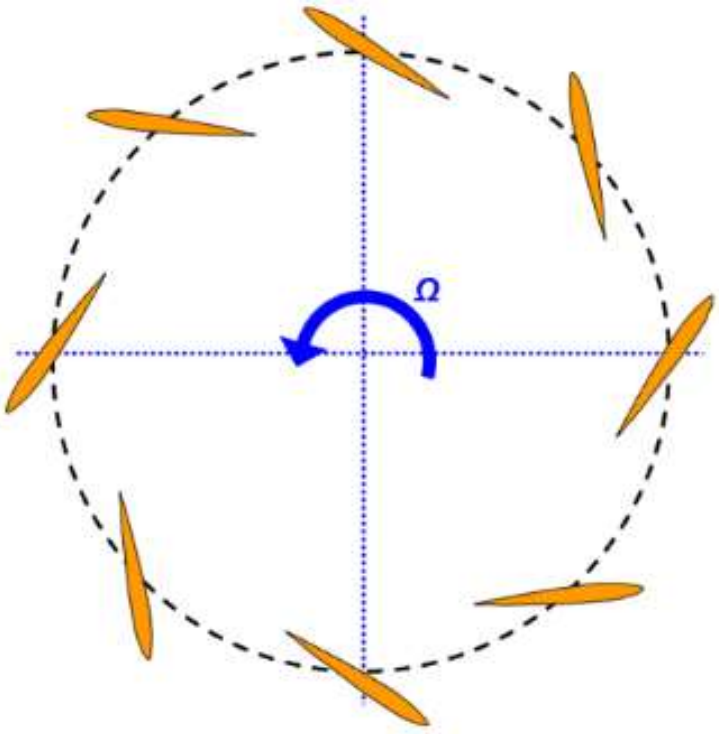

Fig. 10: Blade kinematics for static pitch case.

A static pitch angle sweep from -45° to +45° was performed at 20, 40, and 60 RPM in water, which corresponds to Reynolds numbers of 9,232, 18,465, and 27,697. The next

step was to conduct symmetric and asymmetric dynamic blade pitch experiments on the cyclorotor, meaning that the blade was actively pitched using the blade pitch servo to replicate the cyclic blade pitching kinematics shown in Fig. 2. For symmetric pitching, a pitching amplitude sweep from ±5° to ±45° in steps of 5° was tested at 20, 40, and 60 RPM similar to the static case. For asymmetric pitching, the blade kinematics were similar to that shown in Fig. 2, except that the pitch amplitudes were different between the top and the bottom. One asymmetric pitching amplitude of 60° peak-to-peak was selected, and tests were run at 40 RPM for the following kinematic orientations: 15° Top/ 45° Bottom, 20° Top/ 40° Bottom, 25° Top/ 35° Bottom, 30° Top/ 30° Bottom, 35° Top/ 25° Bottom, 40° Top/ 20° Bottom, and 45° Top/ 15° Bottom.

For each test case, data was recorded for 3 minutes: about 20 seconds of tare data (rotor not rotating), 2 minutes of rotor operating at desired RPM, and the rest of the time duration was used for increasing and decreasing the rotor speed. The data was then processed and analyzed using MATLAB. Each time-history curve presented in this thesis is an average of 40, 80, and 120 waveforms (from the consecutive cycles after the rotor has reached the steady state for each blade RPM tested). Figs. 11 and 12 show the radial and tangential force data for the symmetric pitching case of ±30° at 40 RPM. The red lines represent the cyclic data for 80 revolutions, and the blue line represents the average of the data. Each test case was also performed 3 times, and an average of the three was calculated. This cyclic averaging and test repetition helped minimize any random errors associated with the data.

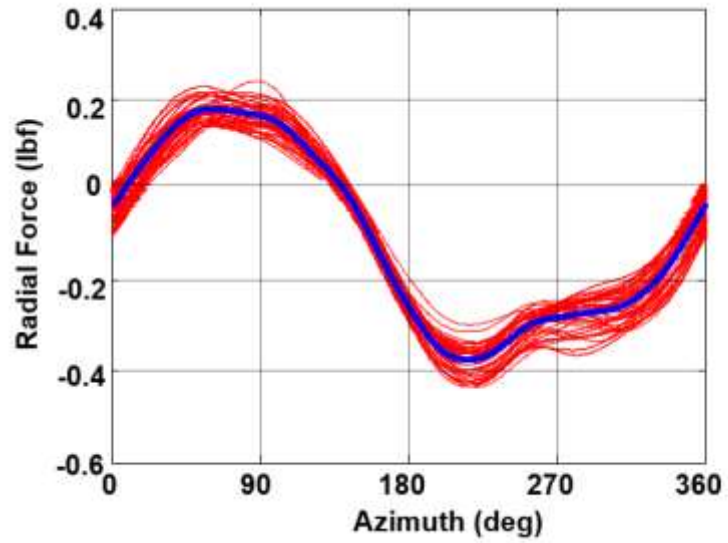

Fig. 11: Radial force for ±30° symmetric pitch at 40 RPM.

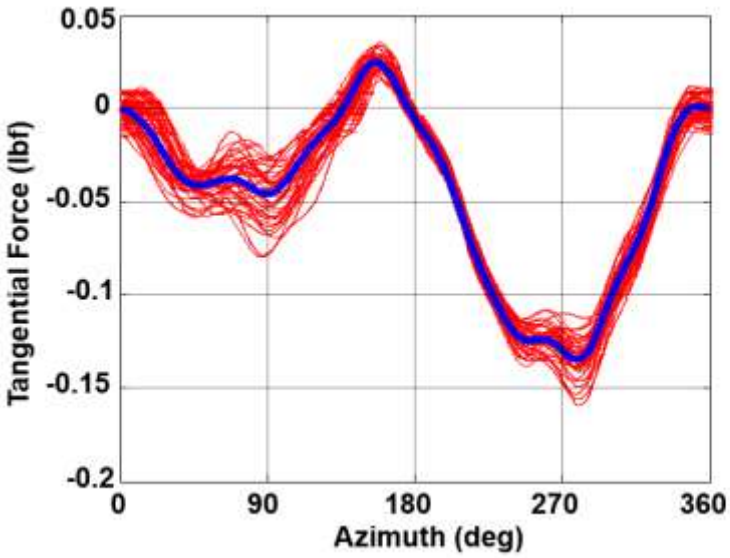

Fig. 12: Tangential force for ±30° symmetric pitch at 40 RPM.

The purpose of doing both static and dynamic pitch experiments was to compare the measured blade forces and flowfield from the two cases and then isolate the unsteady aerodynamic force production mechanisms from the steady ones especially in a curvilinear flow environment, which will be discussed more in the subsequent sections. In this thesis, blade radial force, tangential force and pitching moment are presented. Radial force will be referred to as lift, and is positive when pointed away from the center. Tangential force is drag, and is positive by convention when opposite to the direction of blade motion. The reason for such a terminology is the fact that the inflow velocity is much smaller than the blade speed due to very low disk loading and therefore, the radial force and lift would be approximately in the same direction.

PIV Flowfield Measurements

As mentioned before, the cyclorotor test-rig has been instrumented with a state-of-the-art PIV system, which is used to conduct high resolution flowfield measurements around the blade. The water in the tank is seeded with ~10 μm diameter glass beads. When the laser sheet hits the glass particles, the light is reflected and illuminates the flow. A mirror is also mounted at the back of the tank to reflect the laser light onto the backside of the blade so that the blade shadow is diminished (Fig. 9).

PIV measurements were performed at rotor speeds of 20, 40, and 60 RPM for static pitch cases of 15°, 30° and 45° and dynamic pitch cases with amplitudes of ±15°, ±30° and ±45° to correlate with the force and moment measurement experiments. Phase-locked PIV measurements were conducted around the blade, when the blade reached different

azimuthal locations. Azimuthal resolution for the PIV measurements was 10°, which means flowfield measurements around the blade were made at 36 azimuthal locations in one rotor revolution. The size of the interrogation window around the blade was 80 mm X 66 mm. For each azimuthal location (or phase), 70 phase-locked images of the flowfield were taken at a rate of 2/3 Hz (same as the rotational speed); therefore, one image was taken per rotation. These images were processed using the LaVision DaVis 8 data acquisition and visualization software. An average of the 70 images was computed, and a velocity component representing the rotational velocities (ΩR) of 0.183, 0.365, and 0.547 m/s (corresponding to 20, 40, and 60 RPM) was subtracted, so that the resulting flow vectors are in the rotating frame (as seen by the blade). This is how the flowfield is presented in the paper.

Computational Methodology

Two-dimensional Computational Fluid Dynamic (2D CFD) simulations of the cyclorotor were performed using a Reynolds-averaged Navier–Stokes (RANS) solver called OVERTURNS (Ref. 16). This overset structured mesh solver uses the diagonal form of the implicit approximate factorization method (Ref. 17) with a preconditioned dual time scheme to solve the compressible RANS equations. Computations were performed in the body frame in a time-accurate manner. A third-order MUSCL scheme (Ref. 18) with Roe flux difference splitting (Ref. 19) and Koren's limiter (Ref. 20) was used to compute the inviscid terms, and second-order central differencing was used for the

viscous terms. Due to the low operating Mach numbers of the present cyclorotor, the inclusion of a low Mach preconditioner based on Turkel's method (Ref. 21) helped accelerate convergence and ensure accuracy of the solution. The Spalart–Allmaras (SA) turbulence model (Ref. 22) was employed for RANS closure. This one-equation model is considered advantageous for its ease of implementation, numerical stability, and computational efficiency.

CFD simulations were performed for the static pitch as well as the dynamic pitch cases. The output included radial and tangential force predictions, which were compared with the force and moment measurements, and the flowfield solution, which was compared with the PIV-measured flowfield. The comparison was used to provide insight into the blade loads and flow phenomena around the rotor's azimuth.

CHAPTER III

DYNAMIC VIRTUAL CAMBER

Before the results of the study are presented, a unique phenomenon known as dynamic virtual camber needs to be discussed. This chapter contains an explanation of the virtual camber effect, its dynamic nature, and its dependencies such as azimuthal location, geometry, and pitch rate.

The virtual camber effect occurs due to the chord-wise variation of the incident velocity angle (or angle of attack) on the airfoil. This effect is very predominant in cyclorotors because the flow over a cyclorotor blade is characterized by a pitching airfoil in a curvilinear flow in the presence of inflow that varies along with azimuth.

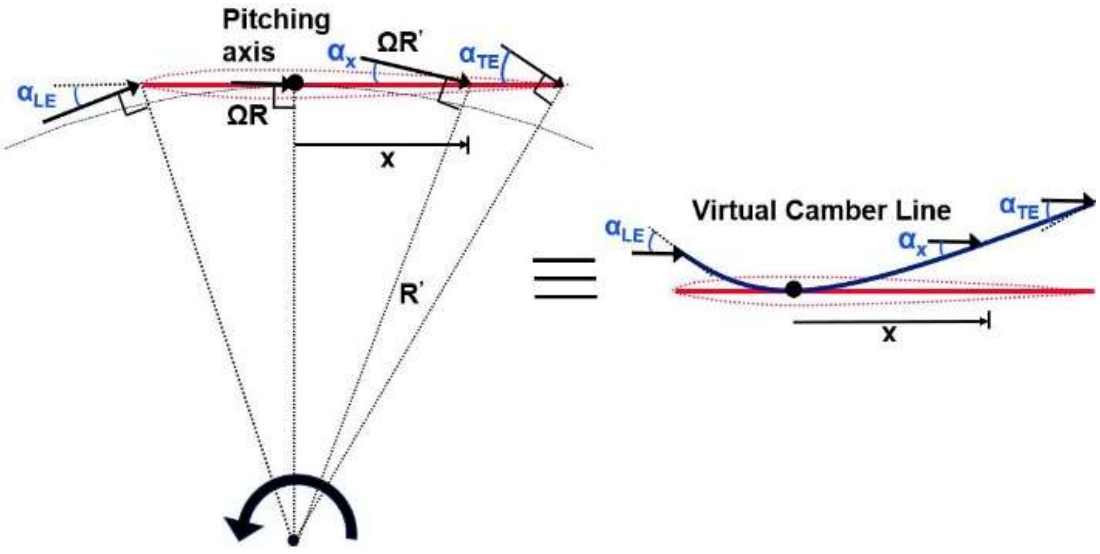

Fig. 13: Negative virtual camber effect due to curvilinear flow.

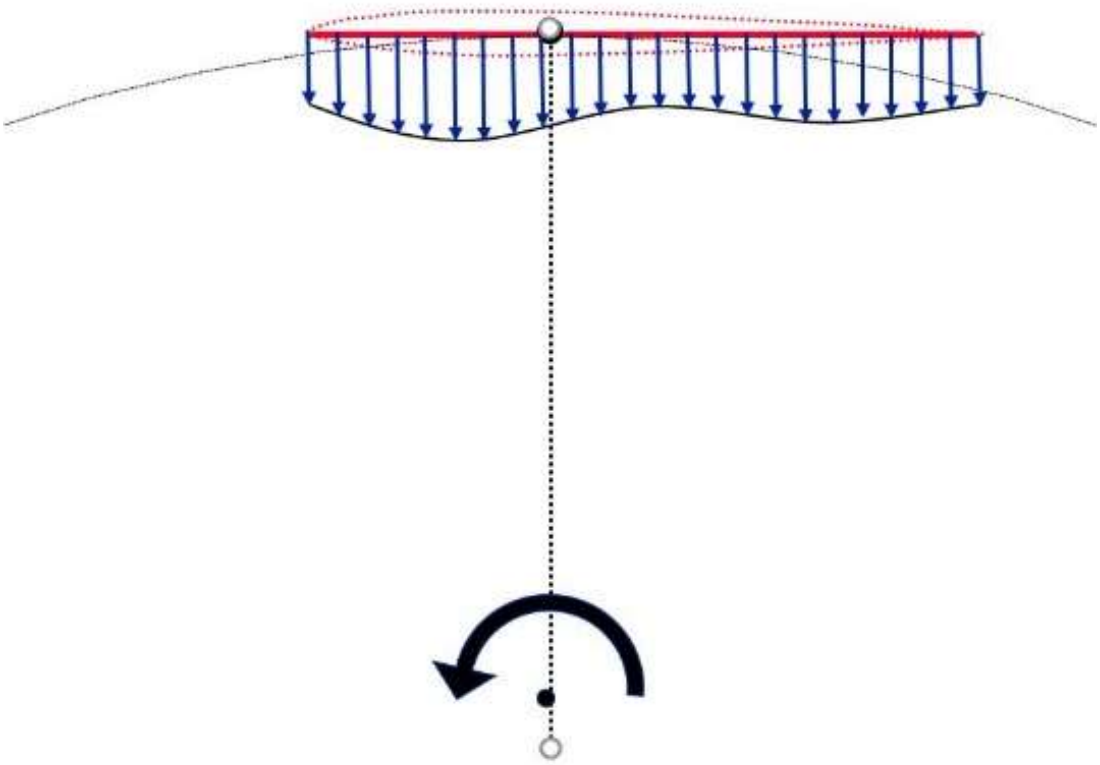

Fig. 14: Chord-wise variation of incidence due to inflow distribution.

An airfoil in a curvilinear flow experiences different flow velocity magnitude and direction along the chord due to geometry and the curvilinear nature of the flow; this manifests as an effective camber and incidence. Figure 13 shows how curvilinear flow geometry creates a negative virtual camber effect for a blade at 0° pitch angle. Therefore, a symmetric blade immersed in a curvilinear flow will behave like a cambered blade in a rectilinear flow as shown in Fig. 13. This phenomenon is more significant for cyclorotors with a large chord-to-radius ratio (c/R).

Flow over a cyclorotor is not purely curvilinear when it is producing thrust because of the induced flow velocity, which also effects virtual camber and incidence (Fig. 14).

Additionally, the blade pitch angle and pitch rate also affect the chord-wise velocity distribution and therefore, virtual camber. Figure 15 shows pitch rate causing chord-wise variation of virtual incidence which is manifested as a positive virtual camber effect. An opposite pitch rate (nose-down pitch) causes a negative virtual camber effect.

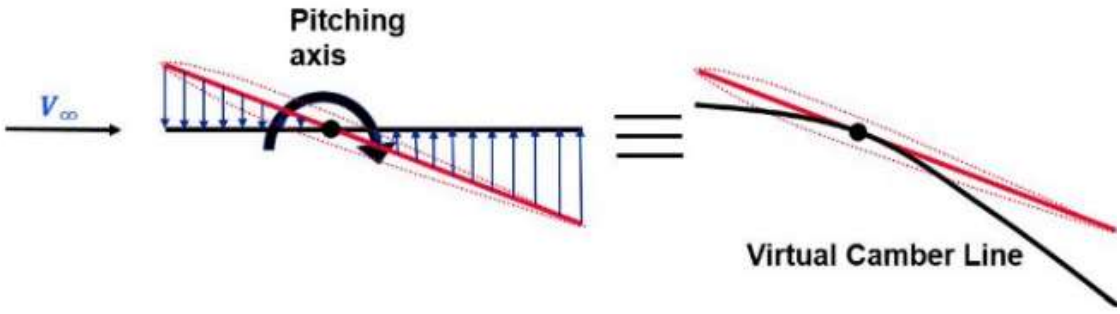

Fig. 15: Positive virtual camber effect due to pitch rate.

Since blade pitch and pitch rate changes with azimuthal location, corresponding virtual camber also changes with azimuth, hence 'dynamic' virtual camber. In essence, the virtual camber experienced by the cyclorotor is a function of chord/radius, blade pitch angle, pitch rate and inflow. Note that on the cyclorotor blade the virtual camber would be apparent in the blade forces as additional lift. Considering all these effects, we have derived a generalized expression (discussed in detail in Ref. 23) to obtain not only the virtually cambered shape of the airfoil but also the additional lift. Figure 16 (i) shows the variation of this additional lift coefficient due to virtual camber versus azimuthal position for a cyclorotor rotating at 40 RPM with 30° pitch amplitude and Figs. 16 (ii) and (iii) show the corresponding prescribed pitch and pitch rate respectively, as blade goes through

various azimuthal locations. Figure 16 (i - iii) shows the effects of virtual camber due to several underlying physical phenomena. It can be observed that virtual camber effect due to only curvilinear geometry (or flow curvature) is static in nature (magenta line) and it always causes negative virtual camber. Pitch and pitch rate create time-dependency of virtual camber effect making it a dynamic virtual camber.

Figure 16 reveals an important result that pitch and especially pitch rate creates a very dominant and characteristic virtual camber effect. Figure 16 (i) shows that blade pitch (black line) decreases negative virtual camber and opposes the effects of curvilinear geometry. The effect of blade pitch is more prominent near 90° and 270° azimuth since pitch angle reaches at its peak at those locations (Fig. 16 (ii)).

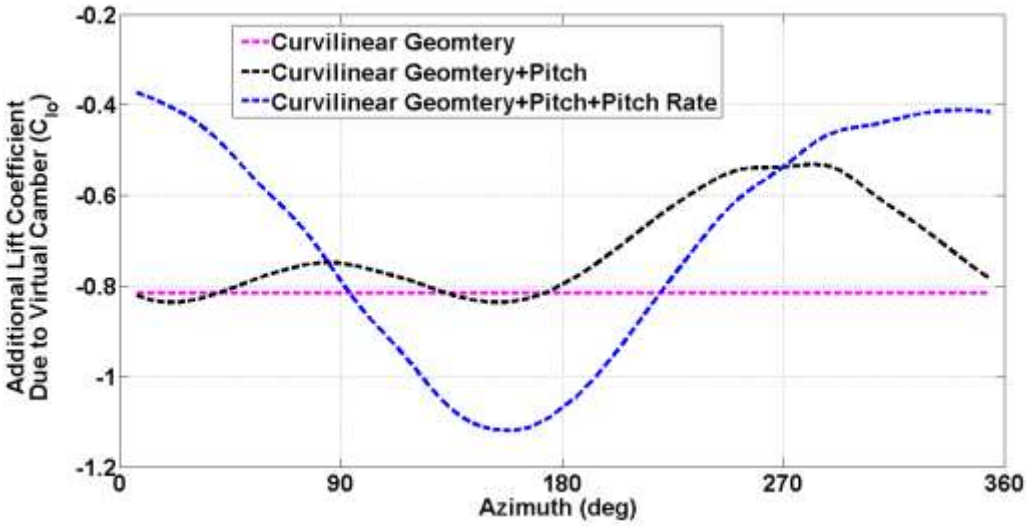

(i) Variation of additional lift coefficient due to virtual camber.

Fig. 16: Effect of curvilinear flow, pitch and pitch rate on virtual camber.

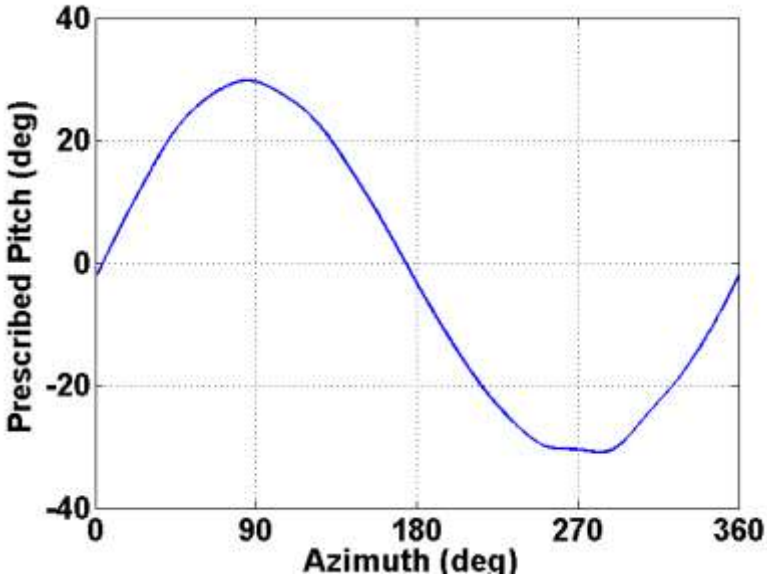

(ii) Prescribed pitch along azimuth.

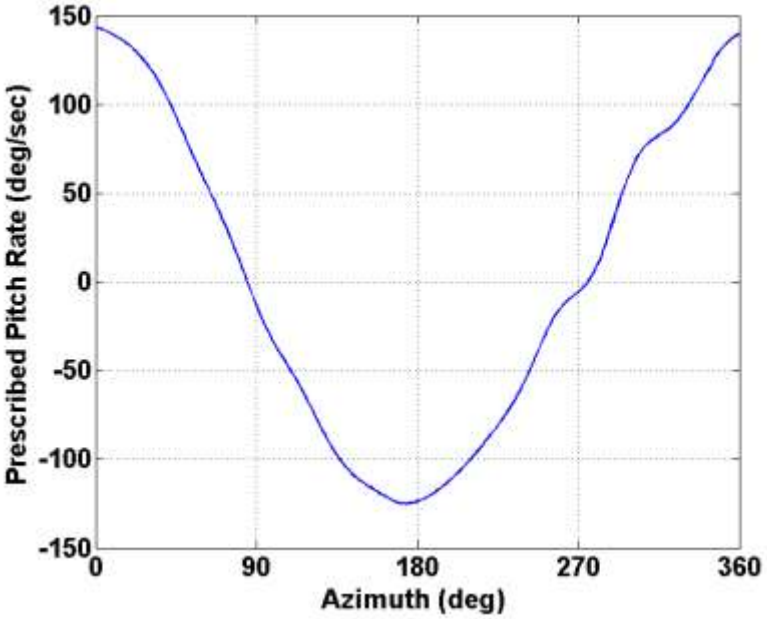

(iii) Prescribed pitch rate along azimuth.

Fig. 16 (continued)

It is also observed that pitch rate (blue line) creates positive virtual camber effect near 0° azimuth, which almost nullifies the effects of curvilinear geometry; while at 180°, it creates negative virtual camber which together with curvilinear effect produces even larger negative lift. For this reason, it will be shown later in the paper that the net lift coefficient is very small at 0° azimuth, while it is much below zero at 180° azimuth, although pitch angle is near 0° at both azimuth locations (Fig. 16 (ii)). Pitch rate effect on virtual camber is dominant at 0° and 180° azimuth because pitch rate reaches its peak near these two locations (Fig. 16 (ii)).

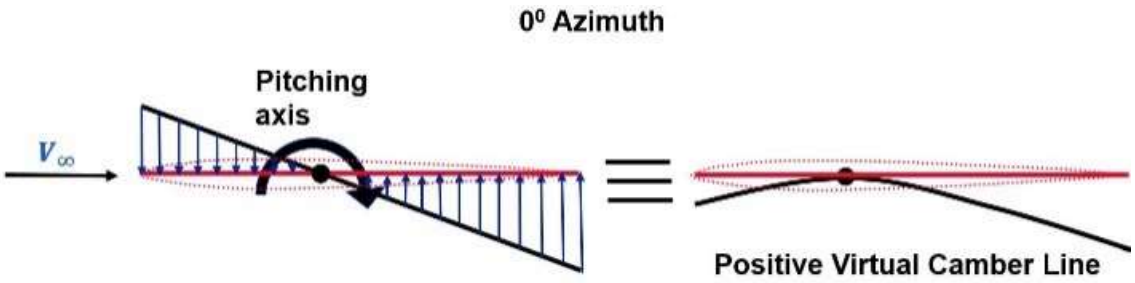

(i) Pitch rate effect at 0° azimuth

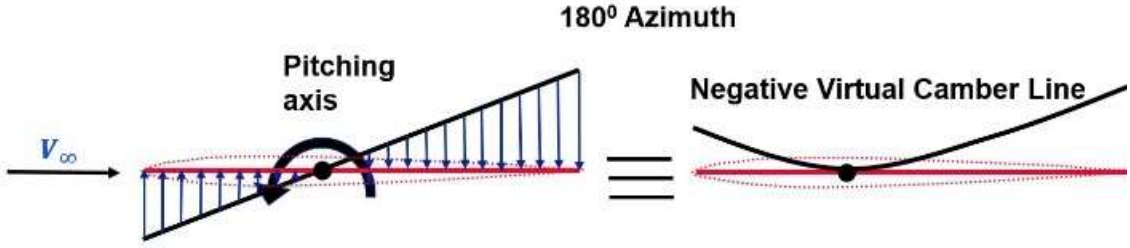

(ii) Pitch rate effect at 180° azimuth

Fig. 17: Effect of pitch rate on dynamic virtual camber at two extreme azimuth locations (0° and 180°).

Figure 17 shows graphically how pitch rate is creating opposite virtual camber effects at different azimuth locations. This phenomenon is also clearly observed in Fig. 18, which shows the actual chord-line of cyclorotor blade and virtual chord-line due to virtual camber effect along different azimuth positions.

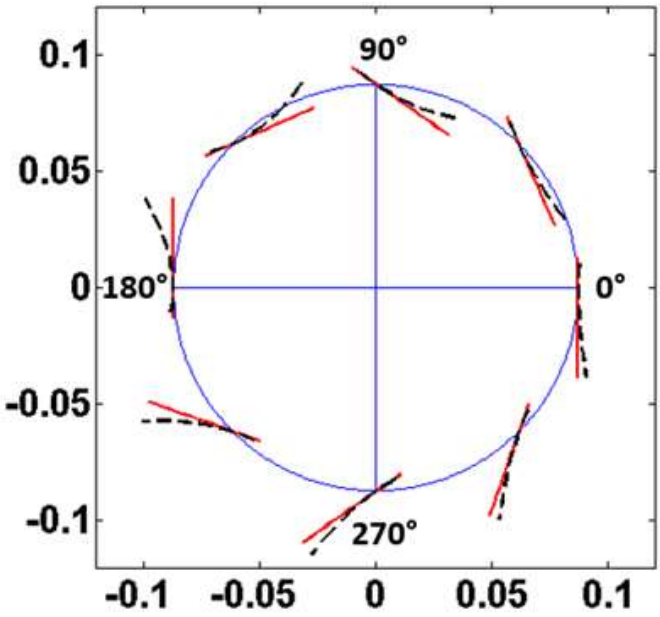

Fig. 18: Virtual chord-line due to virtual camber effect along azimuth.

It can be observed again at 0° azimuth, virtual camber is minimum producing almost negligible negative lift while at 180° azimuth it has huge negative virtual camber producing large negative lift. Based on the convention followed in the paper, lift force directed radially inwards is negative lift. The discussion section of the paper would utilize the virtual shape along with the physical airfoil to understand the physics of force production.

CHAPTER IV

RESULTS: SYMMETRIC PITCHING

This chapter contains the experimental results for the symmetric pitching cases. A comparison of CFD predicted forces and experimental data will be completed for both the static and dynamic pitching cases. The lift, drag, and moment coefficients from the force measurements and the flowfield from the PIV measurements will be compared with CFD. Next, the dynamic pitching experimental results will be discussed, with both force and flowfield measurements presented for several pitching amplitudes. A study comparing the steady and dynamic pitching flowfields will be performed. The chapter will then conclude with an analysis of the physics of force production and the power consumption of a dynamic pitching blade.

Comparison of Experiment and CFD

Force Comparison (Experiment versus CFD)

The first step was to compare the CFD predicted forces with experimental data for both static and dynamic pitch cases.

Static Pitch Case

Figure 19 shows the measured lift coefficient as a function of static pitch angle plotted along with CFD results obtained from the 2D unsteady RANS (Reynolds Averaged

Navier Stokes) simulation for the 40 RPM case. There is good correlation between CFD predicted lift and experimental data especially at positive angles of attack.

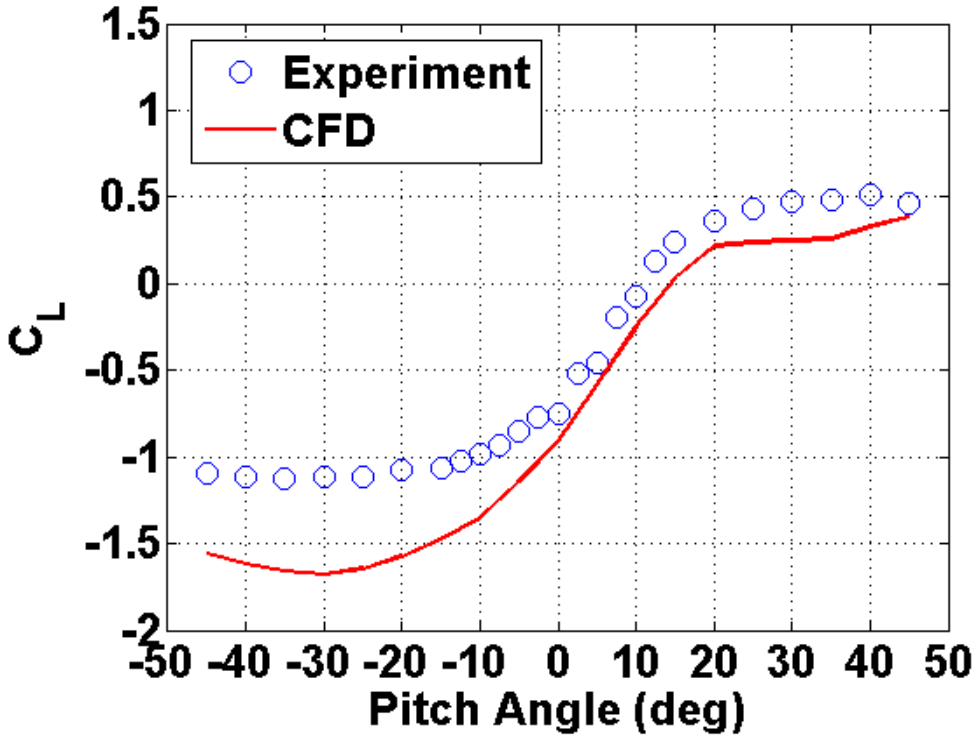

Fig. 19: Lift coefficient versus fixed pitch angle from experiment and CFD.

A key observation from Fig. 19 is that lift curve is highly asymmetric between positive and negative pitch angles even though the airfoil is symmetric. A 0° pitch angle produces a non-zero lift force (CL = -0.75) towards the center of the rotor because of the virtual camber effect (refer Fig. 13) explained in the previous section. Both experiment

and CFD is able to capture this effect even though CFD slightly over-predicts the lift due to virtual camber.

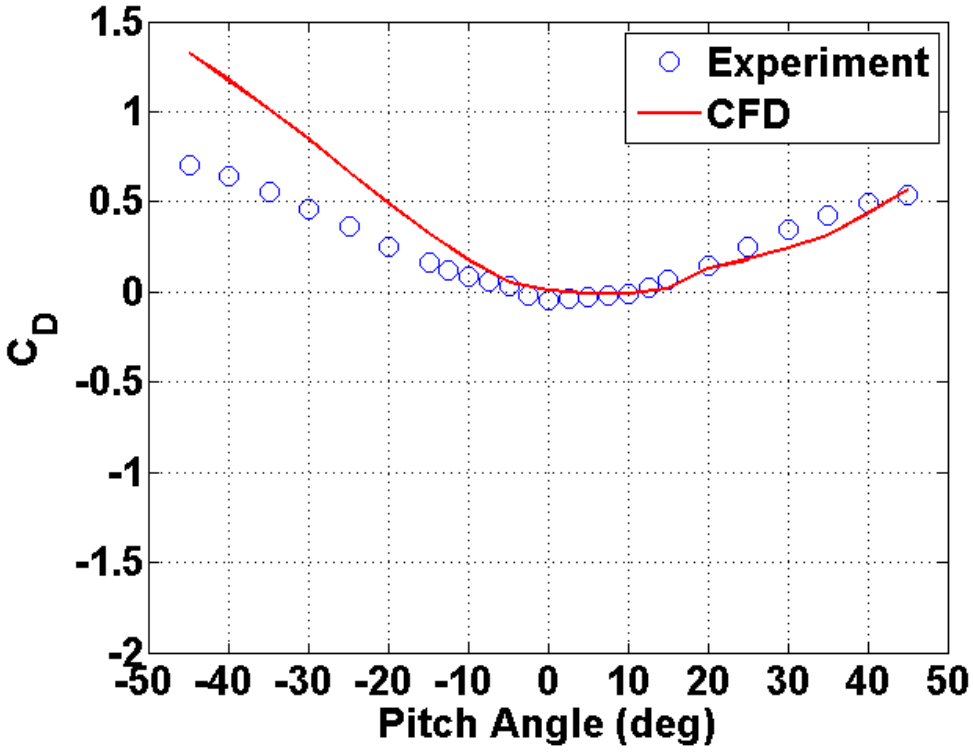

Fig. 20: Drag coefficient versus fixed pitch angle from experiment and CFD.

The drag coefficient as a function of static pitch angle for 40 RPM is shown in Fig. 20. As before, the experimental results are plotted along with the CFD prediction and there is a good correlation between the both, especially for positive pitch angles as in the case of lift. The asymmetry in drag between the positive and negative pitch angles (negative pitch angle causing more drag that positive ones) is due to the virtual camber effect. The

CFD results show the same trend as experimental data. The maximum drag produced is larger for negative pitch angles (C_D = 0.75) than for positive pitch angles (C_D = 0.6). These results clearly show the role of virtual camber effect on the lift and drag production on a static blade experiencing a curvilinear flow. Additionally, these results are also very relevant to a fixed-pitch vertical axis wind turbine blade.

Dynamic Pitch Case

The measured and CFD predicted lift and drag coefficients as a function of azimuthal location for dynamic pitching angles of ±15°, ±30°, and ±45° and a blade RPM of 40 are shown in Figure 21. For all the three cases the CFD results correlate well with the experimental data for the upper half of the azimuth (Ψ = 0° - 180°); however, CFD over-predicts both lift and drag in the lower half (Ψ = 180° - 360°). The reasons for this are not fully understood yet; however, it may be due to 3D effects which are not captured in the 2D CFD simulation. It can be seen from Fig. 21 that as expected, as the pitching amplitude increases, both the lift and drag coefficients also increase. Similar to the static pitch experimental results, there is lift asymmetry between the upper and lower halves of the azimuth for the dynamic case. The reason for this asymmetry even though the pitch kinematics is identical in the upper and lower halves (only the sign is different) can be attributed to the dynamic virtual camber effect. As shown in Fig. 18, in the upper half, the blade experiences a negative camber and hence smaller lift compared to the lower half, where the blade experiences a positive camber. As explained before, on a pitching blade the virtual camber is dynamic in nature and arises predominantly because of two reasons: (1) finite chord/radius ratio and the curvilinear nature of the flow, and also (2) the pitch-

rate. Along with the blade pitch angle the dynamic camber plays a key role in the force production on a cyclorotor blade. The subsequent sections would utilize both the measured instantaneous blade forces and flowfield to understand the role of pitch angle and camber on force production on a cyclorotor blade.

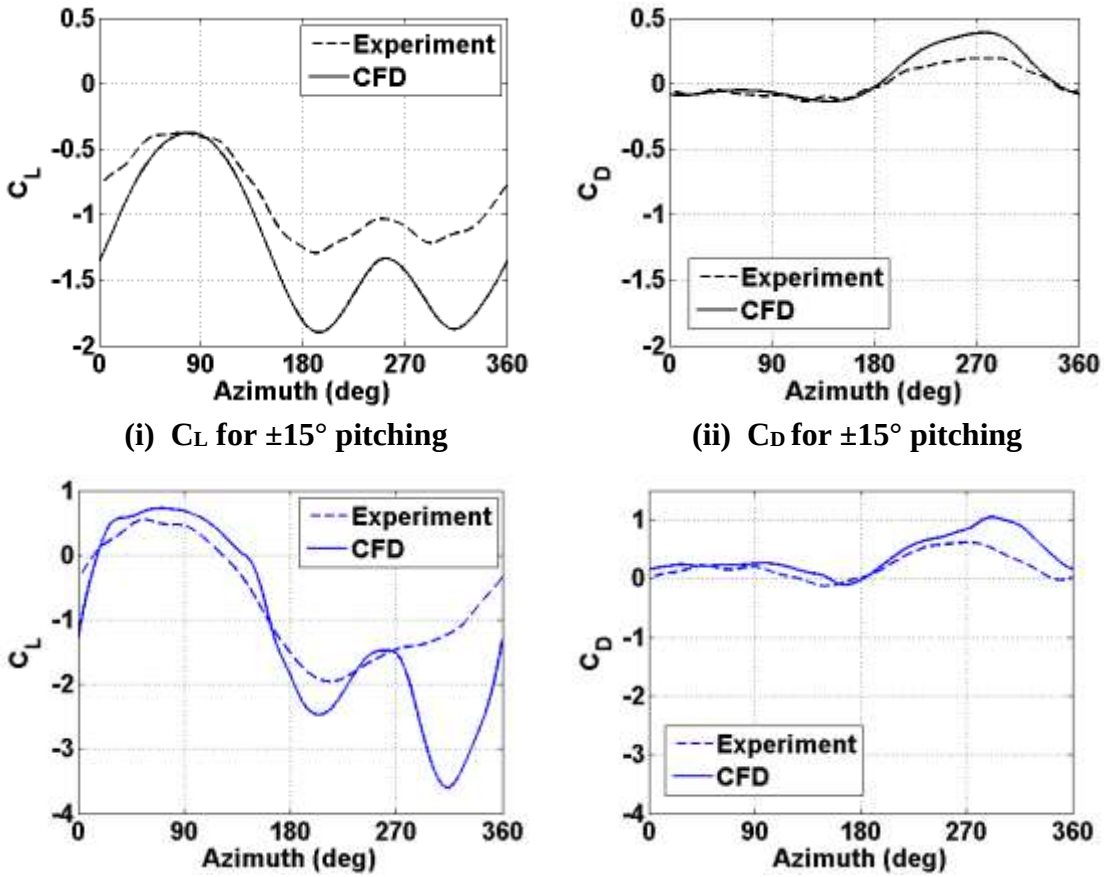

(i) C_L for ±15° pitching **(ii) C_D for ±15° pitching**

(iii) C_L for ±30° pitching **(iv) C_D for ±30° pitching**

Fig. 21: Lift and drag coefficients versus azimuth for ±15°, ±30°, and ±45° dynamic pitching.

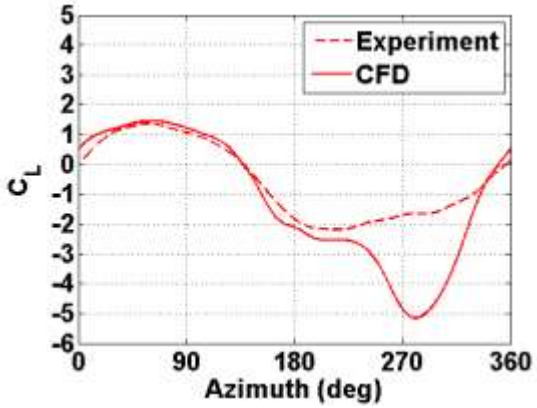

(v) C_L for ±45° pitching

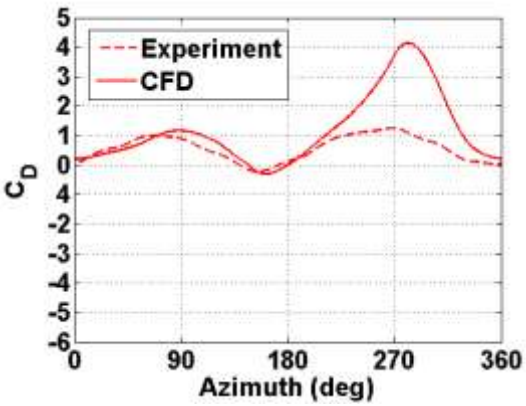

(vi) C_D for ±45° pitching

Fig. 21 (continued)

Flowfield Comparison (PIV versus CFD)

The next step was to compare the CFD predicted flowfield around the blade at different azimuthal locations with the PIV measured flowfield.

Dynamic Pitch Comparison

Figure 22 shows a comparison of flow velocity vectors and vorticity contours obtained using PIV with the flow solution predicted by CFD for the dynamic pitching case with an amplitude of ±45°. The images correspond to azimuthal locations of 50°, 60°, 70°, 80°, 90°, 100°, 260°, and 270°. These azimuthal values were chosen because these are the locations where the blade attains high pitch angles and hence leads to significant growth and shedding of dynamic stall vortices. From Fig. 22, it is significant to note that, overall, there is very good correlation between PIV measured flowfield and CFD even for such high pitch amplitudes (±45°). When the blade is operating in the upper half of its circular trajectory (shown in Figs. 22 (i) – (xii)), there is the formation and shedding of a strong

dynamic stall or leading edge vortex (LEV). The azimuthal location of the blade is shown on the schematic on each PIV figure. As the blade pitch angle increases, the vortex increases in size. At Ψ = 100° (Fig. 22 (xi) and (xii)), the vortex begins to separate from the leading edge and convect over the blade. As the vortex disturbance moves along the chord there is an increase in the nose-down pitching moment, which is due to the aft moving center of pressure.

PIV **CFD**

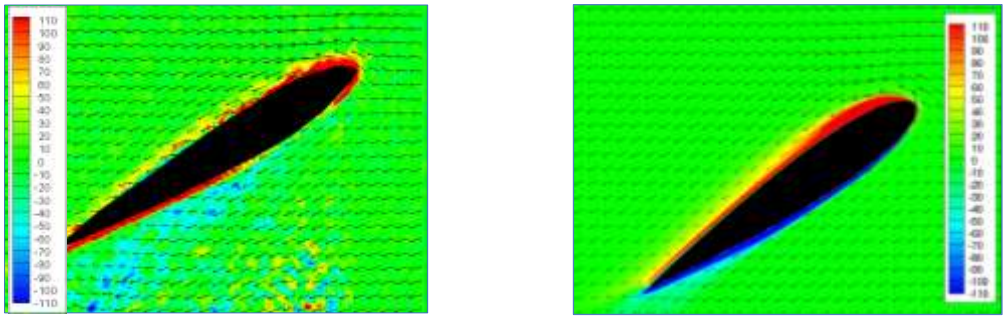

(i) Ψ = 50° for PIV **(ii) Ψ = 50° for CFD**

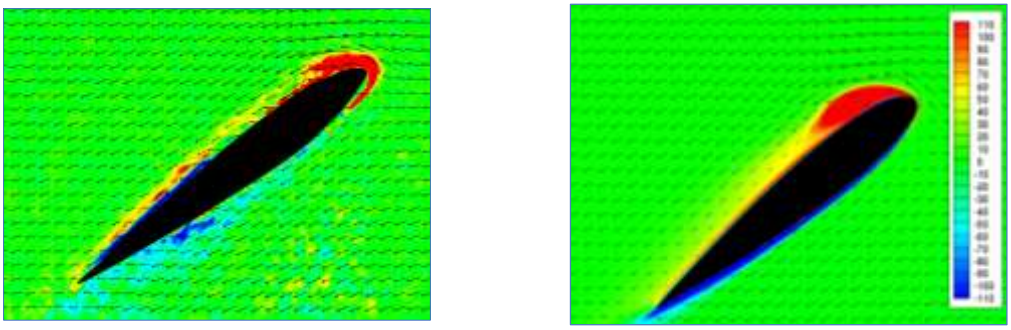

(iii) Ψ = 60° for PIV **(iv) Ψ = 60° for CFD**

Fig. 22: PIV versus CFD flowfield for ±45° pitching.

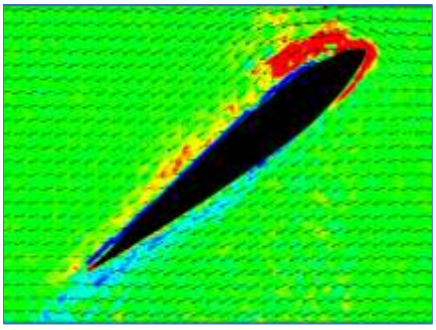

(v) Ψ = 70° for PIV

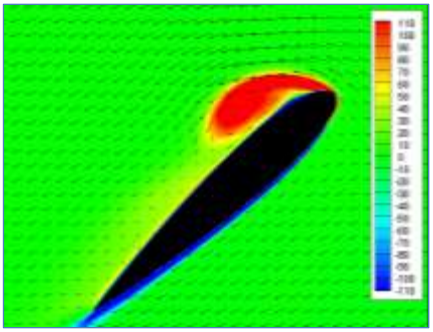

(vi) Ψ = 70° for CFD

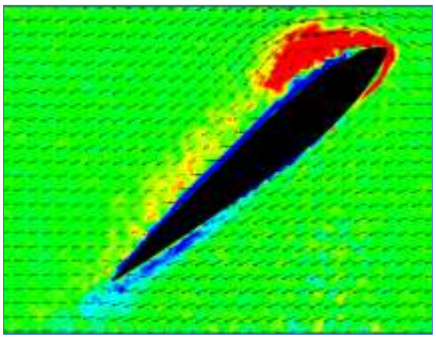

(vii) Ψ = 80° for PIV

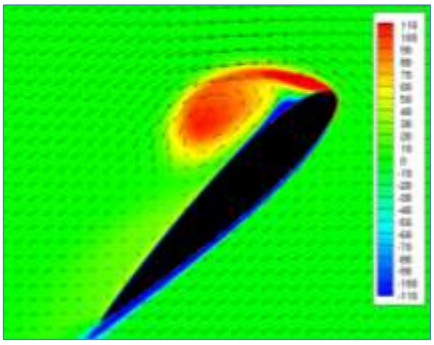

(viii) Ψ = 80° for CFD

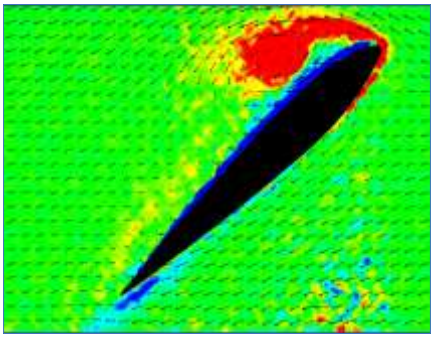

(ix) Ψ = 90° for PIV

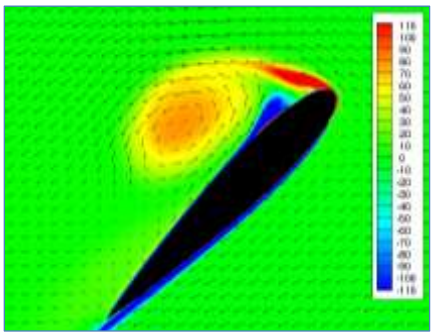

(x) Ψ = 90° for CFD

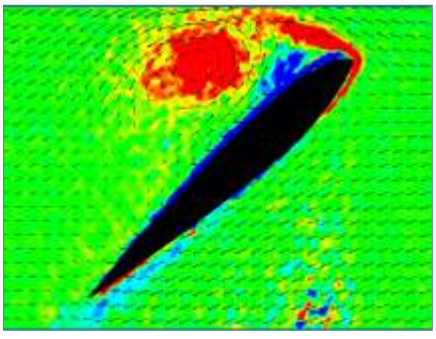

(xi) Ψ = 100° for PIV

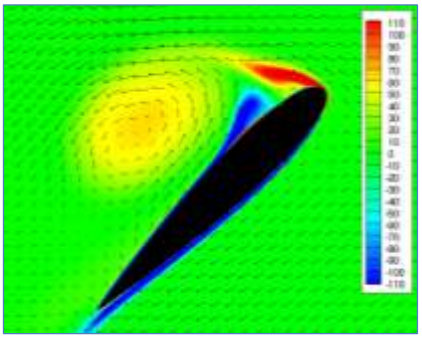

(xii) Ψ = 100° for CFD

Fig. 22 (continued)

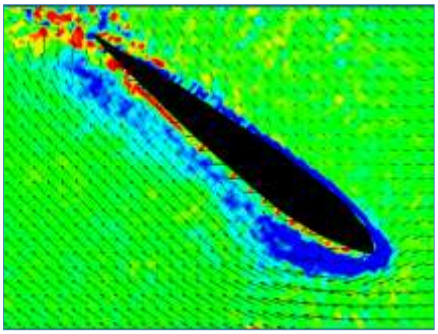

(xiii) Ψ = 260° for PIV

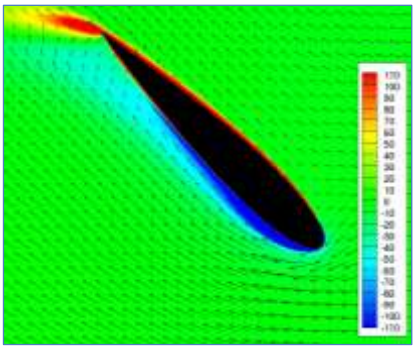

(xiv) Ψ = 260° for CFD

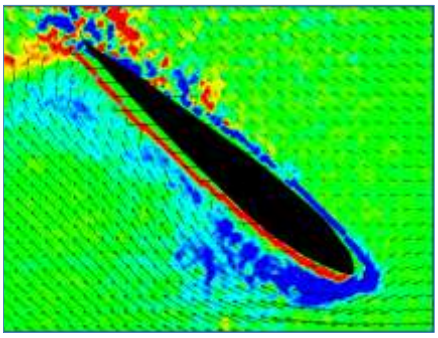

(xv) Ψ = 270° for PIV

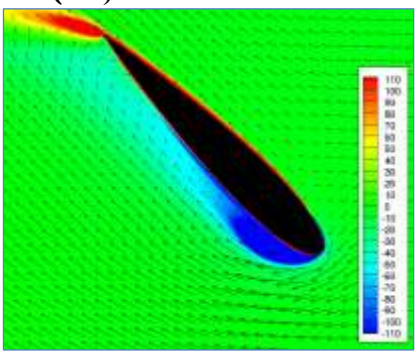

(xvi) Ψ = 270° for CFD

Fig. 22 (continued)

Figures 22 (xiii) – (xvi) show the blade in the lower half of the trajectory where the blade is pitched in the opposite direction (as seen by an observer in the rotating frame). In the lower half, the correlation between PIV and CFD is not as good as the upper half. As expected, the differences between the measured and predicted forces (Fig. 21) in the lower half will also manifest in the flowfield. However, overall flowfield comparison seems good. Even in the lower half, it can be seen from both the CFD and PIV images that a similar vortex disturbance is building up on the leading edge. The colors of the vortex here (fuscha and blue) are different from those of the vortex on the upper half of the cycle (red and orange) due to the change in the sign of the vorticity. The rolling-up of the shear

layer has switched directions which results in vorticity of opposite sense and hence, opposite sign. It is also important to note that, even though the blade is symmetric, the flow phenomena during the nose-up and nose-down pitching is very dissimilar primarily because of the dynamic virtual camber, which is in opposite direction for nose-up and nose-down pitching because of the fact that the flow curvature is always in one direction (refer to Fig. 18).

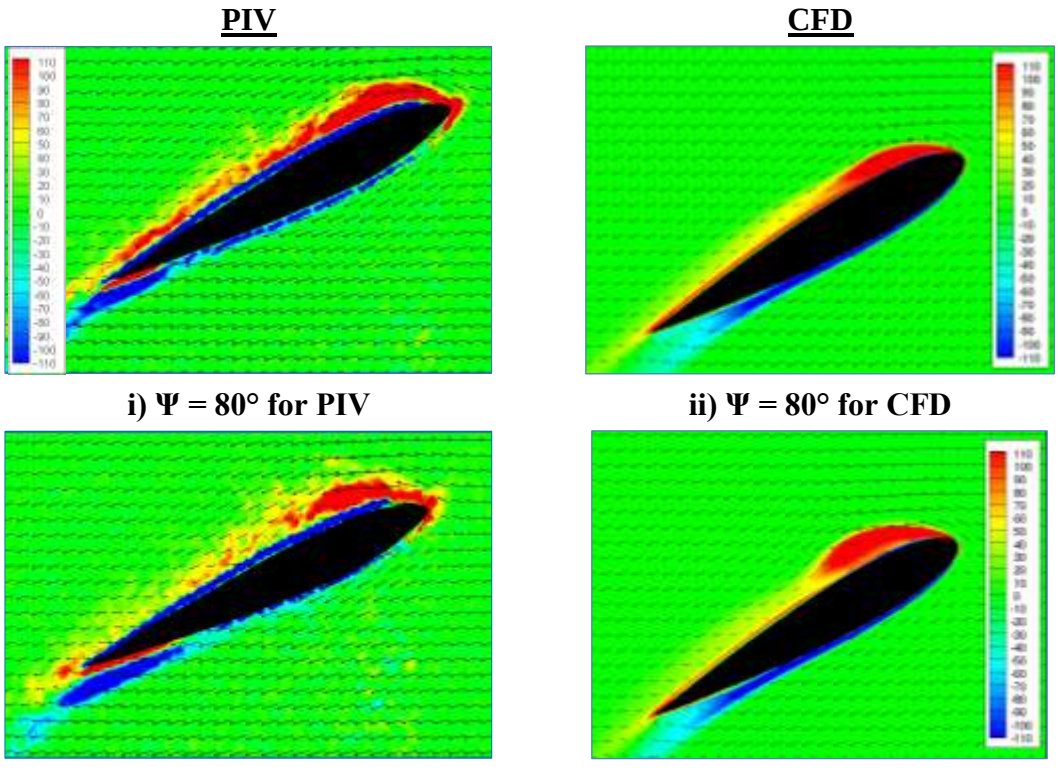

Fig. 23: PIV versus CFD flowfield for ±30° pitching.

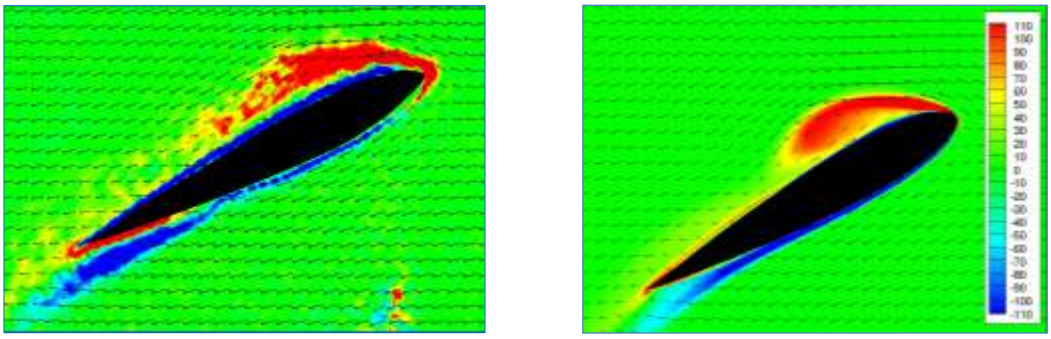

v) Ψ = 100° for PIV **vi) Ψ = 100° for CFD**

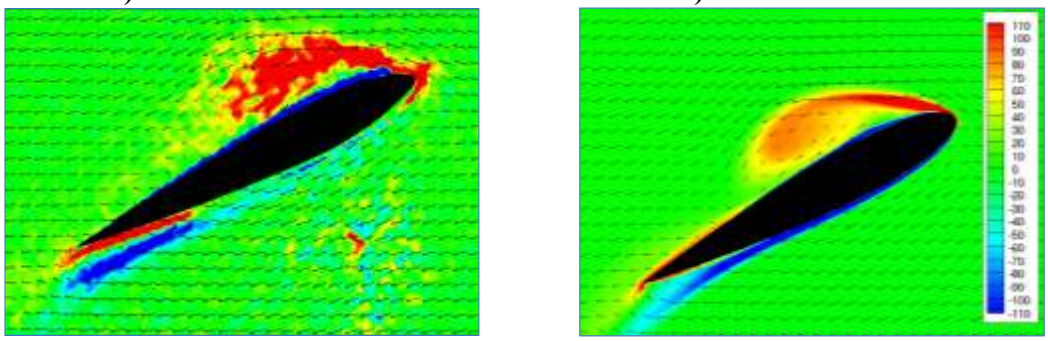

vii) Ψ = 110° for PIV **viii) Ψ = 110° for CFD**

Fig. 23 (continued)

The PIV and CFD flowfield comparison for the dynamic pitching case for an amplitude of ±30° is shown in Fig. 23. The images correspond to azimuthal locations of 80°, 90°, 100°, and 110°. Again in this case there is very good correlation between CFD and PIV measured flowfield, which is notable considering the complexity in the flowfield. As in the ±45° dynamic pitching case, a vortex disturbance is seen building on the leading edge in images from Fig. 23 (i) – (iv). It should be noted that the dynamic stall vortex for the ±30° case does not reach the strength nor develop the same way as the vortex in the ±45° case. For example, at the azimuthal location of 90°, the ±45° case (Fig. 22 (ix) and (x)) shows a vortex that is just starting to separate from the leading edge, whereas the ±30° case for the same azimuthal location (Fig. 23 (iii) and (iv)), shows a vortex that is still

building up at the leading edge. Dynamic stall in a curvilinear flow, especially at such high pitch amplitudes, has never been investigated before at any scales. This finding is not intuitive because one would expect the blade to be fully stalled at a pitch angle of 30° and the flow to just separate from the leading edge. However, due to the unique unsteady flow mechanisms at ultra-low Reynolds numbers in a dynamic pitching environment, the flow remains more or less attached with a strong leading edge vortex even when the blade pitch angle reaches 30° (Fig. 23 (iii) and (iv)) greatly enhancing the lift coefficient as shown in Fig. 21.

Dynamic Pitching Experimental Results

The force and moment results from the dynamic blade pitch experiments are shown in Figs. 24 – 27. The measured blade pitch angle and lift coefficient as a function of the azimuth for a pitching amplitude sweep of ±5° to ±45° are shown in Figs. 24 and 25, respectively. Similar to the static experiments lift asymmetry can be seen between upper (0° - 180°) and lower (180° - 360°) halves (Fig. 25) due to the virtual camber effect. As shown in Fig. 18, the blade pitch is positive in the upper half resulting in reverse or negative virtual camber and hence smaller lift compared to the lower half where the camber is positive (due to negative pitch). The most significant finding from these results is the large values of the dynamic lift coefficients shown in Fig. 25 when compared to the static lift values shown Fig. 19. The maximum static C_L value for positive pitch is around 0.5 (Fig. 19); whereas the maximum dynamic C_L value for positive pitch is around 1.25

(±45° pitching case), which is more than double. The same effect happens for negative pitch where the maximum static C_L is around -1.2 (Fig. 19), whereas the maximum dynamic C_L during negative pitch is around -2 (±45° pitching case). It is significant to note that the lift coefficient monotonically increases all the way up to a pitching amplitude of ±45°, which, as mentioned previously, is not intuitive because one would expect the blade to stall completely at amplitudes much lower than 45°.

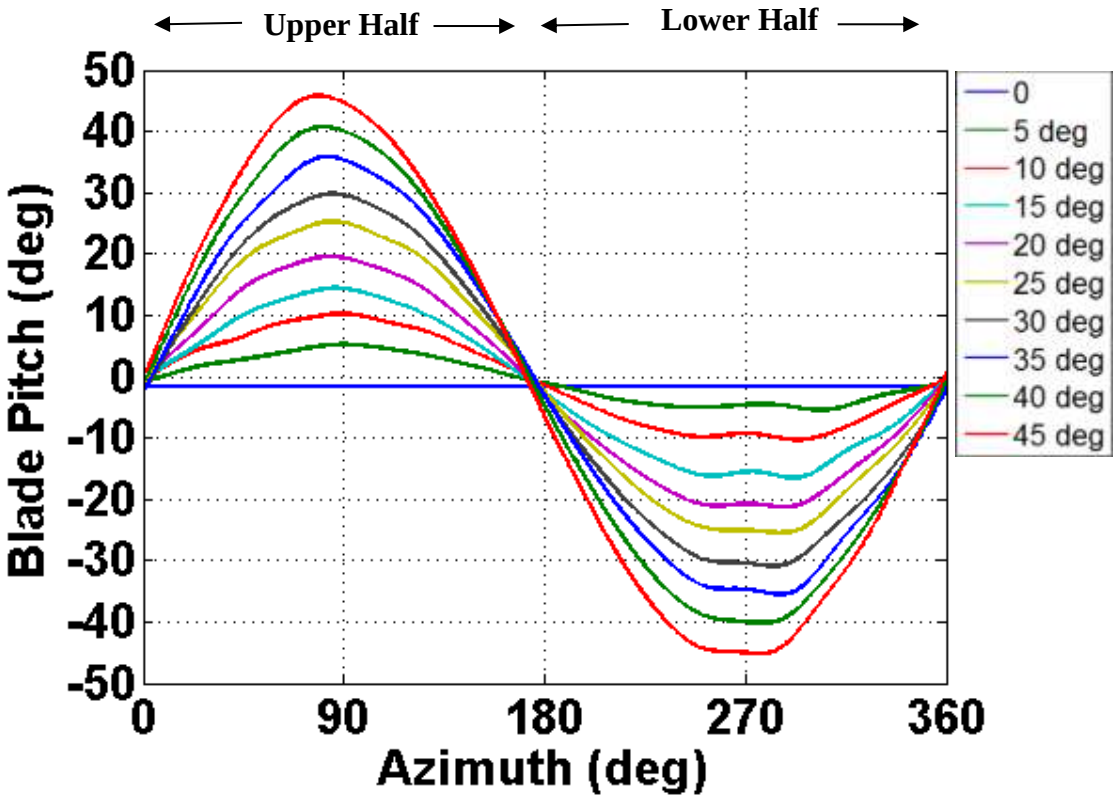

Fig. 24: Measured blade pitch versus azimuth for ±0° to ±45° dynamic pitching.

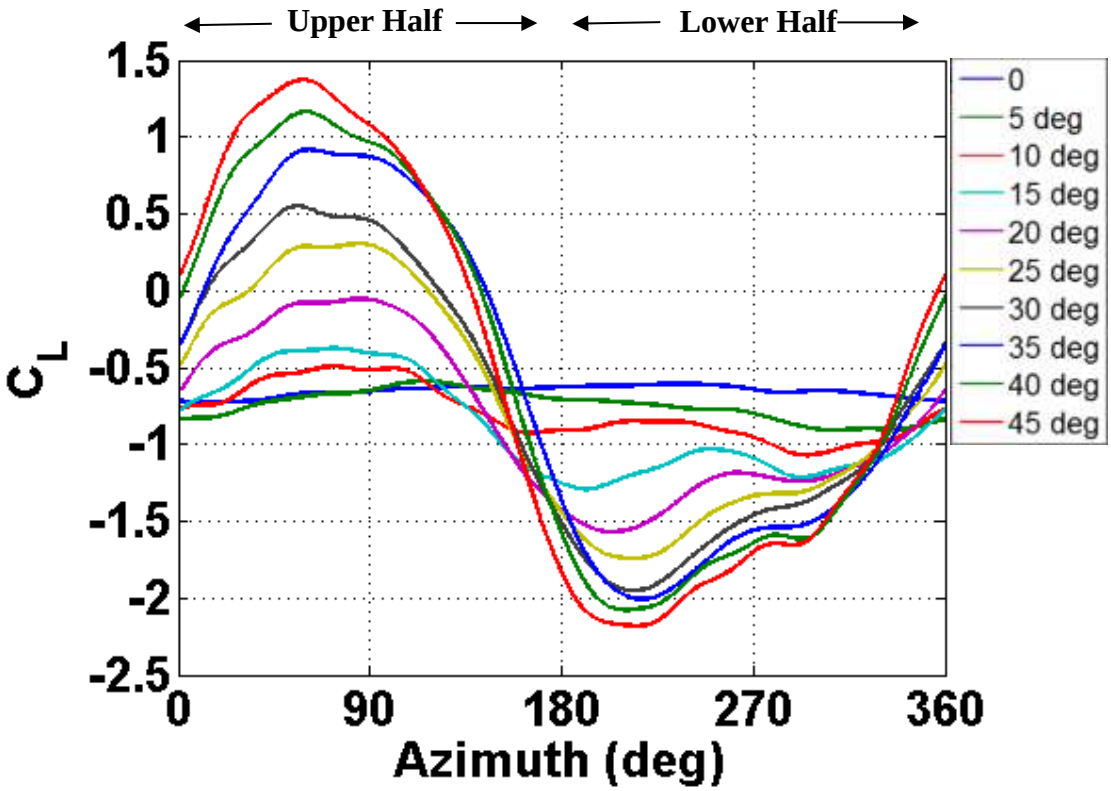

Fig. 25: Measured lift coefficient versus azimuth for ±0° to ±45° dynamic pitching.

The measured drag coefficient as a function of azimuth for the same pitch amplitudes is plotted in Fig. 26. Even the drag coefficient is asymmetric between the upper and lower halves and the magnitude is significantly higher than the static cases shown in Fig. 20. To understand the reason for this huge increase in dynamic lift and drag coefficients on a pitching blade as opposed to a static blade in a curvilinear flow, it is important to look at the flowfield around the blade at different azimuthal locations, which is presented in the subsequent sections.

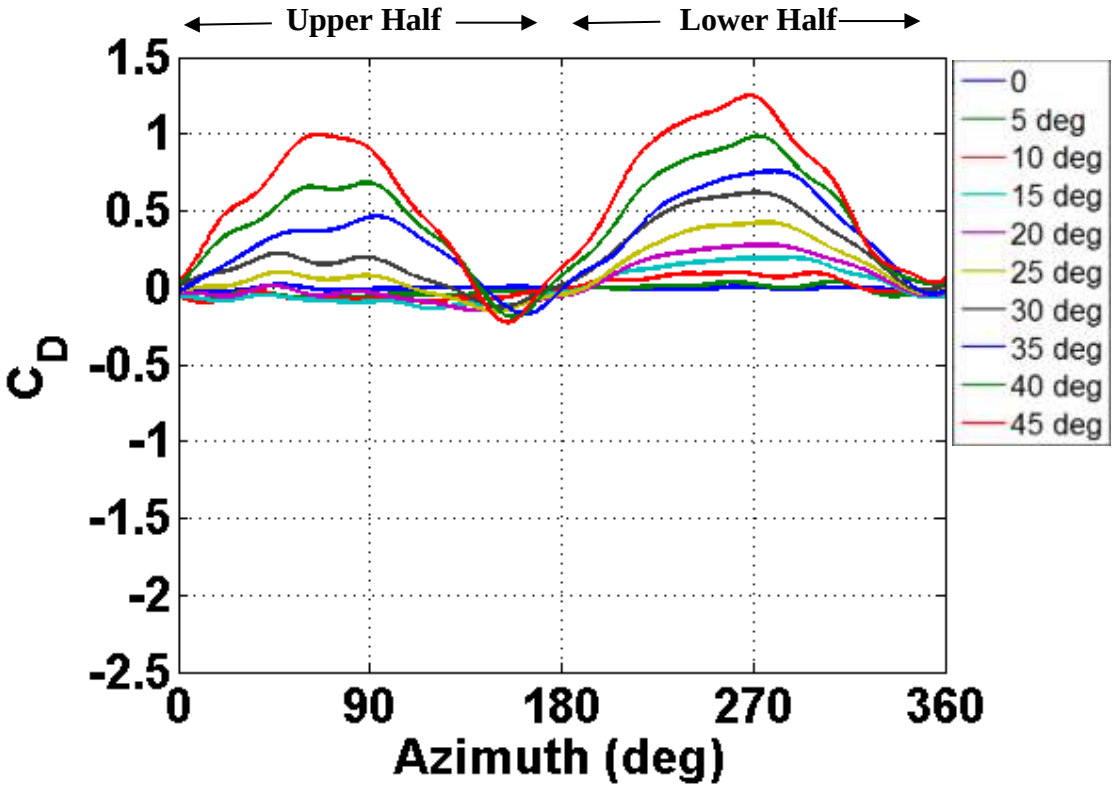

Fig. 26: Measured drag coefficient versus azimuth for ±0° to ±45° dynamic pitching.

Figure 27 shows the variation of the pitching moment coefficient as a function of the azimuth. As mentioned previously, as the blade pitches nose-up and -down, the dynamic-stall vortex is swept downstream and the center of pressure shifts along the chord. This causes a large nose-down pitching moment on the blade. From Fig. 27 it can be seen that the blade experiences moment stall at azimuthal locations of approximately 120° in the upper half and in the lower half at approximately 190°. From the flowfield measurements it can be seen that the local maximum in the upper half is indicative of moment stall due to the formation of a spilled vortex and the local maximum in the lower

half occurs during a state of full separation.

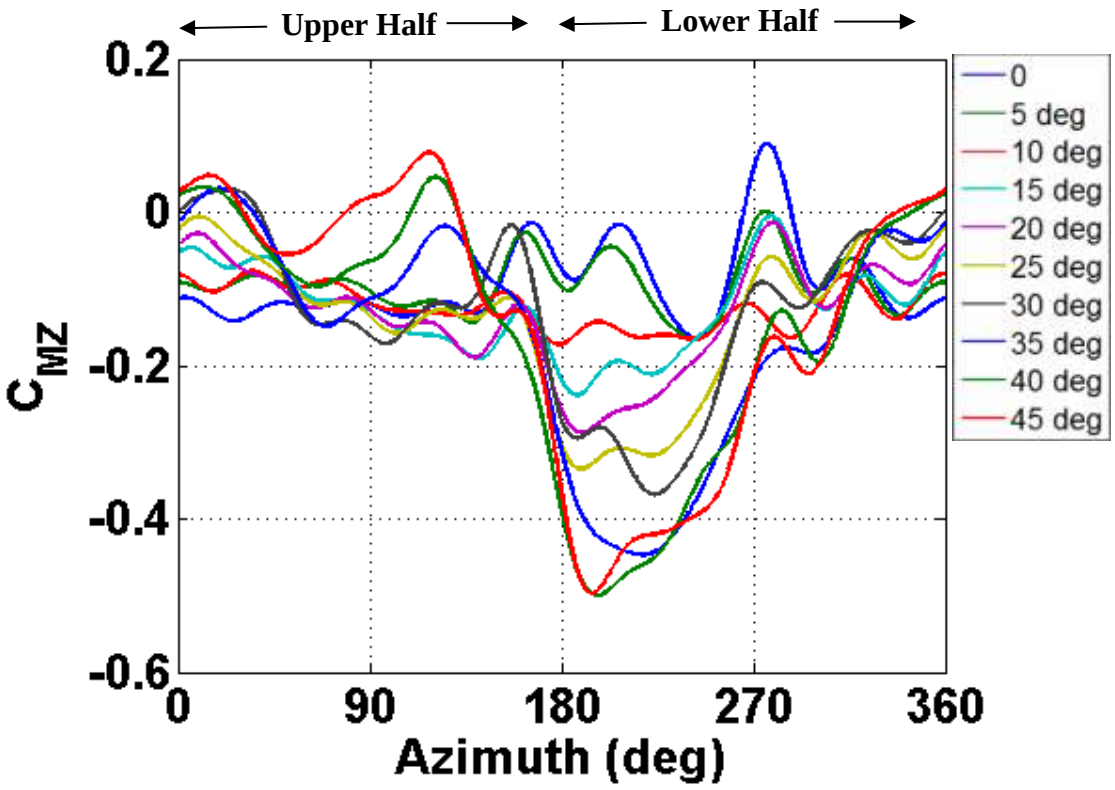

Fig. 27: Measured pitching moment coefficient versus azimuth for ±0° to ±45° dynamic pitching.

To better understand the source of lift and drag forces on a cyclorotor blade operating at ultra-low Reynolds numbers (Re~18,000), it is helpful to identify whether the dominating forces are due to pressure or viscous forces. If there are only pressure forces, the resultant force (denoted by R in Fig. 28) would be normal to the blade chord. In Fig. 28, β represents the angle between the resultant of the lift and drag forces (R) and blade

chord. If the forces are indeed dominated by the pressure force, R would be more or less normal to the chord and β would be close to 90°.

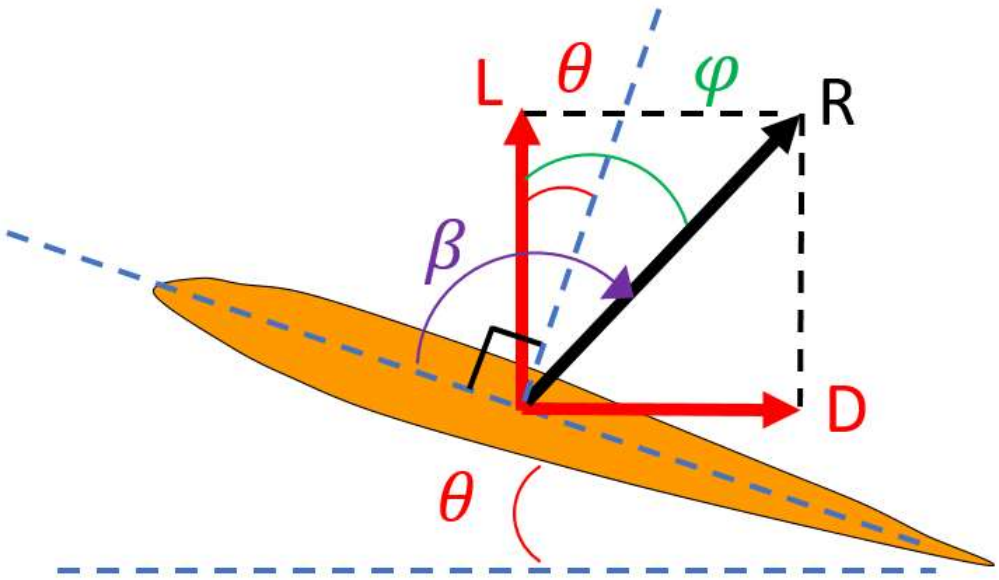

Fig. 28: Schematic showing blade forces.

The lift and drag shown in the diagram can be defined as:

$$L = R\cos\varphi \qquad \text{(Eq 1)}$$

$$D = R\sin\varphi \qquad \text{(Eq 2)}$$

where φ, the phase angle between the lift vector and the resultant vector is the following:

$$\varphi = tan^{-1}(D/L) \qquad \text{(Eq 3)}$$

Finally, the angle β can be computed using Equation 4:

$$\beta = 90 + (\varphi - \theta) \qquad \text{(Eq 4)}$$

If the forces are dominated mainly by the pressure forces, the difference between φ and θ will be small, and the angle β will be close to 90°. Deviations from 90° will indicate the presence of viscous forces acting on the blade.

Figure 29 shows the variation of β as a function of the azimuth for all of the dynamic pitching amplitudes. As seen from the figure, for all of the amplitudes, the angle remains close to 90°, which confirms the domineering role of pressure forces as opposed to the shear viscous forces acting parallel to the blade. This is a significant finding considering the ultra-low Reynolds numbers the blade is operating where viscous forces are relatively large.

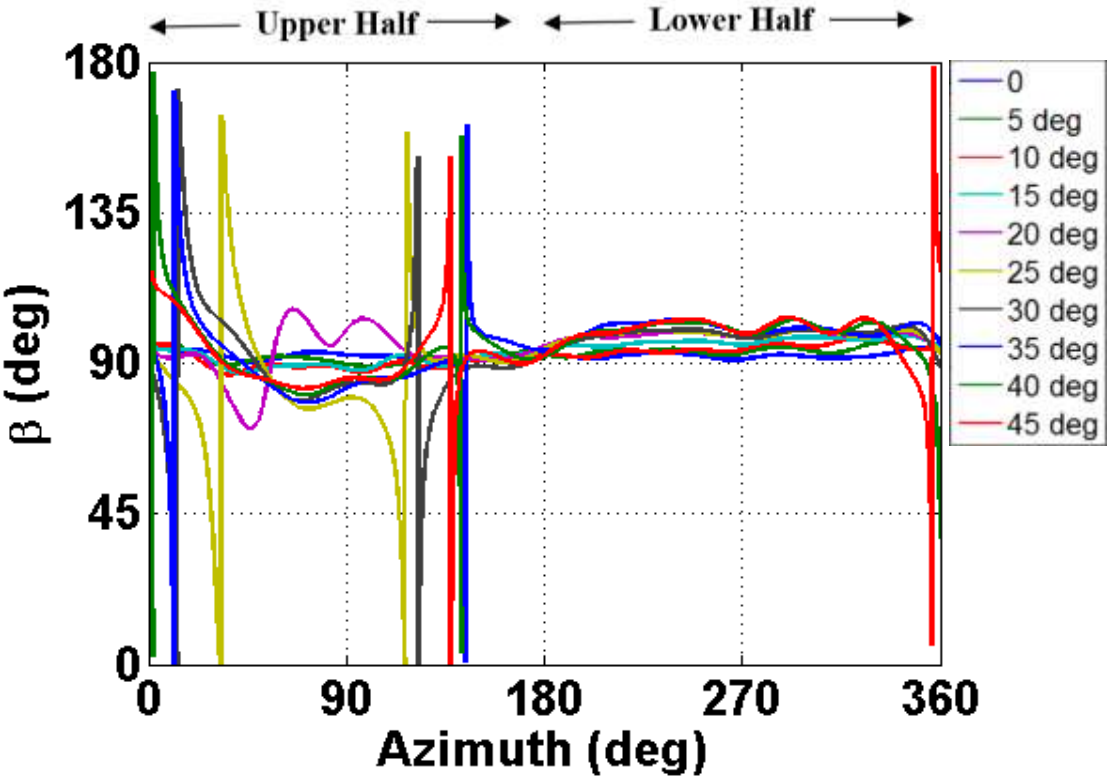

Fig. 29: β versus azimuth for ±0° to ±45° dynamic pitching.

Static Versus Dynamic Pitching

Since there are significant differences in the lift and drag coefficients between the static and dynamic pitching cases, it is important to compare the flowfield for the two cases at the exact same pitch angles to understand the key reason for the lift enhancement for the dynamic case. Figure 30 shows a comparison of PIV measured velocity vectors and vorticity contours for static and dynamic pitching cases at 40 RPM. The static pitch angles include 15°, 30°, and 45°, and the dynamic cases include ±15°, ±30°, and ±45°. For the dynamic pitch case, the flowfield at the azimuthal location of 90° is compared because that is where the blade pitch angle reaches +15°, +30°, and +45°, respectively for the three cases. Therefore, in this comparative study the flowfields are compared at the same pitch angle, but one subjected to steady flow and the other to unsteady flow conditions.

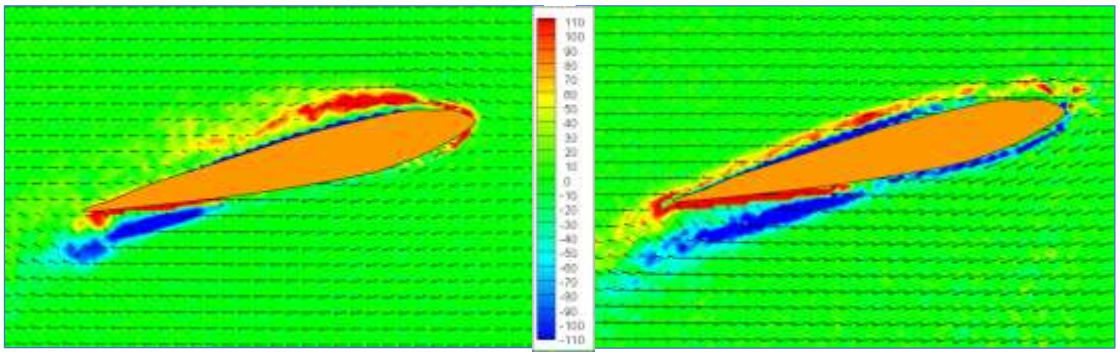

i) Static Pitch = 15°

ii) Dynamic Pitch = ±15° at Ψ = 90°

Fig. 30: Static versus dynamic PIV comparison for 15°, 30°, and 45° pitch angles.

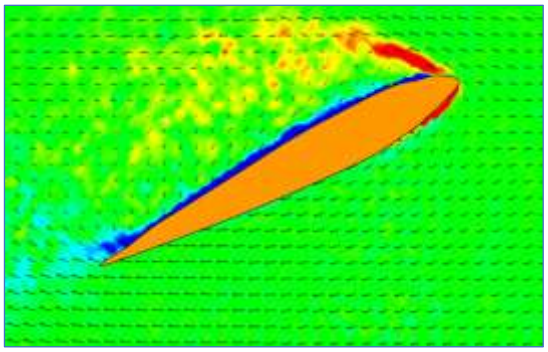

iii) Static Pitch = 30°

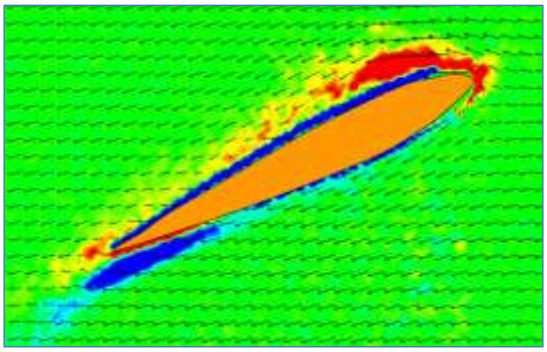

iv) Dynamic Pitch = ±30° at Ψ = 90°

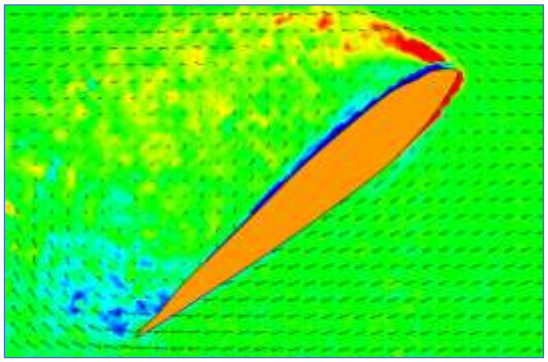

v) Static Pitch = 45°

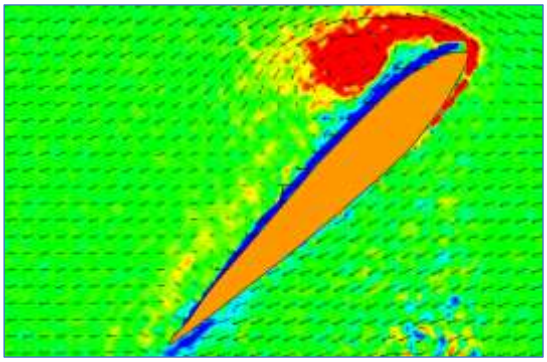

vi) Dynamic Pitch = ±45° at Ψ = 90°

Fig. 30 (continued)

In Figs. 30 (i) and (ii) the blade is at a low angle of attack of 15°; even then, for the static case, as seen from Fig. 30 (i)), the flow has already separated from the leading edge and re-attaches close to the trailing edge forming a large laminar separation bubble (LSB), which is typical on steady airfoil at very low Reynolds numbers. However, for the dynamic case shown in Fig. 30 (ii), when the blade reaches +15° angle of attack the flow is still fully attached showing no signs of stall. The static and dynamic cases for the 30° pitch angle is compared in Figs. 30 (iii) and (iv), respectively. For the 30° static case (Fig. 30 (iii)), as expected, the flow is fully separated from the leading edge denoting deep stall;

however, for the dynamic case (Fig. 30 (iv)), at the same pitch angle of 30°, one can see the initiation of the dynamic stall vortex and the flow is still more or less attached. For the 45° static case shown in Fig. 30 (v), the flow is fully separated from the leading edge. However, for the dynamic case (Fig. 30 (vi)), the dynamic stall vortex has reached the full strength and is in the process of shedding. Comparing Fig. 30 (ii), (iv) and (vi) would provide insight into how the pitching amplitude affects the dynamic stall process on a cyclorotor blade at ultra-low Reynolds numbers. These PIV results clearly explain the reason for the large lift coefficients measured on a dynamic pitching blade at high amplitudes (Figs. 21 and 25).

Understanding Physics of Force Production on Cyclorotor Blade

The variation of lift and drag coefficients as a function of azimuth on a blade operating at ±30° pitch amplitude is shown in Figs. 31 and 32. As mentioned before the lift is the force in the radial direction (positive lift is radially outward) and drag is the force in the tangential direction (positive drag is opposite to the direction of blade motion). Fig. 33 shows the measured flowfield around the azimuth (Ψ) at a 10° resolution. On Figs. 31 and 32 the corresponding PIV figure numbers (Figs. 33 (i) – (xxxvi)) are provided at a resolution of 10°. Also, to improve clarity in the discussion, each of the flowfield images include the lift vector where the magnitude is proportional to the measured magnitude (Fig. 31 and 33) and the direction depends on the sign. Similar to what is shown in Fig.

18, the computed virtual camber chord-line is superimposed on the physical airfoil in Fig. 33 to aid in the explanation of the physics.

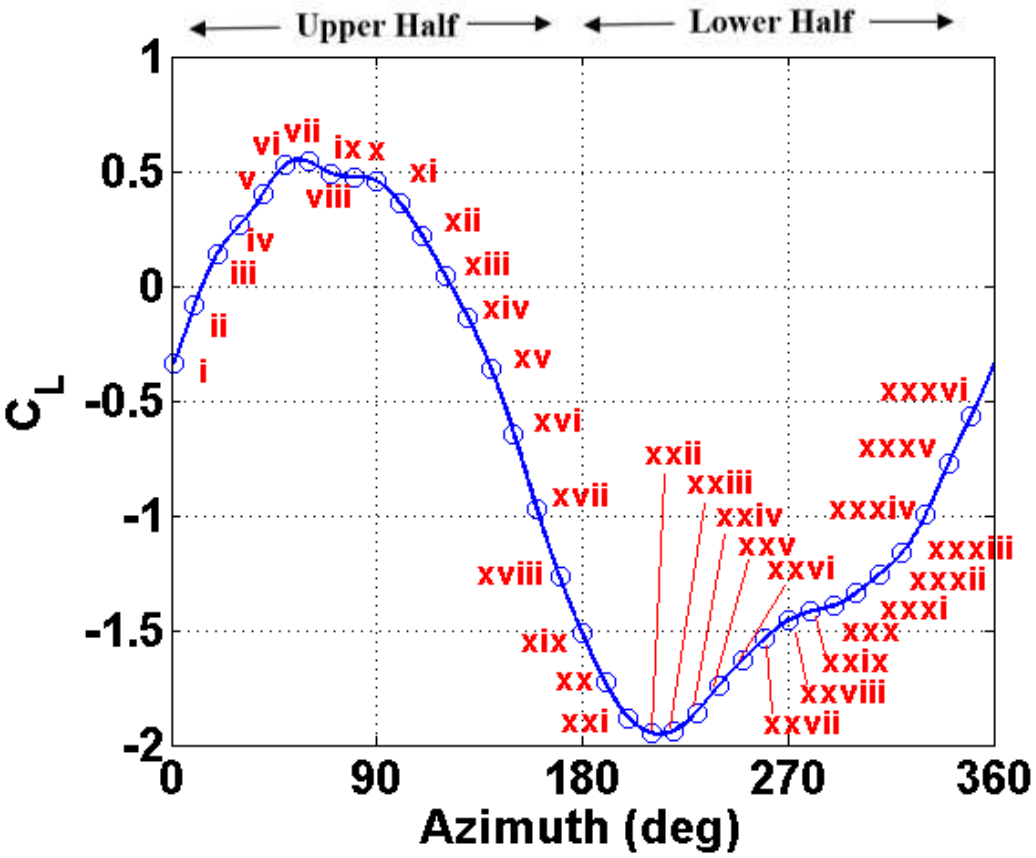

Fig. 31: Measured lift coefficient versus azimuth for ±30° dynamic pitching.

At 0° azimuth (Fig. 33 (i)), even though the airfoil is symmetric and pitch is zero, the small negative virtual camber shown in the figure creates a small negative lift. This can also be seen in Fig. 31. The direction of lift is also very evident from the flowfield around the airfoil. As seen from Fig. 32, the drag is very small and positive.

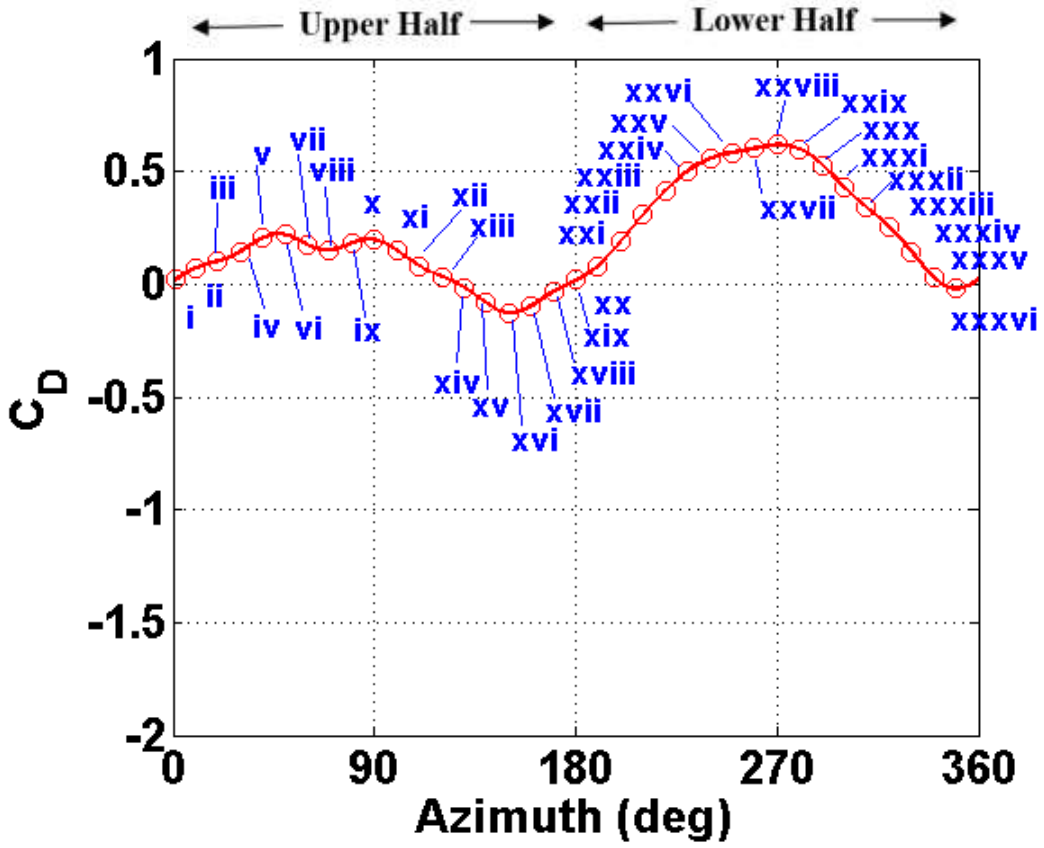

Fig. 32: Measured drag coefficient versus azimuth for ±30° dynamic pitching.

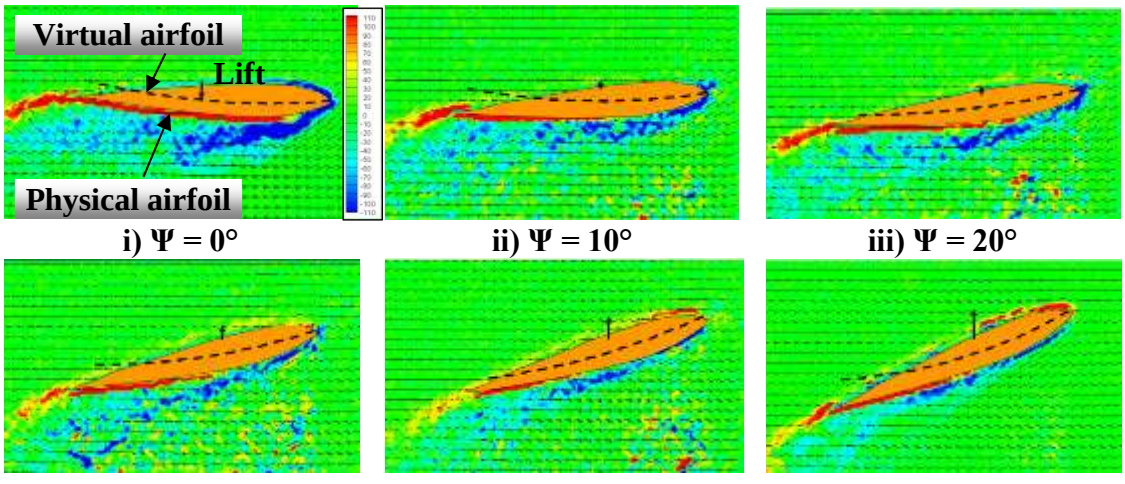

i) Ψ = 0° **ii) Ψ = 10°** **iii) Ψ = 20°**

iv) Ψ = 30° **v) Ψ = 40°** **vi) Ψ = 50°**

Fig. 33: PIV measurements at different azimuths for ±30° dynamic pitching.

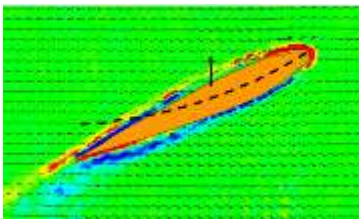

vii) Ψ = 60°

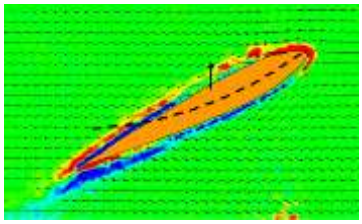

viii) Ψ = 70°

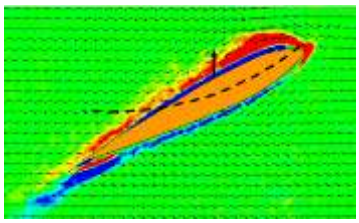

ix) Ψ = 80°

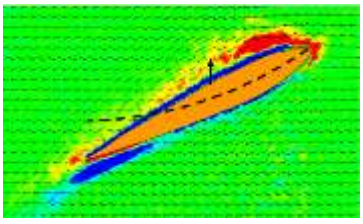

x) Ψ = 90°

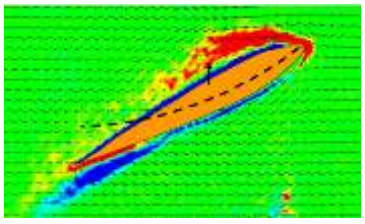

xi) Ψ = 100°

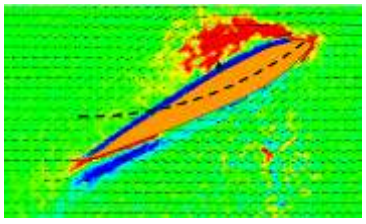

xii) Ψ = 110°

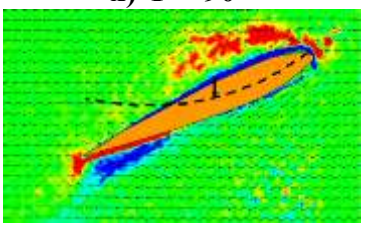

xiii) Ψ = 120°

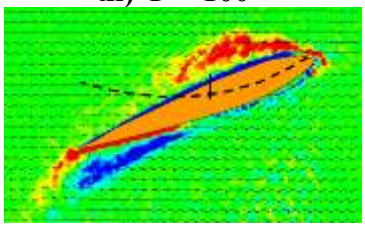

xiv) Ψ = 130°

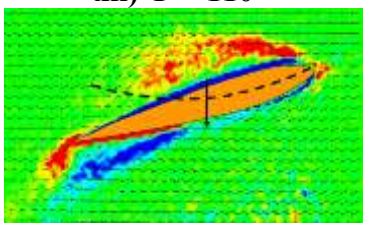

xv) Ψ = 140°

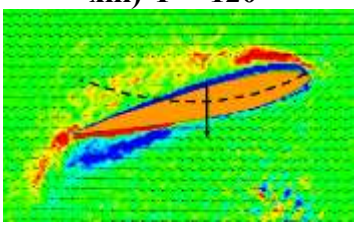

xvi) Ψ = 150°

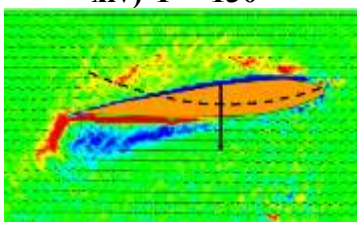

xvii) Ψ = 160°

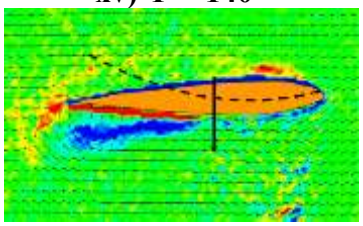

xviii) Ψ = 170°

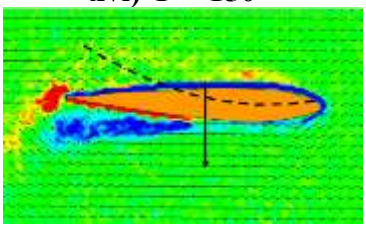

xix) Ψ = 180°

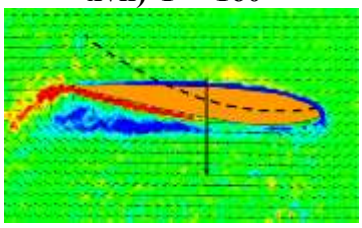

xx) Ψ = 190°

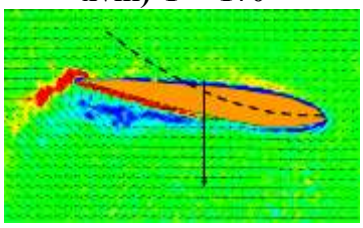

xxi) Ψ = 200°

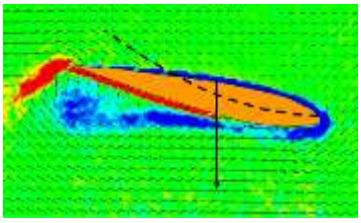

xxii) Ψ = 210°

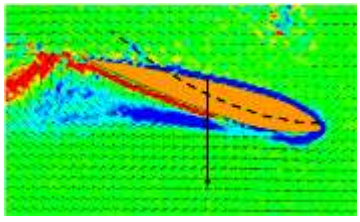

xxiii) Ψ = 220°

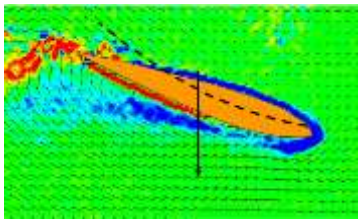

xxiv) Ψ = 230°

Fig. 33 (continued)

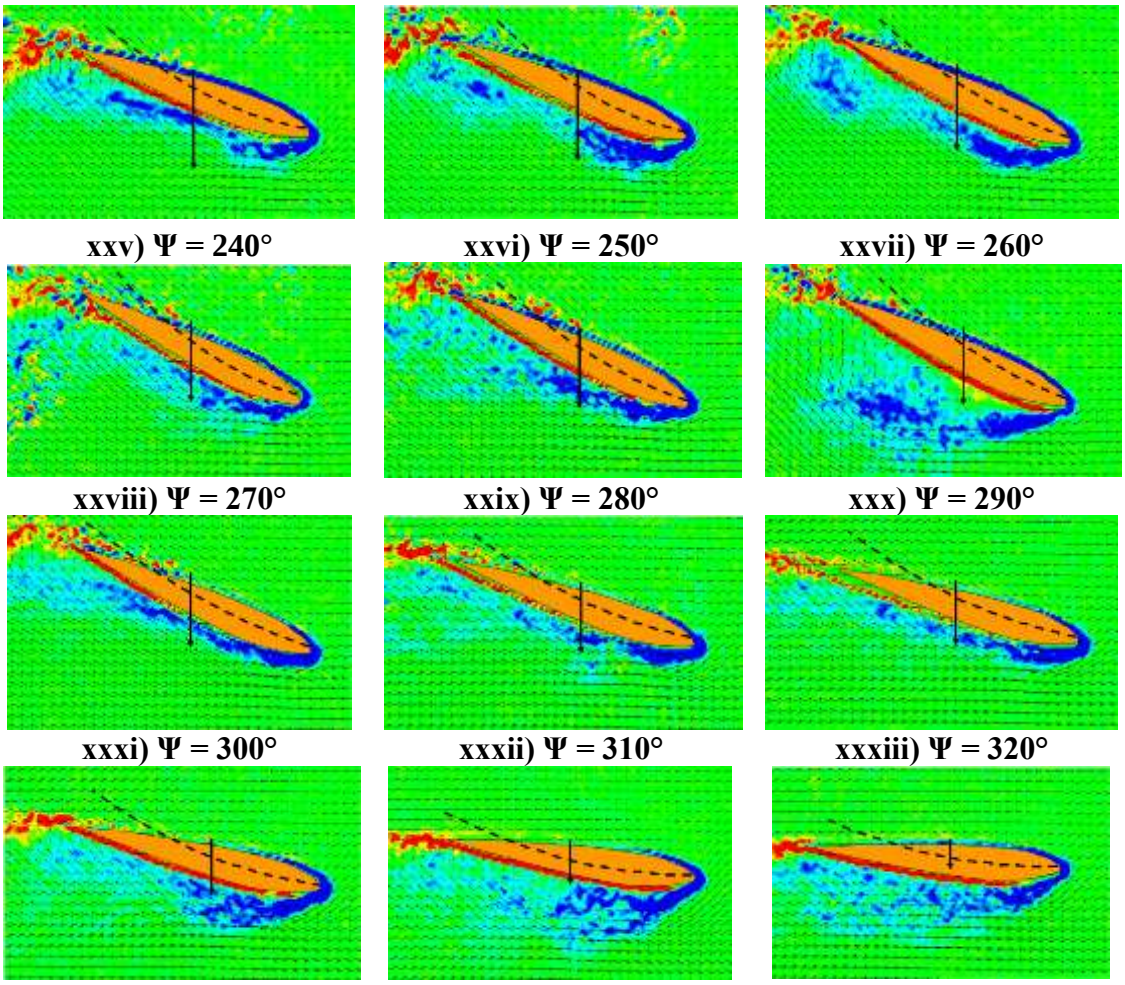

xxv) Ψ = 240° xxvi) Ψ = 250° xxvii) Ψ = 260°

xxviii) Ψ = 270° xxix) Ψ = 280° xxx) Ψ = 290°

xxxi) Ψ = 300° xxxii) Ψ = 310° xxxiii) Ψ = 320°

xxxiv) Ψ = 330° xxxv) Ψ = 340° xxxvi) Ψ = 350°

Fig. 33 (continued)

In Fig. 33 (ii), since the pitch is increasing in the positive direction, the negative lift is decreasing. It is interesting because the lift is downwards or negative due to the virtual camber as shown in the figure. In other words, here the virtual camber is in the reverse direction of the conventional camber and hence it will be called 'negative camber'. Typically, because of the positive pitch angle, the lift should be upwards or positive. However, in Fig. 33 (ii), the negative camber effect is more dominating than the effect of

positive pitch angle and hence results in a negative lift. Again, as before, the direction of lift is evident from the flowfield as well. The drag increases due to the increase in pitch angle (Fig. 32).

At the 20° azimuth location (Fig. 33 (iii)), the pitch angle has increased further and the lift is close to zero because the negative lift from negative virtual camber is nullified by positive pitch. This could be thought of as the zero-lift angle of attack for the virtually cambered airfoil. It is important to note that, as shown in Figs. 16 (i) and 18, the camber of the virtual airfoil changes from one azimuthal location to another. At 30° azimuth (Fig. 33 (iv)), the blade pitch is further increased and now positive lift is generated, which means the pitch is high enough to dominate negative virtual camber. As shown in Fig. 33 (v), the lift increases for the 40° azimuth because of the increase in blade pitch angle. At 50° azimuth (Fig. 31, 32 and Fig. 33 (vi)), both lift and drag reach a local maximum value. The blade camber has also increased significantly from the 0° azimuth.

Starting at 60° azimuth, the lift starts dropping even though the pitch angle is increasing. This may be because of the large increase in negative virtual camber and negative virtual incidence, which is reducing the effective angle of attack and the lift produced. However, more prominent than the drop in lift is the sudden local drop in drag. The reason for this can be traced back to the flowfield shown in Fig. 33 (vii), which shows the initiation of a vortex at the leading edge causing leading edge suction, which could reduce the net profile drag. Lift further decreases for the 70° azimuth (Fig. 33 (viii)) even though the pitch is increasing. Again, this occurs because of the large negative virtual camber and incidence from the reduced pitch rate. Drag drops further because of the

increased leading edge suction as seen from the vorticity contours in the flowfield. From the 70° to 80° azimuth (Fig. 33 (ix)), the lift stays almost constant (refer to Fig. 31). However, from the flowfield, a strong dynamic stall vortex can be seen. At this point it is unclear why the vortex lift does not significantly increase the blade lift (Fig. 31). However, there is a slight increase in drag (Fig. 32). At the 90° azimuthal location (Fig. 33 (x)), the blade reaches its maximum pitch angle. At this point, there is significant negative virtual camber and incidence, as well as a strong dynamic stall vortex forming on the leading edge. The flow remains more or less attached on the top even at such high pitch angles. The lift drops slightly, possibly due to the negative camber and incidence that is more effective than the additional vortex lift.

In Figures 33 (xi) – (xv), the 100° to 140° azimuthal locations show the shedding of the dynamic stall vortex and a reduction in the lift and drag (Figs. 31 and 32). It is also significant to note the large negative virtual camber and incidence for these cases. From the 110° to 120° azimuth, the direction of lift and drag changes from positive to negative (refer Figs. 30, 32, 33 (xii) and 33 (xiii)). This is because the negative virtual camber and incidence have increased to such an extent that it dominates even large positive pitch angles. This clearly shows the strong effect of dynamic virtual camber on the force production of a cyclorotor blade. Interestingly the drag (tangential force) becomes negative, indicating power extraction from the 115° to 170° azimuthal locations. From 150° (Fig. 33 (xvi)) to 180° (Fig. 33 (xix)), there is large negative lift, which continues to increase due to the strong negative virtual camber.

As seen from Figs. 16 (i), 18, and 33 (xix), the maximum virtual camber occurs at the 180° azimuth, causing a huge negative lift force, even with a symmetric airfoil and physical pitch angle of zero. Again, the direction of lift is evident from the flowfield. The drag also increases as shown in Fig. 32. At the 190° azimuth, as seen from Fig. 33 (xx), the camber is consistent with the blade pitch angle and is called 'positive camber'. In the entire lower half (180° to 360°) the camber will not oppose the pitch angle, which is the case in the upper half (0° to 180°). In the entire lower half, the lift will be negative because it will be acting radially inwards towards the center of the rotor. From the 190° to 220° azimuthal locations (Figs. 31, 33 (xx) – (xxiii)) the magnitude of negative lift keeps increasing due to the positive camber. Also, from the flowfield, a strong trailing edge separation can be seen, which increases with increasing pitch angle.

From the 220° to 270° azimuth, the magnitude of negative lift starts decreasing but the drag coefficient keeps increasing until it reaches a maximum value of 0.6 at the 270° azimuth. At this position the blade attains the maximum pitch angle. The 230° azimuth (Fig. 33 (xxiv)) shows a weak dynamic stall vortex beginning to appear on the leading edge. It is weaker in nature mostly because virtual camber is positive and hence decreases flow separation (unlike the upper half where the camber was negative or reverse camber). For azimuths of 240° – 260° (Figs. 33 (xxv) – (xxvii)) the dynamic stall vortex builds up strength. There is a mild shedding at approximately 270° (Fig. 33 (xxviii)). The vortex is fully separated at the 290° azimuth (Fig. 33 (xxx)). During this time, the magnitude of effective angle of attack is very high causing large lift and drag. It is also important to note that even though the pitching is symmetric, the dynamic stall process in the upper and

lower half of the circular trajectory is completely different because of the complete reversal of dynamic virtual camber from the upper to lower half. From the 300° to 320° azimuth (Fig. 33 (xxxi) – (xxxiii)), the flow again starts re-attaching as pitch decreases. The magnitude of lift and drag decreases as seen from Figs. 31 and 32. However, from the 330° to 350° azimuth (Figs. 33 (xxxiv) – (xxxvi)), the shedding of a secondary leading edge vortex can be seen. The reason for this is not completely understood at this point. Finally, at 360° (Fig. 33 (i)), the flow reattaches again.

A key insight gained from these measurements is the interplay of blade pitch angle and dynamic virtual camber in the blade force production. In the entire upper half, the pitch angle and virtual camber oppose each other, unlike the lower half where they act in the same direction. This leads to completely different dynamic stall process in the upper and lower halves. This can also explain why a huge improvement in cyclorotor performance is obtained using asymmetric blade pitching (Ref. 6), where the pitch angle in the upper half increased and decreased in the lower half.

Power Calculations

Also of interest is the power consumption of a dynamic pitching cyclorotor blade. Figure 34 shows the measured instantaneous blade power breakdown for the ±45° dynamic pitching case at 40 RPM as a function of azimuth. Included in the plot are the power required for the blade to rotate, the power required for the blade to pitch, and the total power.

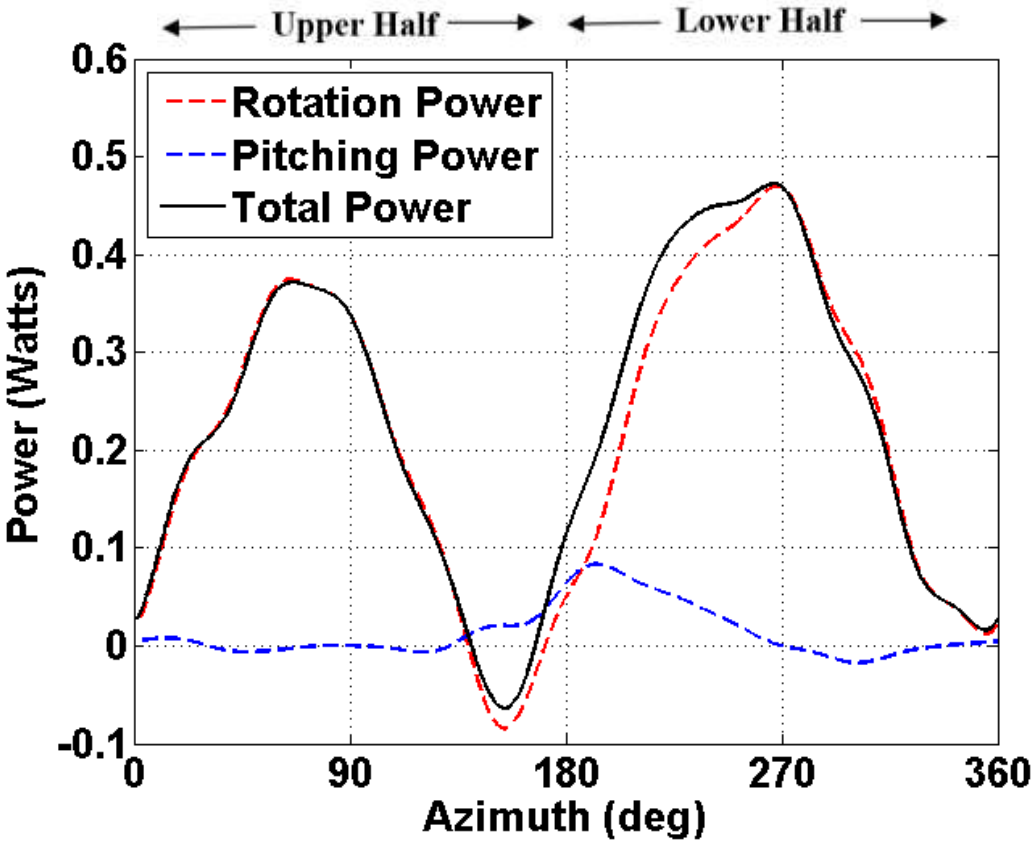

Fig. 34: Measured blade power versus azimuth for ±45° pitching.

These are calculated using the following equations:

$$Rotation\ power\ \ (P_{ROT}) = D\Omega R \qquad \text{(Eq 5)}$$

$$Pitching\ power\ (P_{PITCH}) = M_Z\dot{\theta} \qquad \text{(Eq 6)}$$

$$Total\ power = P_{ROT} + P_{PITCH} \qquad \text{(Eq 7)}$$

where D is the measured tangential force, which is referred to as the drag force in this paper, ΩR is the rotational velocity, M_Z is the measured pitching moment, and $\dot{\theta}$ is the measured pitch rate.

It is clear from Fig. 34 that most of the power is required for the blade rotation and not pitching. The present study conclusively proves that it only takes up a very small fraction of the total aerodynamic power to dynamically pitch the blades at least at such low Reynolds numbers. Figure 35 shows the instantaneous total blade power versus the azimuth for all of the dynamic pitching cases. It can be seen that, as expected, the power continues to increase as the dynamic pitching amplitude increases. In fact for a small part of the azimuthal cycle the blade power is negative or blade is extracting power.

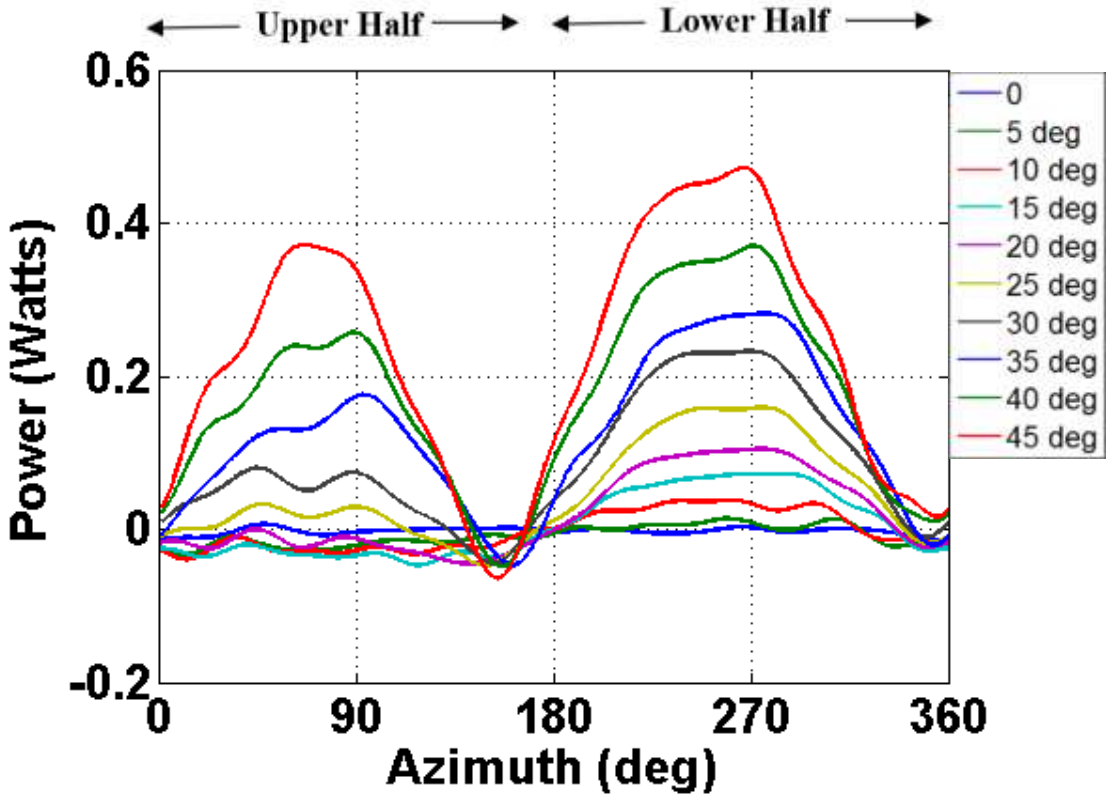

Fig. 35: Measured blade power versus azimuth for ±0° to ±45° dynamic pitching.

The cycle-averaged power versus the pitching amplitude for all the dynamic pitching cases is plotted in Fig. 36. As seen from the figure, the power increases quadratically with the pitching amplitude. For the pitching amplitudes of 5° and 10° the power is slightly negative denoting power extraction or negative induced power in a cycle-averaged sense. Similarly, for 0°, the average power is close to zero may be because the component of lift vector in the forward direction (causing negative induced power) cancels out the profile power. From 20° to 45° the power increases rapidly until it reaches a maximum of about 0.24 Watts.

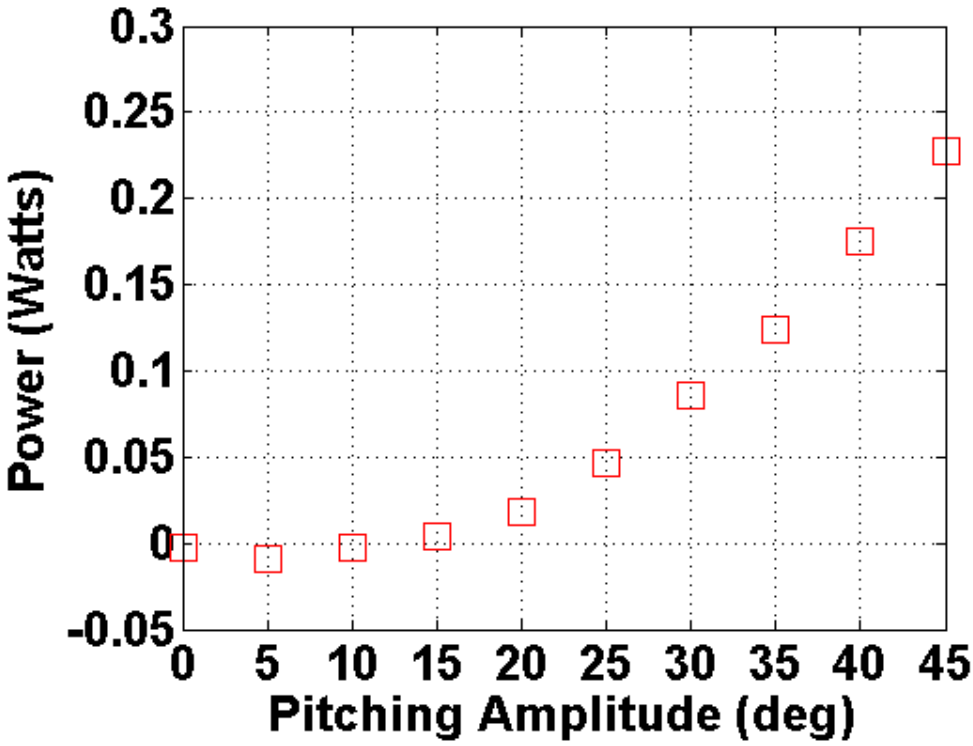

Fig. 36: Cycle-averaged blade power versus blade pitching amplitude.

In Figure 37 the cycle-averaged thrust is plotted against the dynamic pitching amplitude. The cycle-averaged thrust (T) is computed as follows:

$$T = \sqrt{{F_Z}^2 + {F_Y}^2} \qquad \text{(Eq 8)}$$

where F_Z and F_Y are vertical and horizontal components (in the fixed frame, refer Fig. 2) of measured radial and tangential forces. As seen from the figure, there is a nonlinear relationship between the average thrust produced by the rotor and the dynamic pitching amplitude.

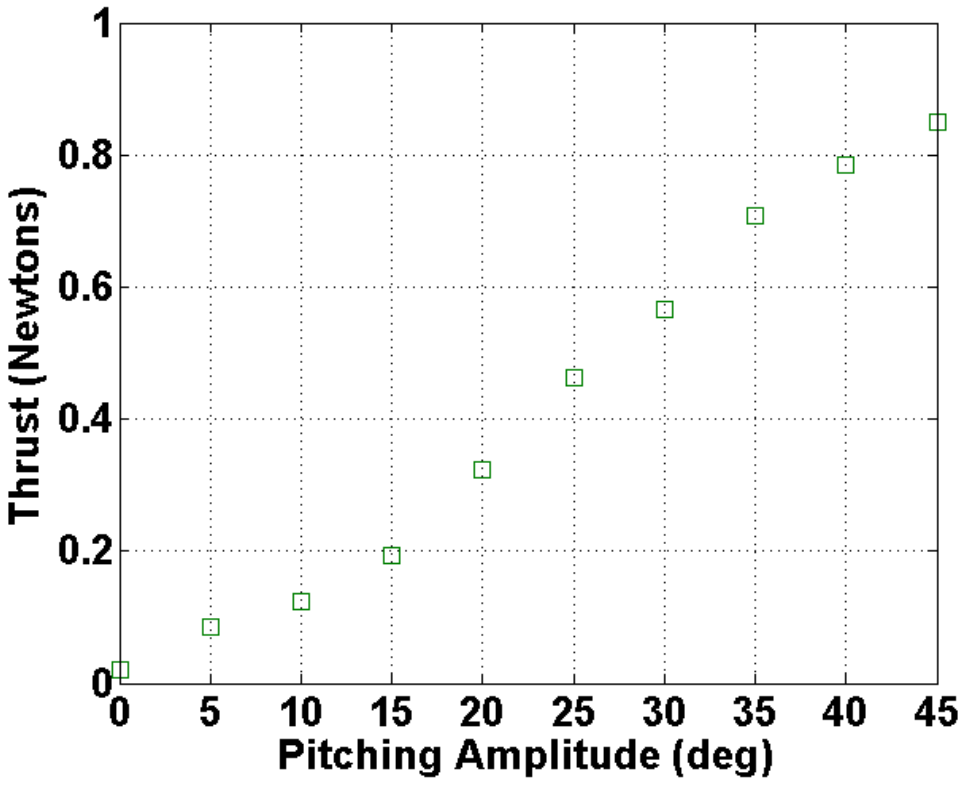

Fig. 37: Cycle-averaged thrust versus blade pitching amplitude.

Figure 38 has the cycle-averaged thrust to power ratio as a function of pitching amplitudes of 25° to 45°. It can be seen that the power loading decreases with respect to the pitching amplitude. The unusually high power loading values can be attributed to extremely low disk loading at which the present rotor is operating. For the 45° pitching amplitude, based on the rectangular projected area of the rotor, the disk loading is around 16 N/m^2 (0.33 lb/ft^2), which is extremely low.

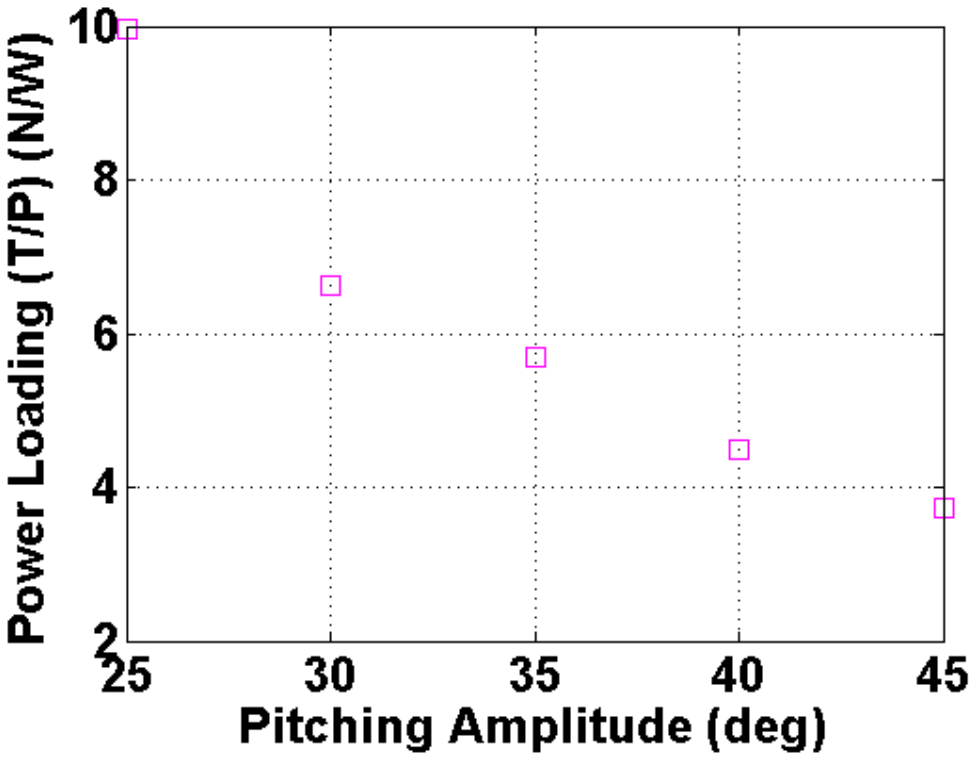

Fig. 38: Cycle-averaged power loading (T/P) versus blade pitching amplitude.

The decrease in power loading with pitch amplitude can be attributed to the fact that the disk loading is increasing and the figure of merit is decreasing with pitch amplitude. The figure of merit (*FM*) is defined as following:

$$FM = \frac{P_{IDEAL}}{P_{MEASURED}} \qquad \text{(Eq 9)}$$

P_{IDEAL}, the ideal power, is given as:

$$P_{IDEAL} = Tv_i \qquad \text{(Eq 10)}$$

where v_i, the induced velocity calculated as follows:

$$v_i = \sqrt{\frac{T}{2\rho A}} \qquad \text{(Eq 11)}$$

where ρ is the density of water and A is the rectangular projected area of the rotor ($A = b \times d$), where b is the blade span and d is the cyclorotor diameter.

The figure of merit is plotted as a function of pitch amplitude in Fig. 39. It can be seen that *FM* drops with pitch amplitude; however, for a pitch amplitude of ±25°, the *FM* is around 0.65, which is very high considering the ultra-low Reynolds numbers (Re~18,000) at which the blade is operating. However, as seen from Fig. 39, for a pitch amplitude of ±45°, the *FM* is around 0.34. This decrease in *FM* is mainly due to the higher drag coefficient (Fig. 26) which the blade experiences at larger blade pitching angles.

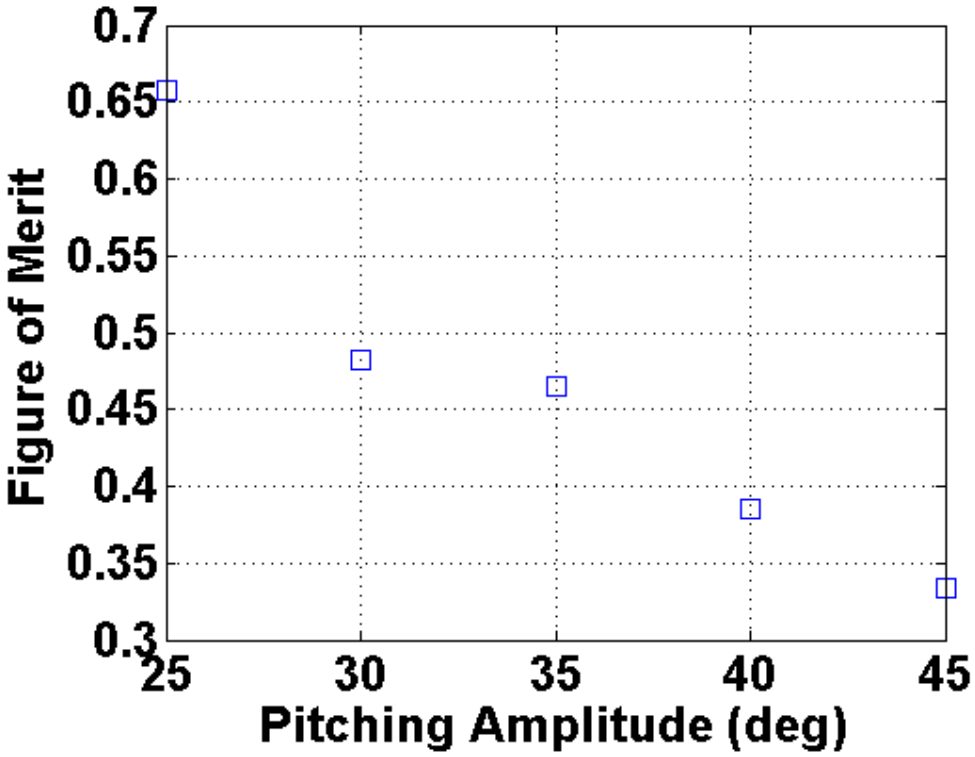

Fig. 39: Figure of merit versus blade pitching amplitude.

CHAPTER V

RESULTS: ASYMMETRIC PITCHING AND REYNOLDS NUMBER EFFECT

In the previous sections, the cyclorotor performance with symmetric pitching kinematics was studied. As shown in the previous sections there are considerable dissimilarities in aerodynamic environment experienced by the blade between the upper and lower halves due to the flow curvature effects (virtual camber and incidence) and the differences in inflow velocities. Therefore, it is logical to have different blade pitch kinematics in the upper and lower halves, which is referred to as 'asymmetric pitching' in this section.

Figures 40 – 42 show the measured blade pitch angle, lift coefficient, and drag coefficient versus the azimuth, respectively, for the following 60° peak-to-peak amplitude cases: 15° Top/ 45° Bottom, 20° Top/ 40° Bottom, 25° Top/ 35° Bottom, 30° Top/ 30° Bottom, 35° Top/ 25° Bottom, 40° Top/ 20° Bottom, and 45° Top/ 15° Bottom. As seen previously in Fig. 18, the blade pitch is positive in the upper half which results in reverse or negative virtual camber, and pitch is negative in the lower half resulting in positive camber. In the symmetric 30° Top/ 30° Bottom pitch case, as shown previously, asymmetry between the upper and lower halves could be seen clearly for both the lift and drag coefficients (Figs. 41 and 42). The lift and drag are lower in the upper half due to the negative camber and higher in the lower half due to positive camber.

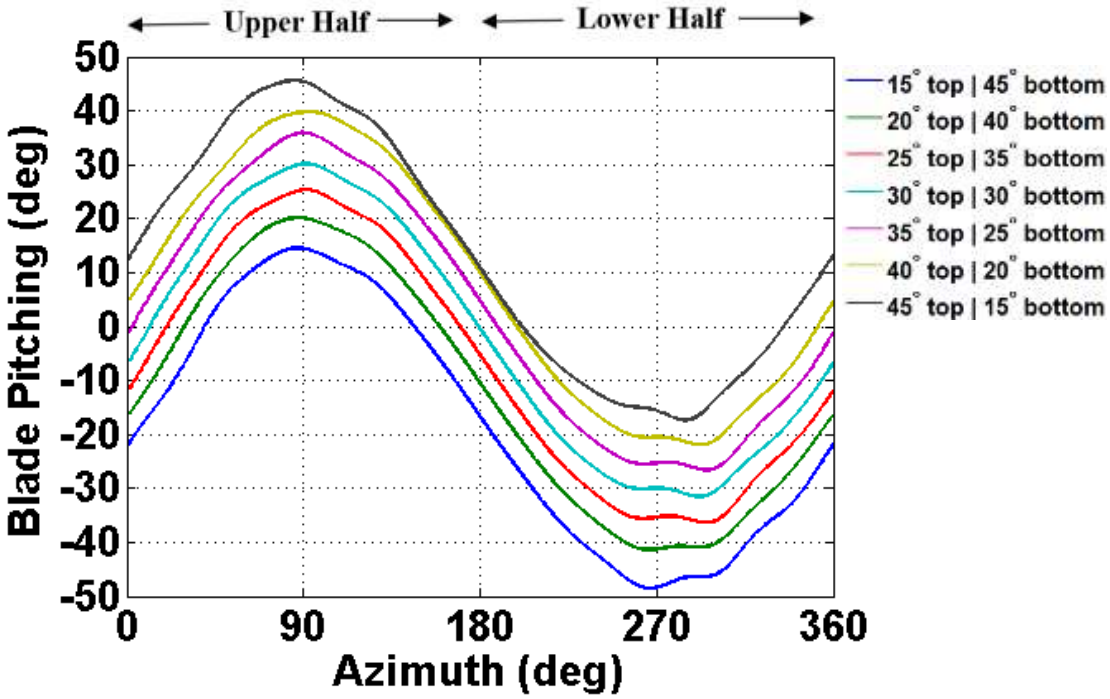

Fig. 40: Measured blade pitch versus azimuth for 60° peak-to-peak asymmetric pitching.

Now, as seen from Figs. 41 and 42, when the pitch angle at the upper half is decreased and lower half increased from the symmetric case (15° Top/ 45° Bottom, 20° Top/ 40° Bottom, 25° Top/ 35° Bottom), the asymmetry grows even further. Therefore, with the goal of making the force distribution more uniform across the azimuth, the pitch angle at the top was increased and the bottom was decreased from the symmetric case (35° Top/ 25° Bottom, 40° Top/ 20° Bottom, and 45° Top/ 15° Bottom), which, as expected, increased the lift and drag on the top and decreased it on the bottom resulting in a more uniform force production between the upper and lower halves. The 40° Top/ 20° Bottom case produced an approximately symmetric lift distribution between the upper and lower

halves (Fig. 41) and the 35° Top/ 25° Bottom case produced similar drag coefficients in upper and lower halves (Fig. 42). This clearly shows the significant role of asymmetric pitching on the force production on a cycloidal rotor blade. To better examine and compare the performance of the asymmetric cases it is important to look at the power calculations, which is presented in the next section.

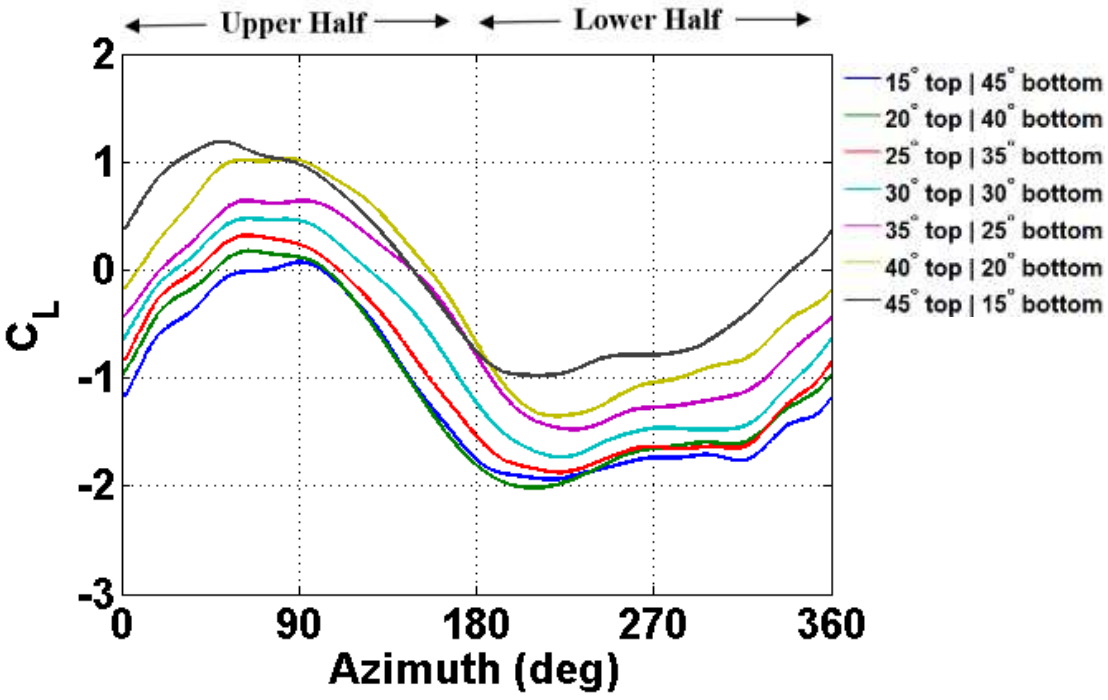

Fig. 41: Measured lift coefficient versus azimuth for 60° peak-to-peak asymmetric pitching.

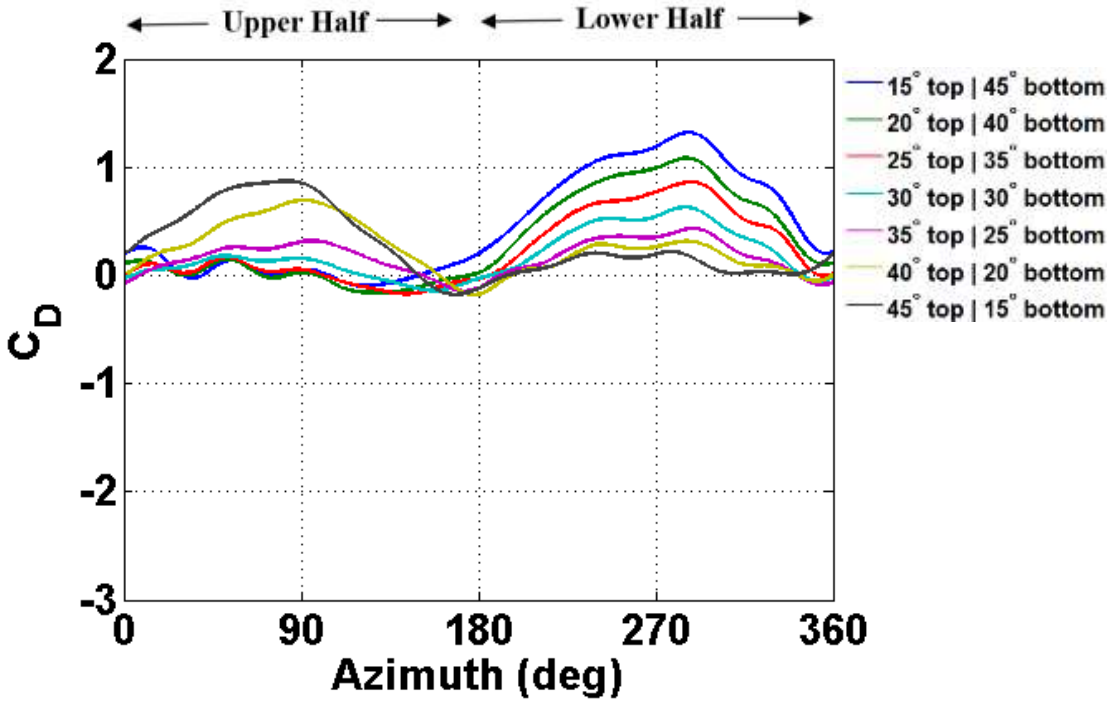

Fig. 42: Measured drag coefficient versus azimuth for 60° peak-to-peak asymmetric pitching.

Asymmetric Pitching Power Calculations

Figure 43 shows the instantaneous total blade power versus the azimuth for the 60° peak-to-peak symmetric and asymmetric pitching cases. The power includes both the roational power and blade pitching power and the methodology for calculating power is discussed in the previous sections. As shown before, since the power for a cycloidal rotor blade is dominated by the rotational power, the the azimuthal power distribution shown in Fig. 43 would strongly correlate with the drag distribution in Fig. 42. Increasing the blade

pitch in the upper half and decreasing the pitch in the lower half would make the power distribution more uniform. Similar to the drag case, the 35° Top/ 25° Bottom case required almost the same power in the upper and lower halves (Fig. 43).

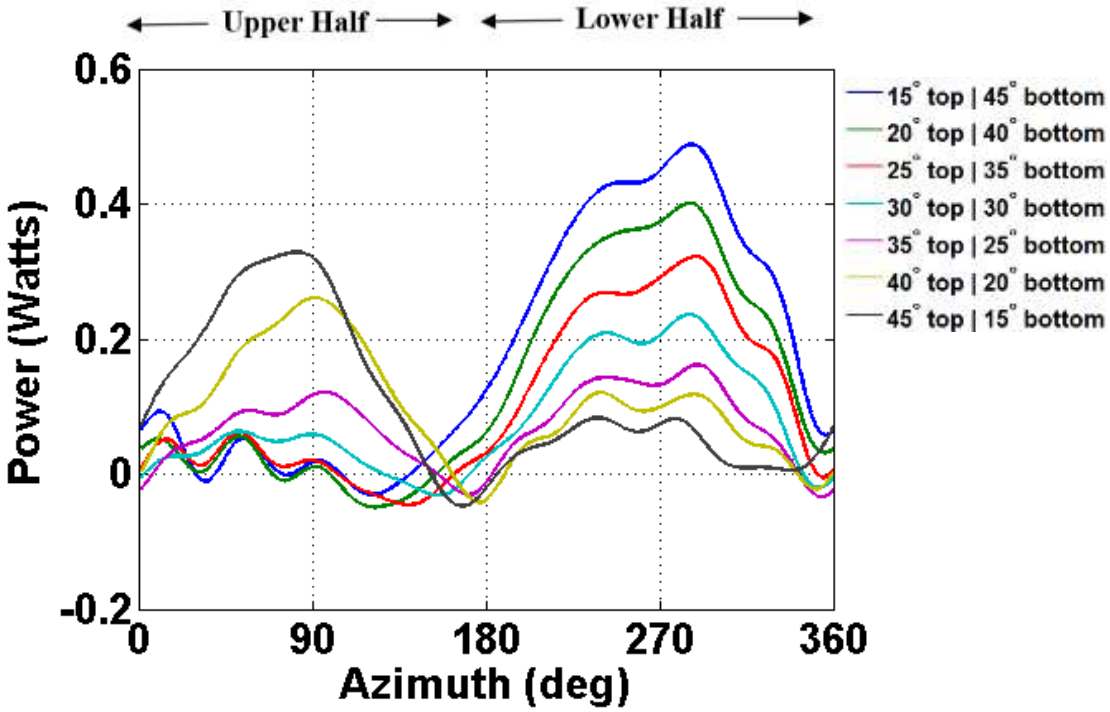

Fig. 43: Measured instantaneous blade power versus azimuth for 60° peak-to-peak asymmetric pitching.

The cycle-averaged blade power is plotted in Fig. 44 for each of the 60° peak-to-peak asymmetric pitching cases. As can be seen in the figure, the power required is maximum for the 15° Top/ 45° Bottom case (Fig. 44), which had the most asymmetric distribution of power between the upper and lower halves. The large amount of power

required for this case can be attributed to the high drag coefficients seen in the lower half of the trajectory (Fig. 42). On the other hand, the power required is minimum for the 35° Top/ 25° Bottom case (Fig. 44).

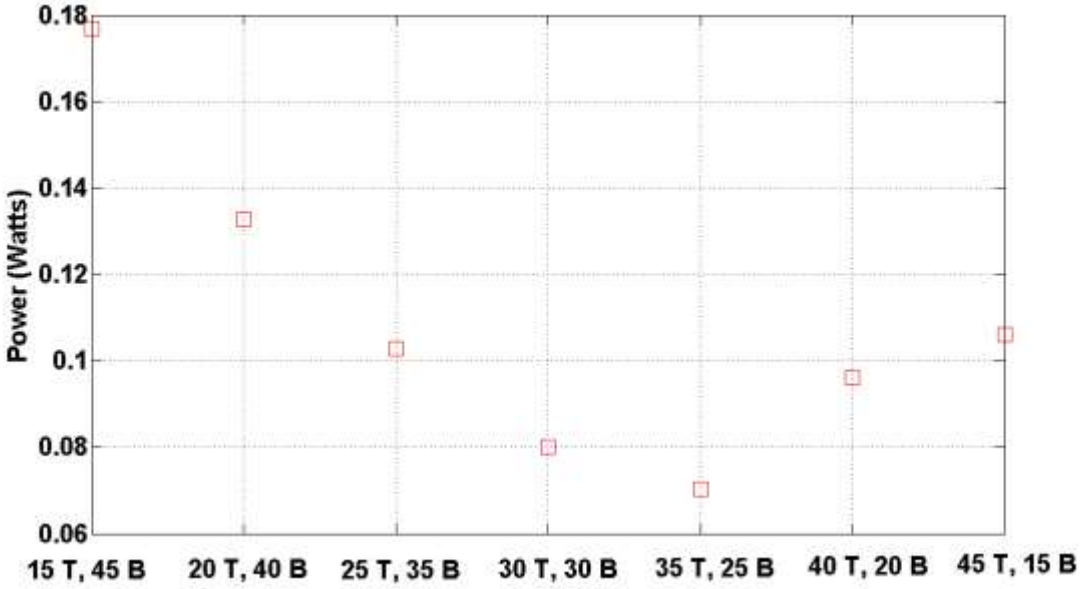

Fig. 44: Cycle-averaged blade power for each 60° peak-to-peak asymmetric pitching case.

Figure 45 has the cycle-averaged thrust to power ratio for each of the asymmetric pitching cases. Unlike the symmetric cases where the power loading decreased with respect to the pitching amplitude (Fig. 38), the asymmetric power loading varies with the asymmetric pitching cases in a quadratic manner. It is clear from the figure that the 35° Top/ 25° Bottom case has the highest power loading of approximately 7.6 (Fig. 45).

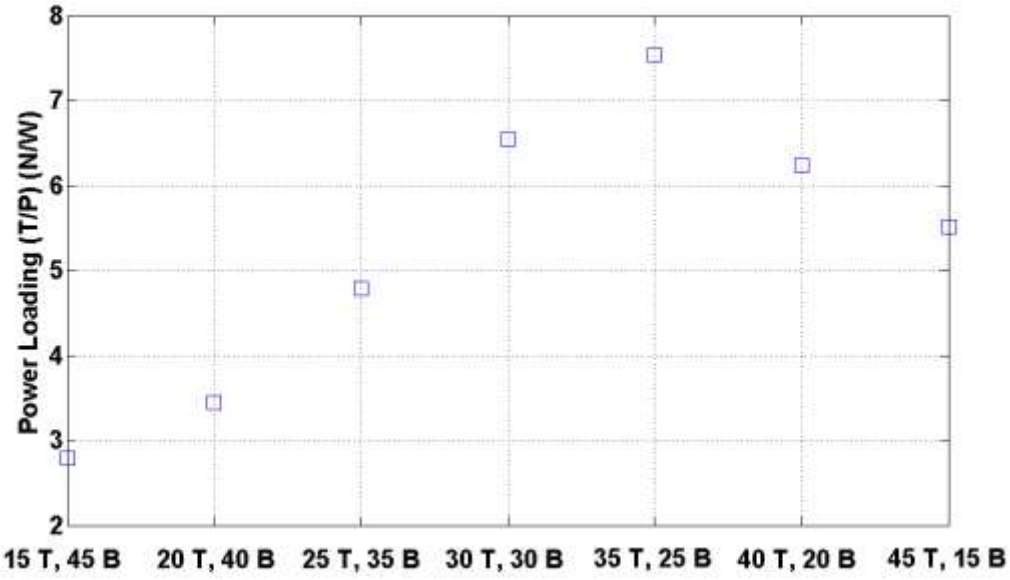

Fig. 45: Cycle-averaged power loading (T/P) for each 60° peak-to-peak asymmetric pitching case.

The figure of merit is plotted as a function of the asymmetric pitching cases in Fig. 46. It can be seen that the *FM* shows a similar trend to the power loading, where it varies quadratically with the asymmetric pitching cases. The maximum *FM* occurs for the 35° Top/ 25° Bottom case with a value of about 0.54. As mentioned for the symmetric pitching *FM* results, this value is especially high considering the ultra-low Reynolds numbers the cyclorotor is operating at. The lowest *FM* occurs for the 15° Top/ 45° Bottom case, which can be attributed to the large amount of drag present in the lower half (Fig. 42).

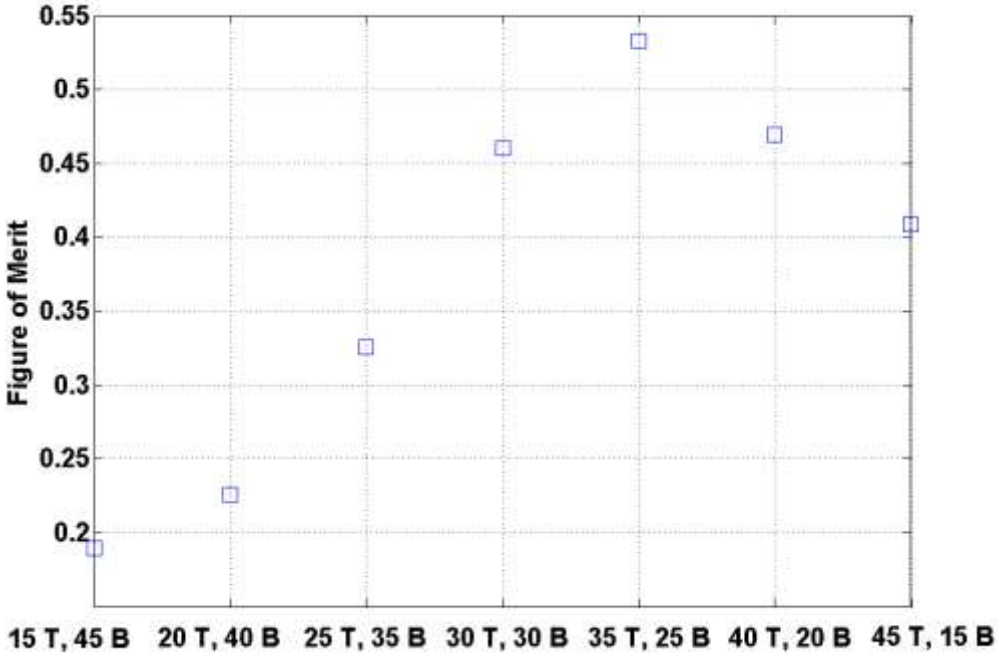

Fig. 46: Figure of merit for each 60° peak-to-peak asymmetric pitching case.

To further understand why the 15° Top/ 45° Bottom and 35° Top/ 25° Bottom cases have the worst and best performance, respectively, it is important to look at the flowfield for specific azimuthal locations. Figs. 47 and 48 show the lift and drag coefficients as a function of azimuth for the 30° Top/ 30° Bottom case (symmetric pitching), in addition to the two asymmetric cases in question, namely, 15° Top/ 45° Bottom and 35° Top/ 25° Bottom. Fig. 49 shows the measured flowfield around the blade at some key azimuthal locations where the blade reaches maximum positive and negative pitch angles, resulting in dynamic stall and therefore produces the maximum forces. The locations included 80°, 90°, 100°, 110°, 240°, 250°, 260°, 270°, 280°, 290°, and 300°. To

aid in the analysis, Figs. 47 and 48 are also labelled with the figure number for the corresponding flowfield image at each azimuth (Figs. 49 (i) – (xxxiii)).

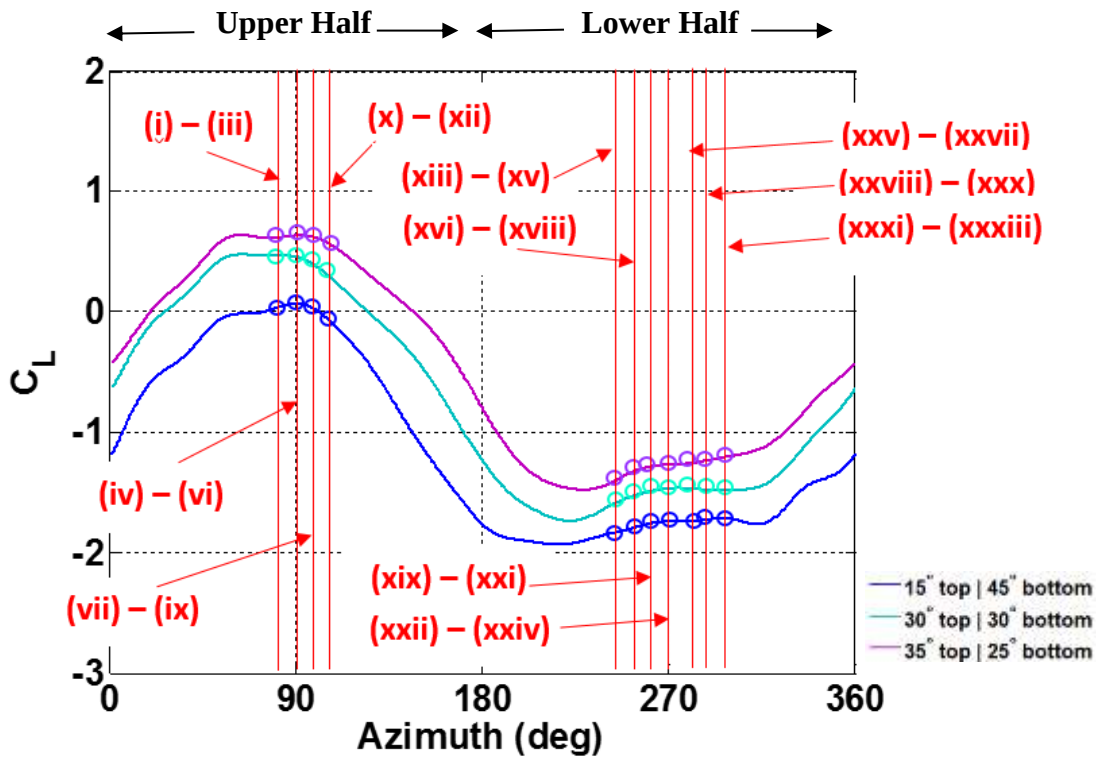

Fig. 47: Measured lift coefficient versus azimuth for 60° peak-to-peak asymmetric pitching.

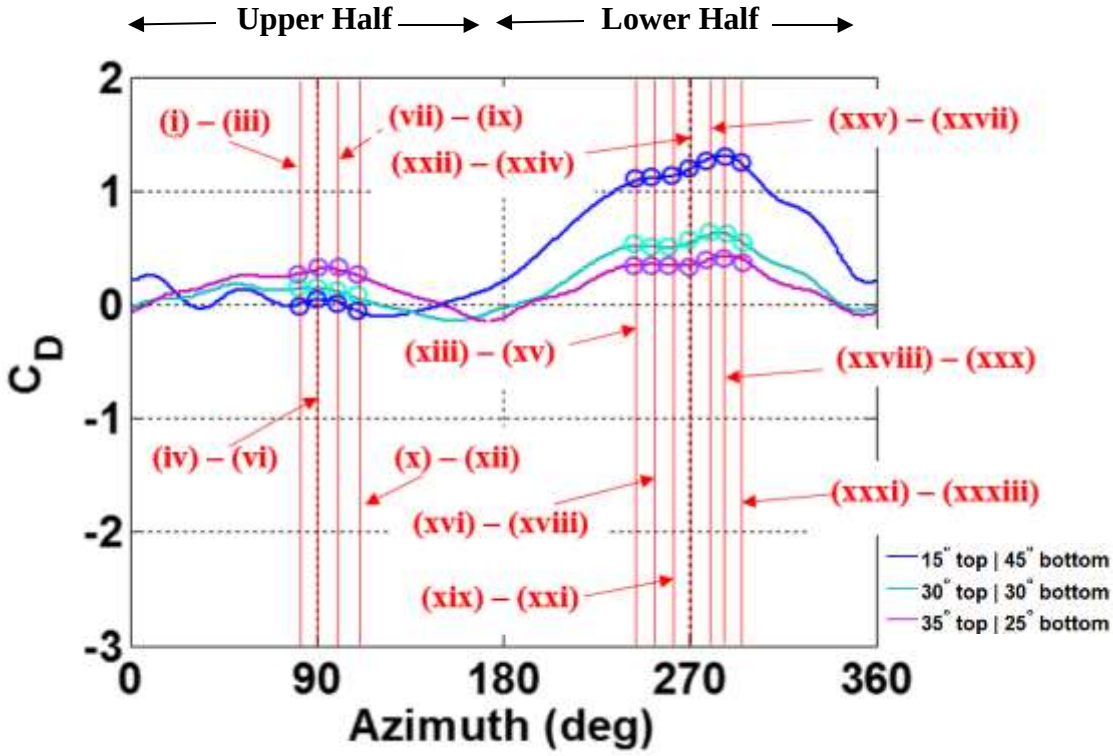

Fig. 48: Measured drag coefficient versus azimuth for 60° peak-to-peak asymmetric pitching.

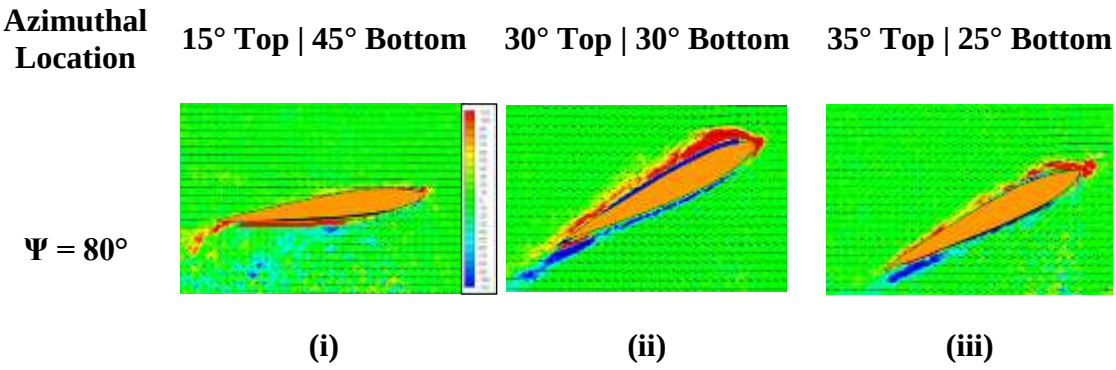

Fig. 49: PIV measured flow velocity vectors and vorticity contours at different azimuthal locations for 60° symmetric and asymmetric pitching.

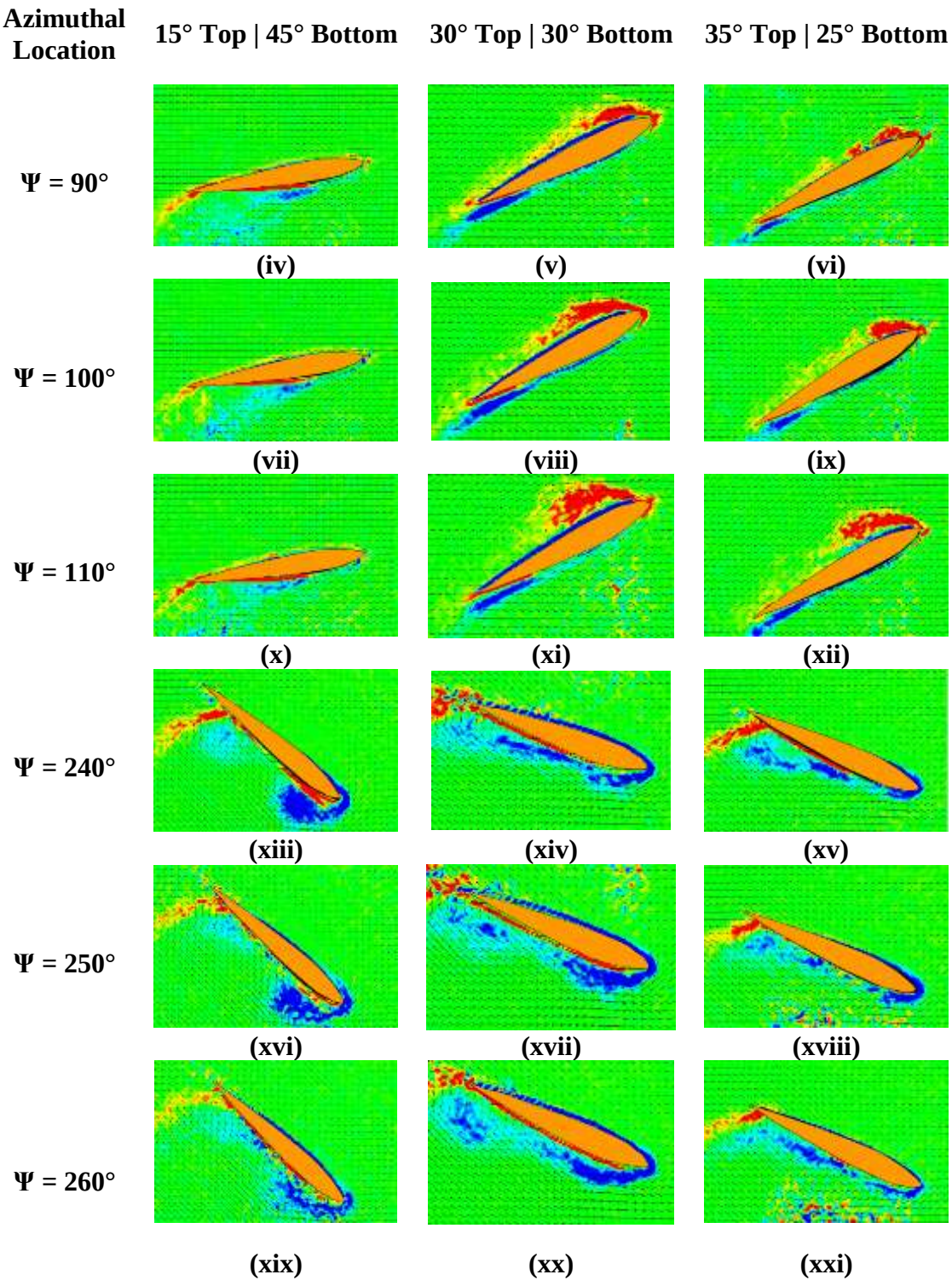

Fig. 49 (continued)

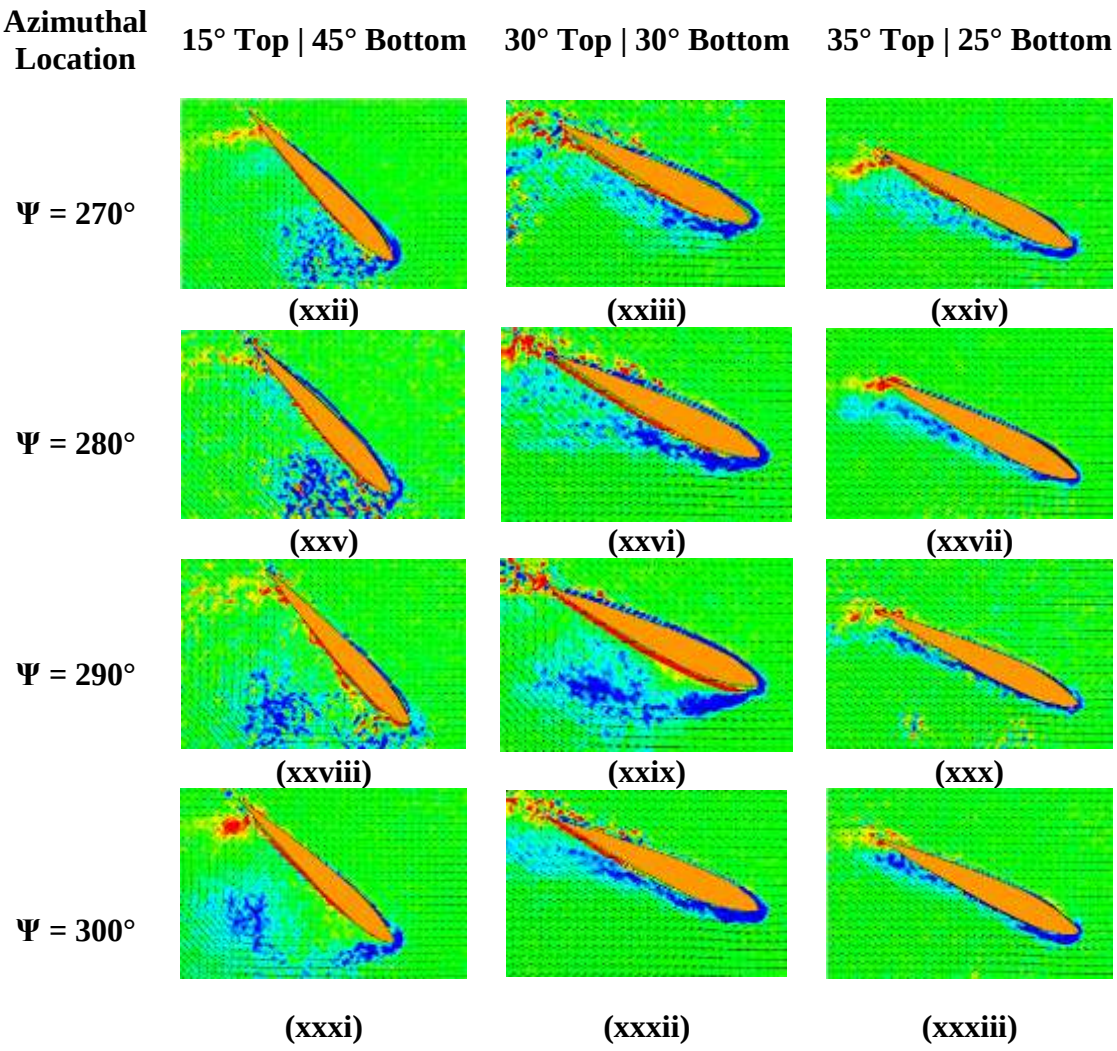

Fig. 49 (continued)

At the 80° azimuth, the lift coefficient for symmetric pitching and the 35° Top/ 25° Bottom case is positive, and for the 15° Top/ 45° Bottom case is zero (Fig. 47 (i – iii)). Similarly, the drag coefficient is small and positive for symmetric pitching and the 35° Top/ 25° Bottom case, but is zero for the 15° Top/ 45° Bottom case (Fig. 48 (i – iii)). This can be seen in the flowfield as well, for the flow is fully attached for the 15° Top/ 45°

Bottom case, whereas slight vortex development can be seen on the leading edge for the symmetric and 35° Top/ 25° Bottom cases (Fig. 49 (i – iii)). This is expected because the blade pitch angle is smallest for the 15° Top/ 45° Bottom case in the upper half of the azimuth, and the negative camber will counteract the small positive pitch angle resulting in almost zero lift. At the 90° azimuth, the blade pitch angle has increased and is at its maximum in the upper half of the trajectory. The vortex has grown slightly for the symmetric and 35° Top/ 25° Bottom cases, and the flow is still fully attached for the 15° Top/ 45° Bottom case (Fig. 49 (iv – vi)). The lift and drag has also increased for all three cases (Figs. 47 and 48 (iv – vi)), which is indicative of the blade force production being influenced by the blade pitch angle.

From the 100° to 110° azimuth, the lift and drag decrease for all three cases ((Figs. 47 and 48 (vii – xii)), which is expected as the blade pitch angle has reached its maximum and is beginning to decrease. The dynamic stall phenomena can be seen for the symmetric and 35° Top/ 25° Bottom case (Fig. 49 (vii – xii)); however, the flow stays fully attached for the 15° Top/ 45° Bottom case ((Figs. 47 and 48 (iv – vi)). As discussed in prior sections, positive pitch angles should result in positive lift for a symmetric blade. However, due to negative virtual camber, the blade produces negative lift even in positive pitch. Therefore, the negative virtual camber effect dominates the effect of blade pitch angle in the force production during the upper half for the 15° Top/ 45° Bottom case.

In the bottom half, the azimuthal range of 240° to 300° was selected for the flowfield measurements because the blade attains the maximum negative pitch angle at 270° azimuth resulting in unique flow characteristics in this range. At 240°, the lift

coefficients for all three cases are negative because lift the vector is pointing inwards toward the center of the rotor (Fig. 47 (xiii – xv)) and this is a negative force by convention. The 15° Top/ 45° Bottom case has the greatest negative lift, due to its much larger blade pitch angle in the bottom half of the azimuth. The drag coefficient has also increased significantly from the upper half for all three cases, with the 15° Top/ 45° Bottom case having the largest magnitude (Fig. 48 (xiii – xv)). This increase is due to a combination of the blade pitch angle and positive virtual camber. As was discussed in the symmetric pitching section, the blade pitch angle and virtual camber act in the same direction in the lower half of the cycle, which further increases the lift and drag coefficients in that region. The flowfield for the 35° Top/ 25° Bottom and symmetric pitching cases are very similar in that they both display mild flow separation at the leading edge, and then flow re-attachment towards the trailing edge (Fig. 49 (xiv - xv)). The flowfield for the 15° Top/ 45° Bottom case, however, exhibits a strong dynamic stall vortex (shown in blue) developing off the leading edge (Fig. 49 (xiii)). At 250° the vortex appears to weaken and begins shedding over the blade (Fig. 49 (xvi)), which corresponds to the decreased negative lift coefficient seen in Fig. 47 (xvi). The symmetric case at this azimuth shows a small vortex developing on the leading edge, with the flow re-attaching towards the trailing edge (Fig. 49 (xvii)). A much smaller vortex is also seen developing on the leading edge for the 35° Top/ 25° Bottom case, with some minor flow separation towards the trailing edge (Fig. 49 (xviii)). The difference in leading edge vortex size between the symmetric and 35° Top/ 25° Bottom case is evident in the lift and drag coefficient plots ((Figs. 47 and 48 (xvii – xviii)), with the larger vortex case resulting in the largest negative

lift and largest drag of the two. This magnitude difference is due to the effect of blade pitch angle; in this case, the larger vortex was present for the case with the larger blade pitch angle in the lower half.

From 260° to 270°, the lift coefficients decrease in magnitude for all three cases ((Fig. 47 (xix – xxiv)). This is fascinating because one expects the lift to continue to increase in magnitude as the blade pitch angle increases. The drag coefficient does appear to increase slightly, however, which is due to the blade pitch angle increase ((Fig. 48 (xix – xxiv)). For the 15° Top/ 45° Bottom case, the dynamic stall vortex is seen to increase in size but is weak in nature (Fig. 49 (xix and xxii)), which could explain the reason for the decrease in negative lift. The symmetric pitching case shows further development of the vortex on the leading edge, with the flow remaining mostly attached throughout (Fig. 49 (xx and xxiii)), and the 35° Top/ 25° Bottom case has mostly constant and attached flow (Fig. 49 (xxi and xxiv)) because it has the lowest pitch angle in the lower half among the three cases.

Finally, for azimuths 280° to 300°, the lift coefficient continues to decrease in magnitude for all three cases ((Fig. 47 (xxv – xxxiii)). The drag also increases until it peaks at 290° azimuth, and then decreases for the remainder of the cycle ((Fig. 48 (xxv – xxxiii)). For the 15° Top/ 45° Bottom case, the vortex is still developing at the 280° azimuth, but is fully separated from the blade from 290° to 300° (Fig. 49 (xxv, xxvii, xxxi)), which is reflective of the peak and eventual decrease of the drag coefficient for this range. The flow for the 35° Top/ 25° Bottom case remains mostly attached throughout, with the exception of the 290° azimuth where the drag is maximum and there is slight

trailing edge separation (Fig. 49 (xxvii, xxx, xxxiii)). The symmetric pitching case displays a very similar pattern, with the vortex being fully separated at the 290° azimuth, but fully attached flow by 300° (Fig. 49 (xxvi, xxix, xxxii)).

It is clear from these asymmetric pitching results that, once again, the dynamic stall process is highly dependent on the virtual camber effect and blade pitch angle. As mentioned in the previous section, the most aerodynamically efficient case of the three examined is the 35° Top/ 25° Bottom case. In the upper half, the lift coefficient was largest, but did not have a very large drag coefficient when compared to the other cases. This is because, as seen from the flowfield (Fig. 49 (iii, vi, ix, and xii)), even though the flow separated from the leading edge it was getting reattached. Furthermore, in the lower half where the blade pitch angle was smaller, the lift coefficient was not significantly lower than the 15° Top/ 45° Bottom case, which had a much larger blade pitch angle. However, the drag for the 35° Top/ 25° Bottom case was almost $1/4^{th}$ of the 15° Top/ 45° Bottom case resulting in a much higher aerodynamic efficiency in the lower half. The reason for this could be clearly seen from the flowfield (Fig. 49 (xxii – xxxiii)), which shows deep stall for the 15° Top/ 45° Bottom case from azimuthal locations of 270° - 300°, however, the flow was still attached for the 35° Top/ 25° Bottom case with only minor separation at the trailing edge. All these components combined indicate that asymmetric pitching with higher pitch at the top and lower pitch at the bottom could counteract the inherent virtual camber effect and significantly improve the performance of a cyclorotor.

Comparison of Experiment and CFD for Asymmetric Pitching

Force Comparison

2D CFD simulations of the asymmetric pitch cases were conducted with the same CFD solver (OVERTURNS) mentioned in the symmetric pitch section and the results were correlated with the asymmetric pitching experimental data. The measured and CFD predicted lift and drag coefficients are plotted against the azimuth in Figure 50. The asymmetric pitching cases selected are the same as those studied in the previous section: 15° Top/ 45° Bottom (worst performance) and 35° Top/ 25° Bottom (best performance).

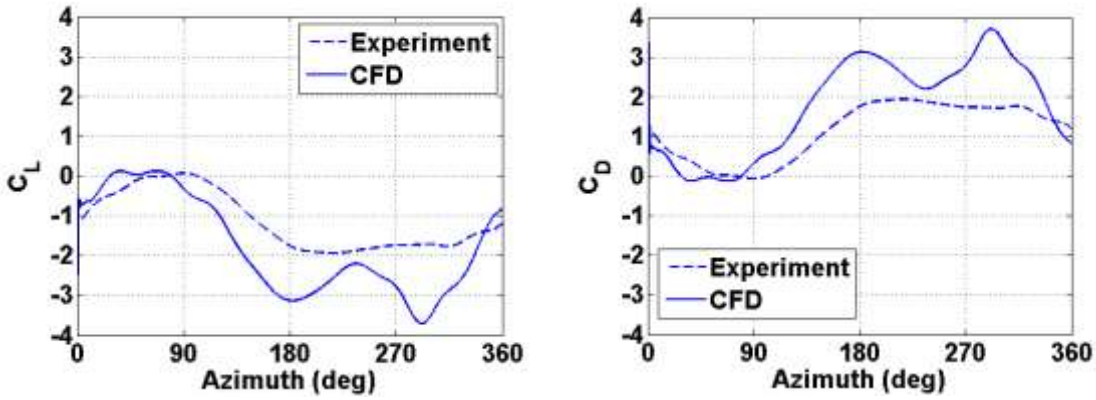

(i) C_L for 15° Top/ 45° Bottom. **(ii)** C_D for 15° Top/ 45° Bottom.

Fig. 50: Lift and drag coefficients versus azimuth for 15° Top/ 45° Bottom and 35° Top/ 25° Bottom asymmetric pitching.

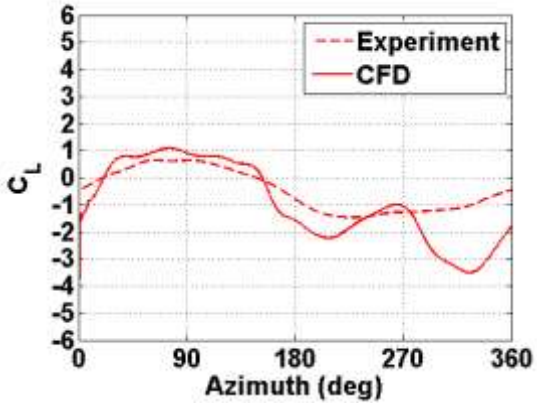

(iii) C_L for 35° Top/ 25° Bottom.

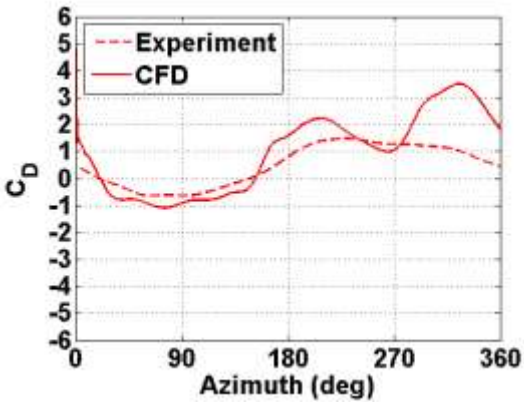

(iv) C_D for 35° Top/ 25° Bottom.

Fig. 50 (continued)

For both cases, the measured and CFD predicted forces correlate well, especially for the upper half of the trajectory. In the lower half, CFD appears to overpredict the forces, which is similar to what was observed for the symmetric pitching comparison as well. The reasons for the differences between the two are not full identified at this point, but are in the process of being investigated.

Flowfield Comparison

The next step was to compare the CFD predicted flowfield with the PIV measured flowfield at the same key azimuthal locations that were studied in the previous section. Fig. 51 shows the comparison for the 15° Top/ 45° Bottom case at azimuthal locations of 80°, 90°, 100°, 110°, 240°, 250°, 260°, 270°, 280°, 290°, and 300°.

PIV **CFD**

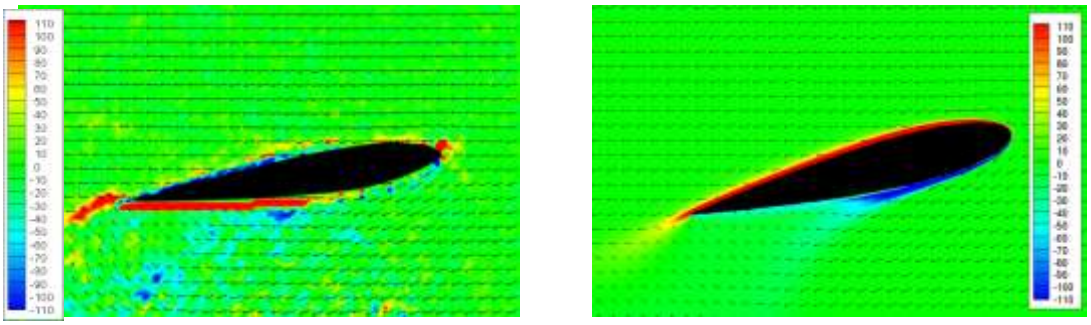

(i) Ψ = 80° for PIV **(ii) Ψ = 80° for CFD**

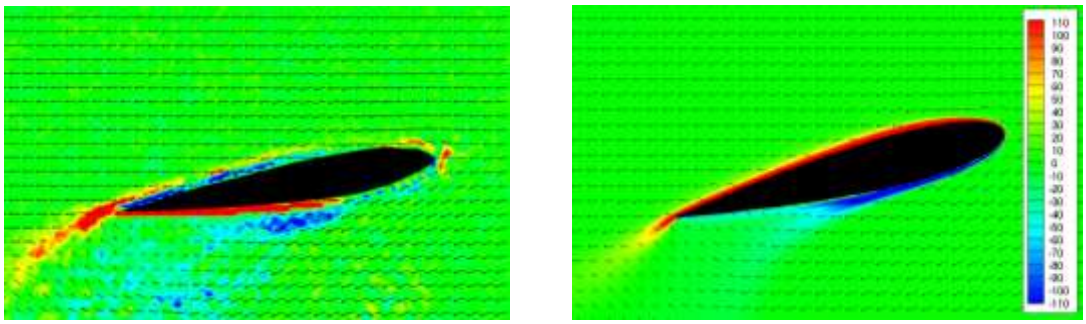

(iii) Ψ = 90° for PIV **(iv) Ψ = 90° for CFD**

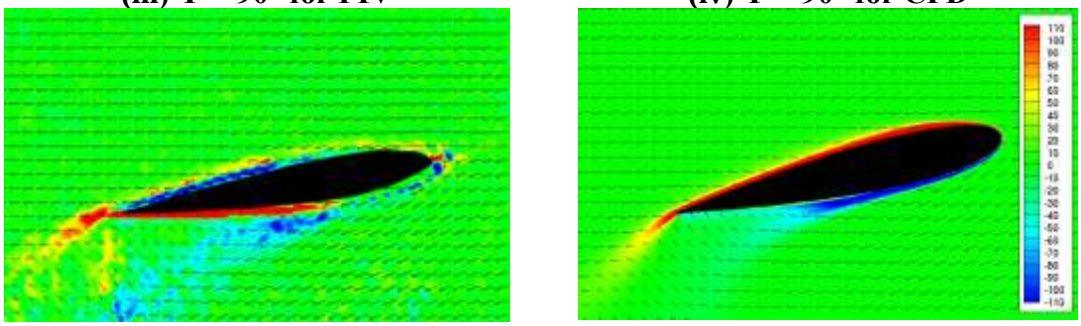

(v) Ψ = 100° for PIV **(vi) Ψ = 100° for CFD**

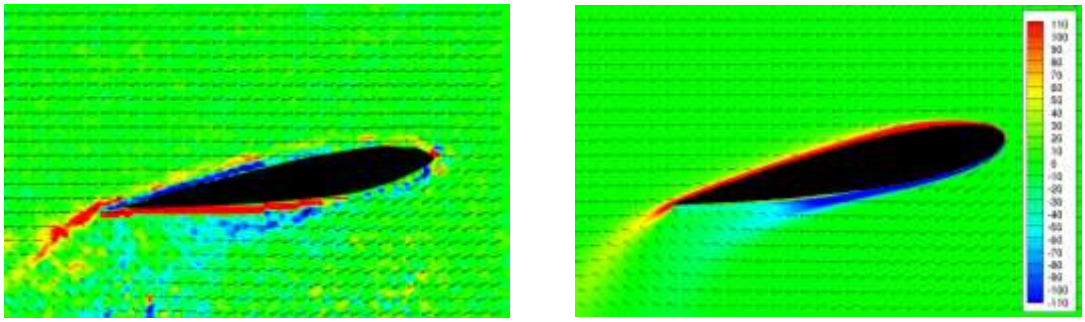

(vii) Ψ = 110° for PIV **(viii) Ψ = 110° for CFD**

Fig. 51: PIV versus CFD flowfield for 15° Top/ 45° Bottom.

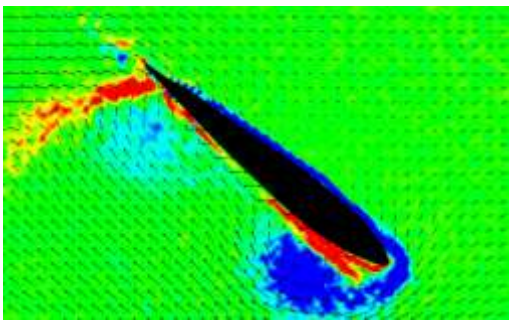

(ix) Ψ = 240° for PIV

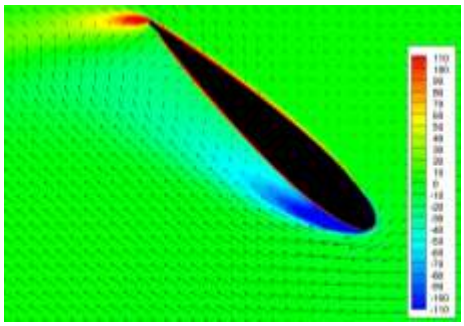

(x) Ψ = 240° for CFD

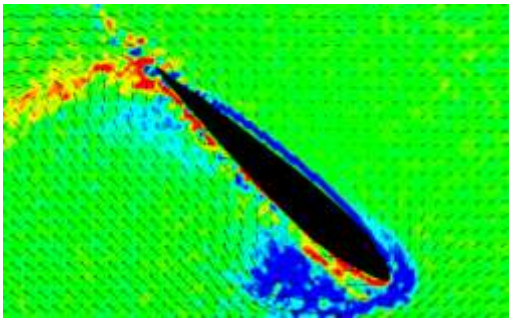

(xi) Ψ = 250° for PIV

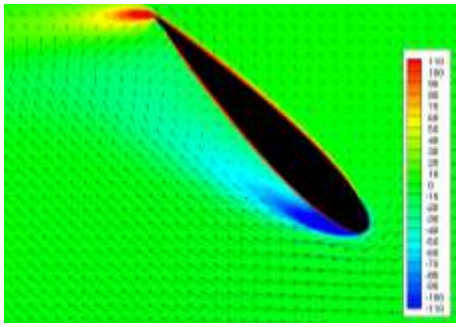

(xii) Ψ = 250° for CFD

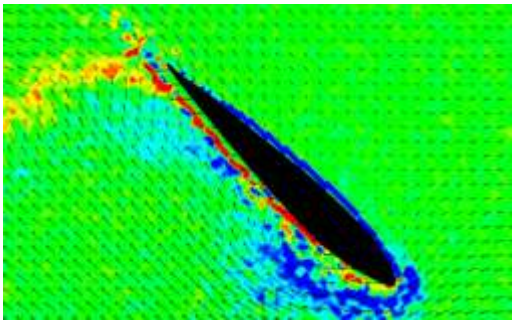

(xiii) Ψ = 260° for PIV

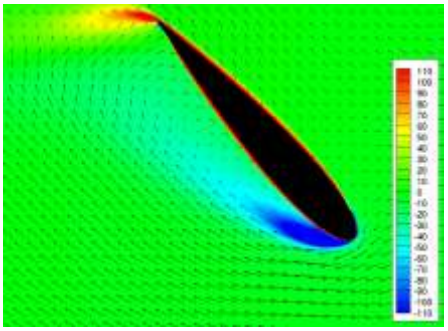

(xiv) Ψ = 260° for CFD

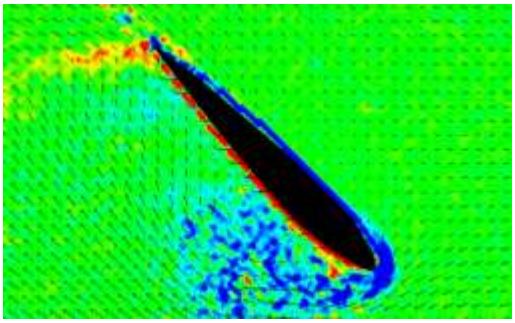

(xv) Ψ = 270° for PIV

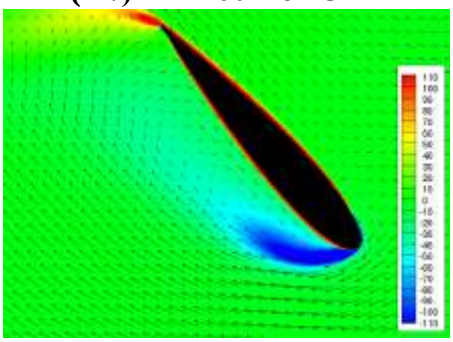

(xvi) Ψ = 270° for CFD

Fig. 51 (continued)

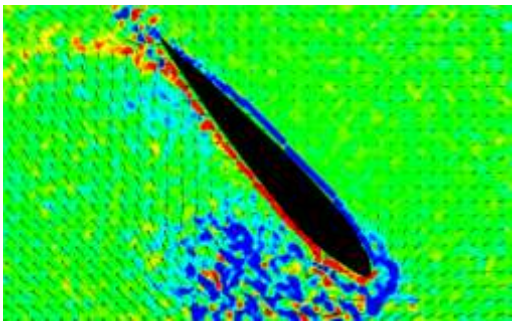

(xvii) Ψ = 280° for PIV

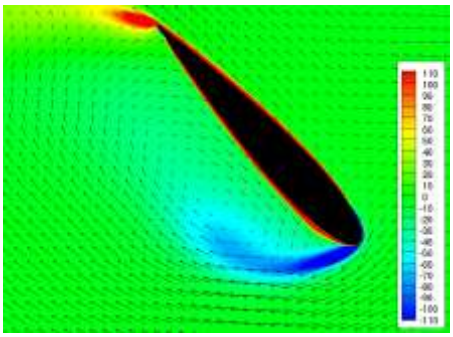

(xviii) Ψ = 280° for CFD

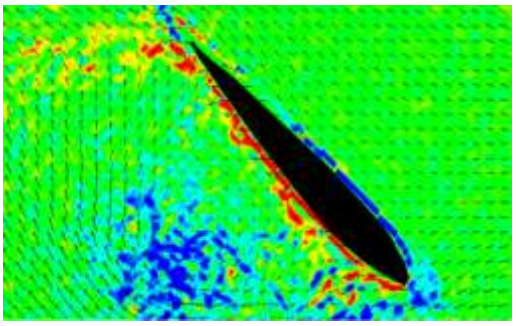

(xix) Ψ = 290° for PIV

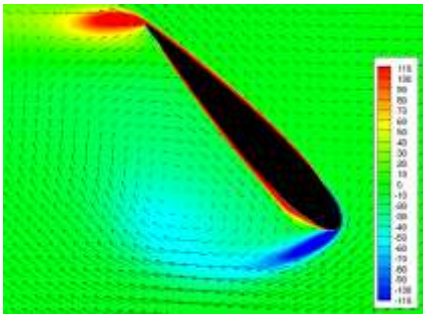

(xx) Ψ = 290° for CFD

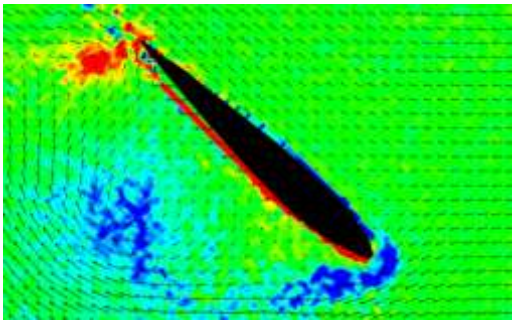

(xxi) Ψ = 300° for PIV

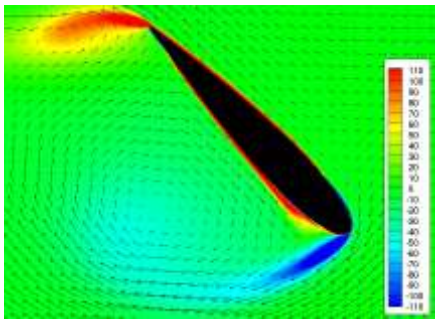

(xxii) Ψ = 300° for CFD

Fig. 51 (continued)

In the upper half, the PIV and CFD predicted flowfield solutions correlate well. The flow is attached throughout and the magnitudes of vorticity are very similar for both (Figs. 51 (i – viii). In the lower half beginning at 240°, a leading edge vortex is developing on the bottom of the blade (Figs. 51 (ix – xxii)). Both CFD and PIV capture the vortex

growth, shedding, and separation over the blade. The CFD vortex appears to be slightly smaller compared to the experiment.

The comparison for the 35° Top/ 25° Bottom case is shown in Fig. 52 below. Similarly, the azimuthal locations of 80°, 90°, 100°, 110°, 240°, 250°, 260°, 270°, 280°, 290°, and 300° are displayed for both the PIV measured and CFD predicted flowfields.

PIV **CFD**

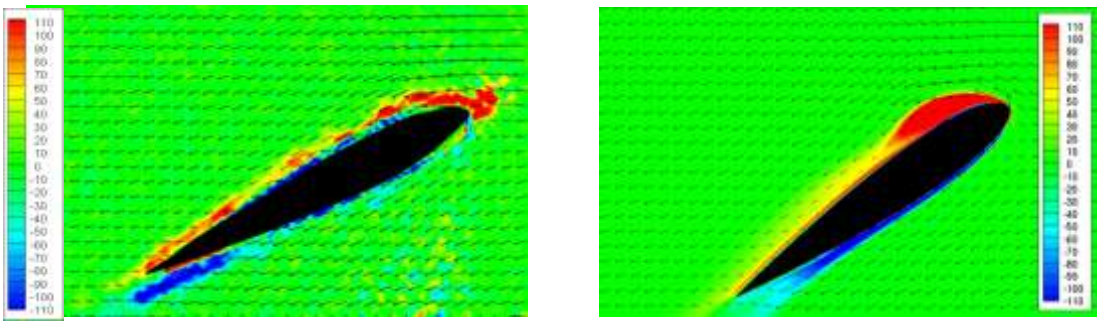

(i) Ψ = 80° for PIV **(ii) Ψ = 80° for CFD**

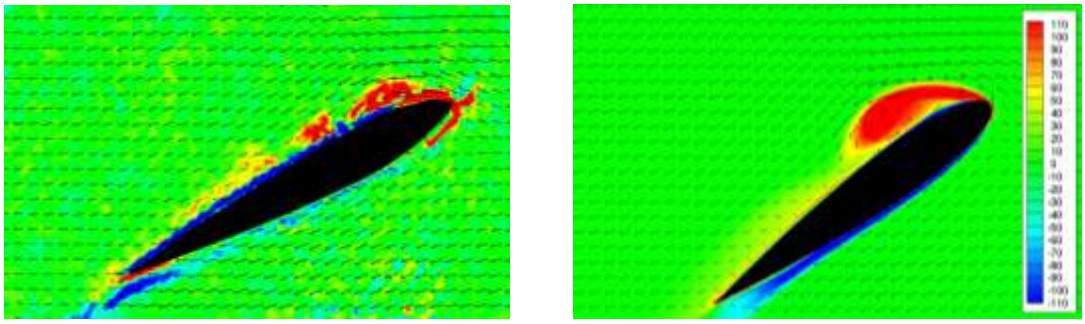

(iii) Ψ = 90° for PIV **(iv) Ψ = 90° for CFD**

Fig. 52: PIV versus CFD flowfield for 35° Top/ 25° Bottom.

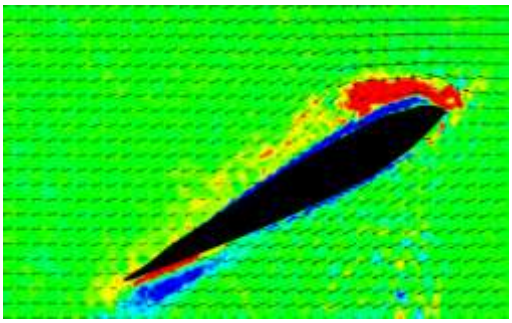

(v) Ψ = 100° for PIV

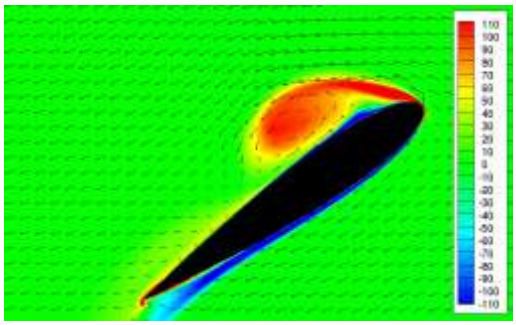

(vi) Ψ = 100° for CFD

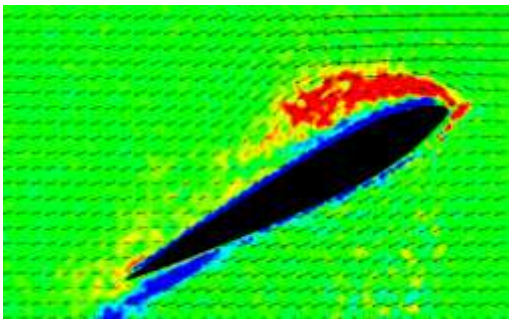

(vii) Ψ = 110° for PIV

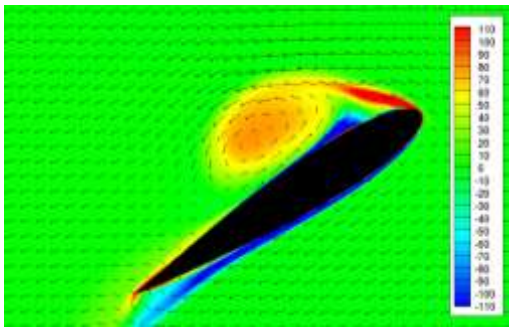

(viii) Ψ = 110° for CFD

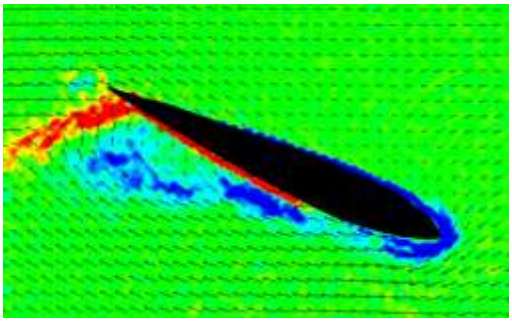

(ix) Ψ = 240° for PIV

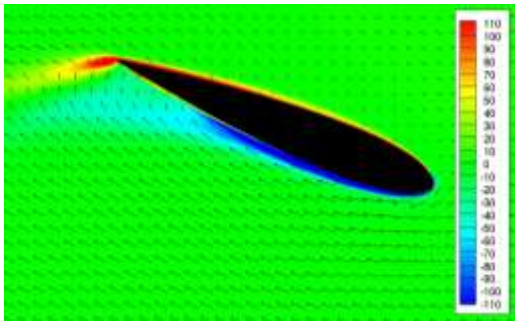

(x) Ψ = 240° for CFD

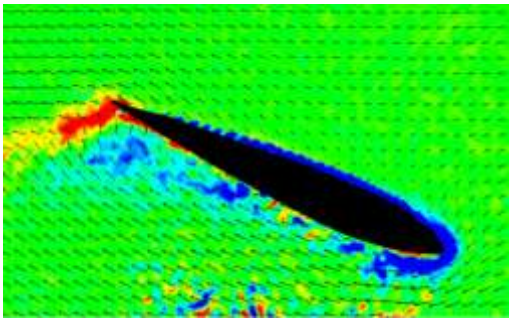

(xi) Ψ = 250° for PIV

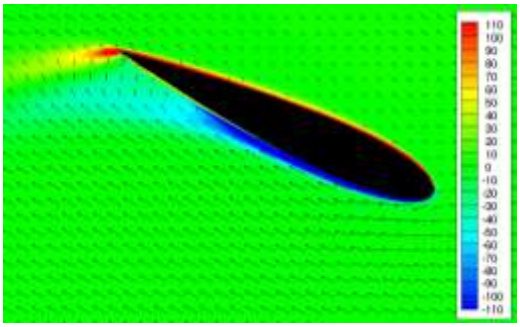

(xii) Ψ = 250° for CFD

Fig. 52 (continued)

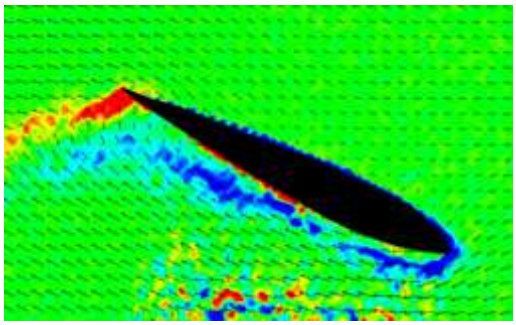

(xiii) Ψ = 260° for PIV

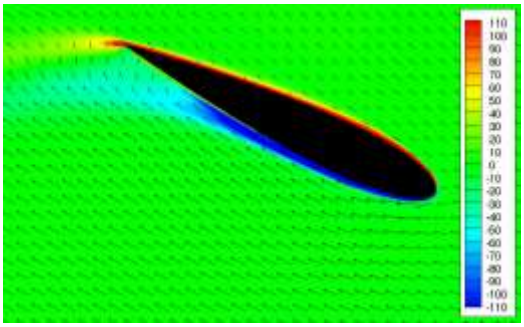

(xiv) Ψ = 260° for CFD

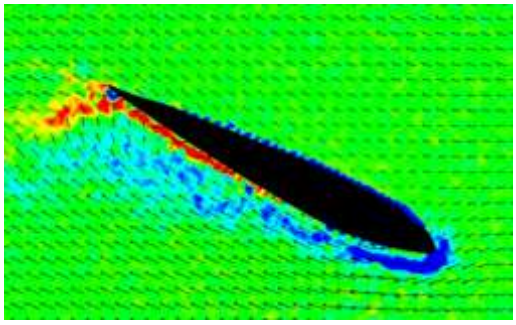

(xv) Ψ = 270° for PIV

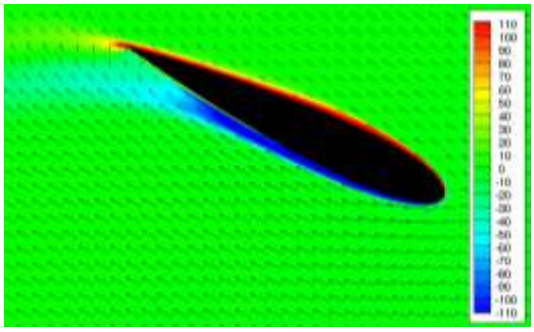

(xvi) Ψ = 270° for CFD

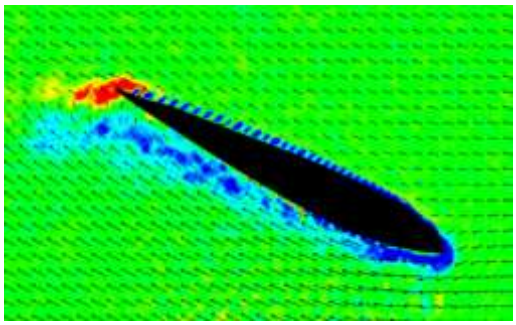

(xvii) Ψ = 280° for PIV

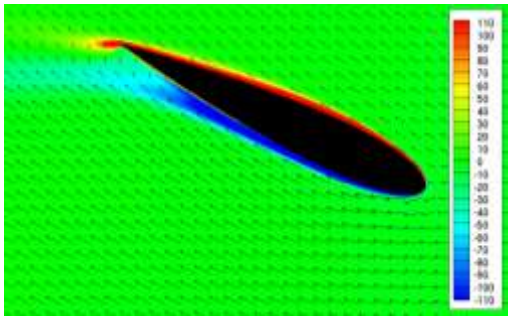

(xviii) Ψ = 280° for CFD

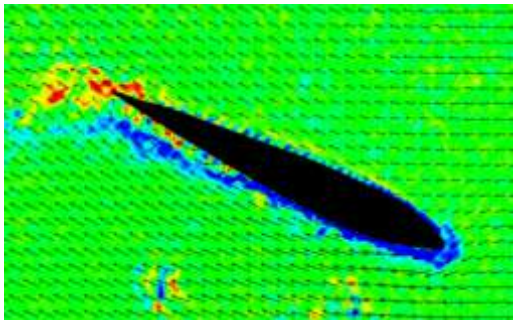

(xix) Ψ = 290° for PIV

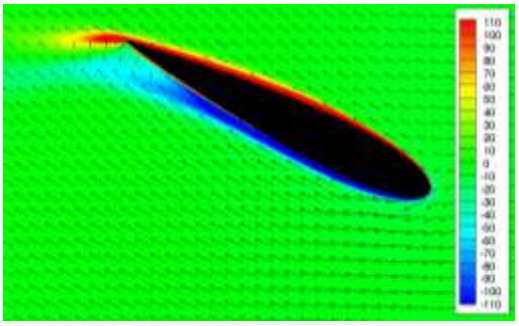

(xx) Ψ = 290° for CFD

Fig. 52 (continued)

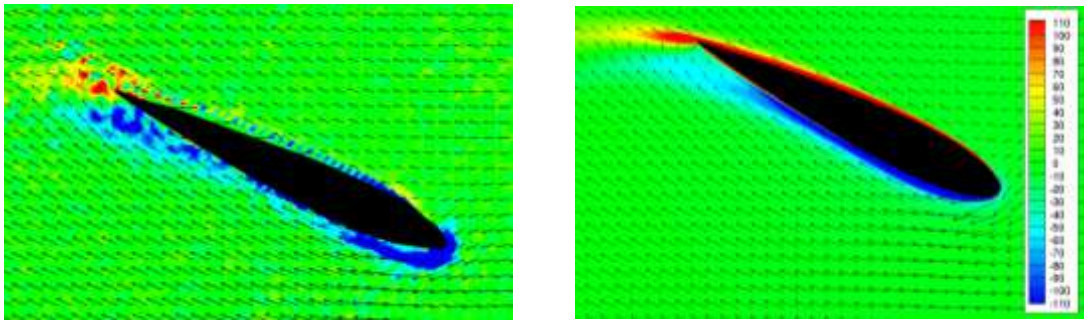

(xxi) Ψ = 300° for PIV **(xxii) Ψ = 300° for CFD**

Fig. 52 (continued)

From 80° - 110°, a small leading edge vortex is seen developing on the leading edge (Figs. 52 (i – viii)). This development is captured by both PIV and CFD, with the CFD showing a vortex that is slightly larger in size. In the lower half from 240° to 270°, the PIV measured flowfield shows mild flow separation at the leading edge and then flow re-attachment at the trailing edge (Figs. 52 (ix, xi, xiii, xv)). The CFD predicted flowfield shows only attached flow over the blade for this range (Figs. 52 (x, xii, xiv, xvi)). Again, this discrepancy is mirrored in the lift and drag coefficients (Figs. 50 (iii – iv)), where the CFD overpredicts the lift and drag in the lower half for reasons yet to be identified.

Reynolds Number Effect Experimental Results

The last experimental analysis to be discussed is regarding the effect of Reynolds number on both static and dynamic pitch cases.

Static Pitch Case

The static lift and drag coefficients as a function of the static pitch angle have been plotted for three different Reynolds numbers in Figs. 53 and 54. The Reynolds numbers include 9,232, 18,465, and 27,697, which correspond to 20, 40, and 60 RPM, respectively.

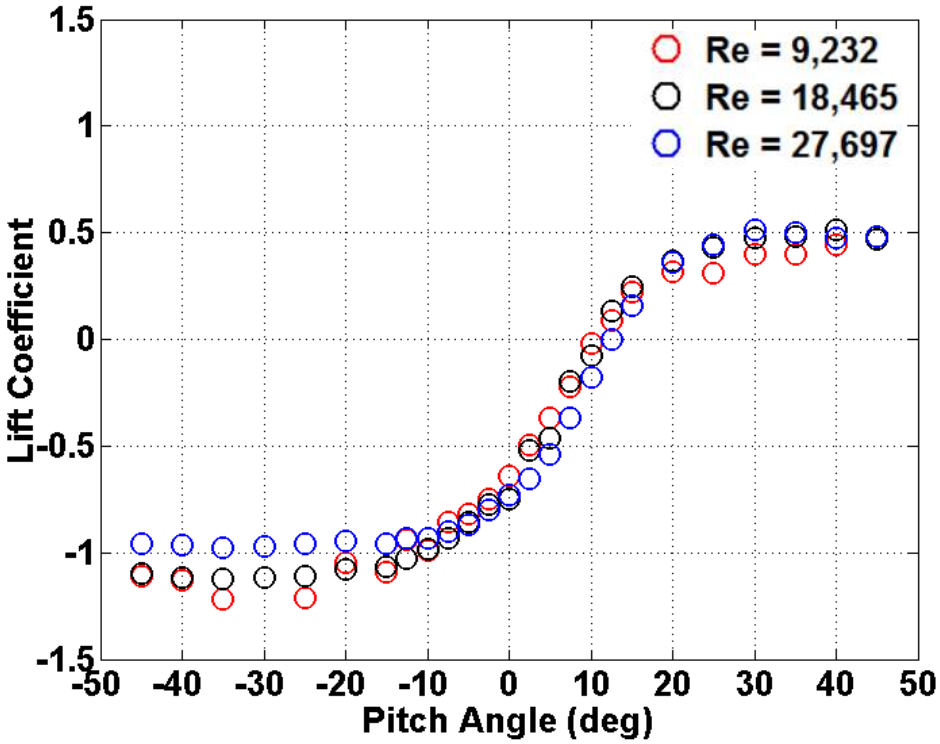

Fig. 53: Lift coefficient versus fixed pitch angle for different Reynolds numbers and static blade pitch angles.

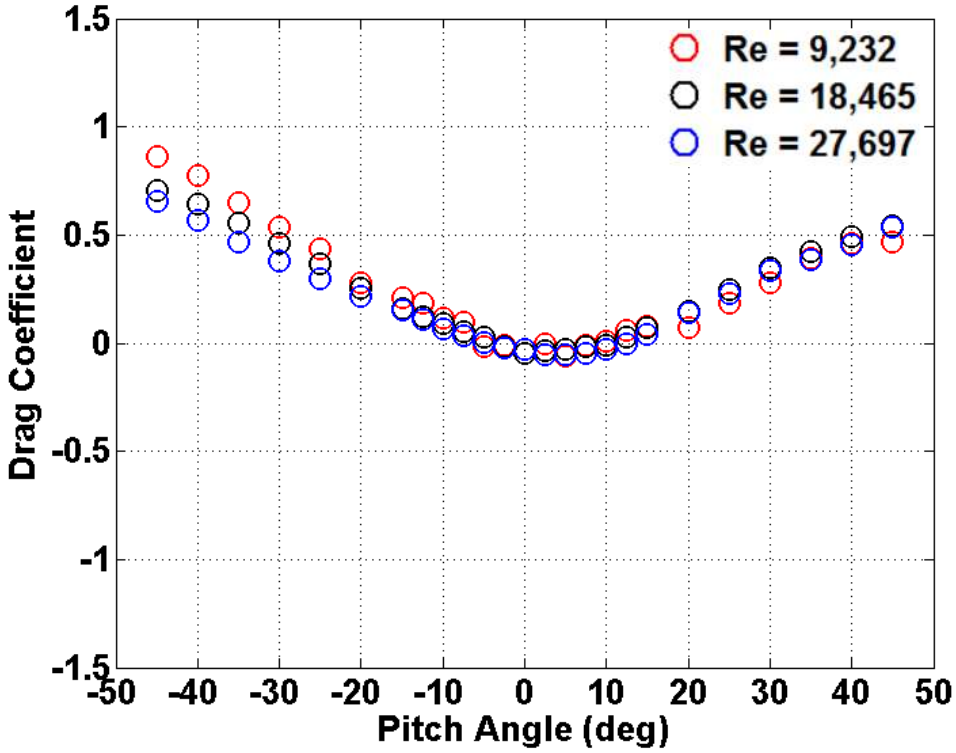

Fig. 54: Drag coefficient versus fixed pitch angle for different Reynolds numbers and static blade pitch angles.

The static results are similar in magnitude for all three Reynolds numbers. The largest deviation appears for negative pitch angles, where the lift and drag coefficients are largest for Re = 9,232 (Figs. 53 and 54). This is expected because of the more prevalent effect of viscosity at lower Reynolds numbers leading to the formation of laminar separation bubbles and more skin-friction drag.

To complement the force measurements at different Reynolds numbers, measured flowfield for several static blade pitch angles are shown in Fig. 55. The static blade pitch angles presented include 10°, 25°, and 45° at the three different Reynolds numbers.

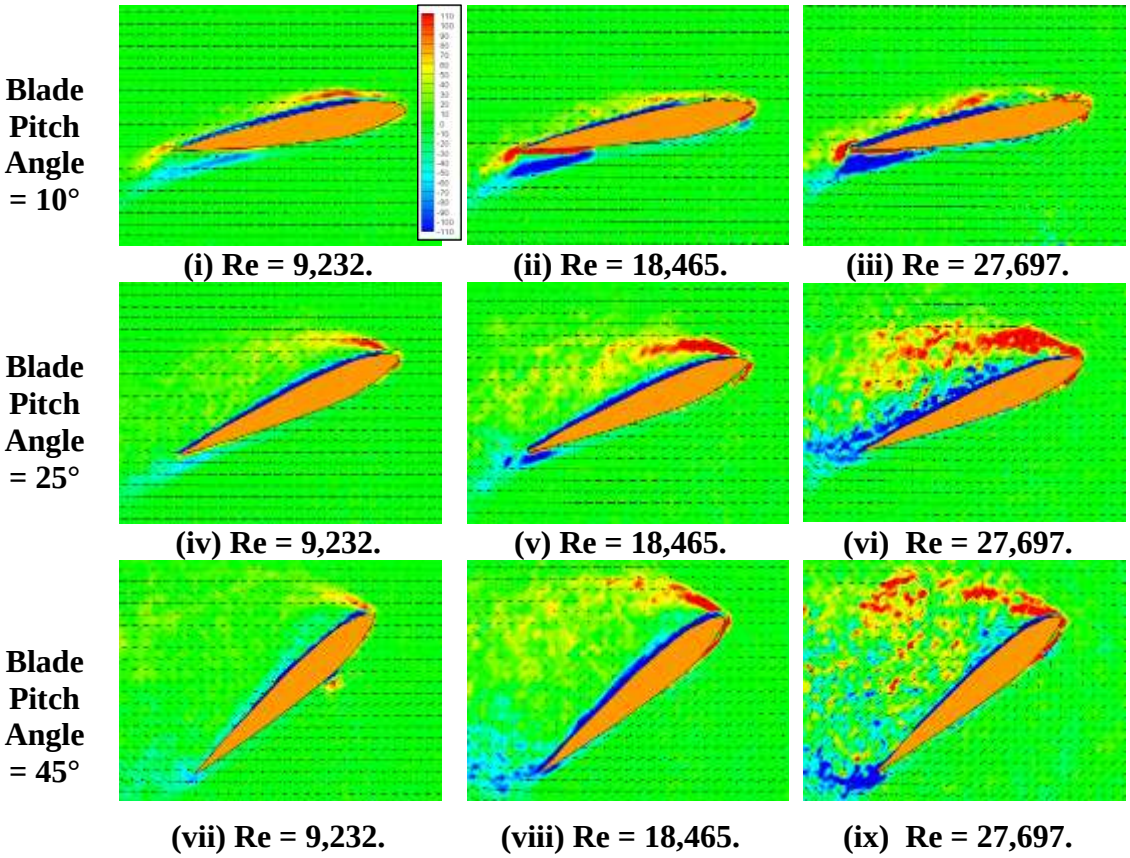

Fig. 55: PIV measured flow velocity vectors and vorticity contours for different Reynolds numbers and static blade pitch angles.

From Fig. 55 it can be seen that for a static pitch angle of 10°, the flow remains mostly attached at all the three Reynolds numbers (Fig. 55 (i – iii)) without any significant differences. However, at higher pitch angles (Fig. 55 (iv – ix)), the flow separates from the leading edge; however, there is more vorticity being shed from both leading and trailing edges with increasing Reynolds number.

Dynamic Pitch Case

The dynamic lift coefficients for the dynamic pitching cases of ±15°, ±30°, and ±45° are plotted for Re = 9,232, Re = 18,465, and Re = 27,697 in Fig. 56. For the ±15° pitching case, the Re = 9,232 case produces the maximum lift coefficient in the upper half, and maximum for the drag coefficient during the entire cycle (Fig. 56 (i – ii)).

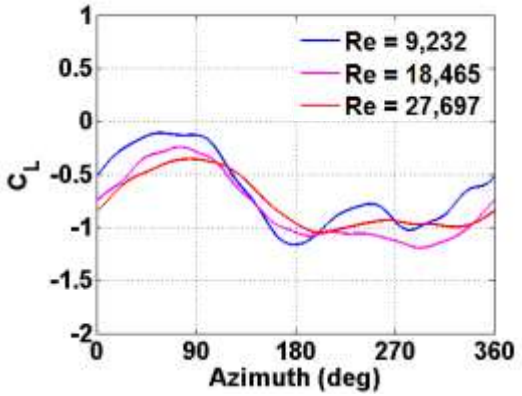

(i) C_L for ±15° pitching.

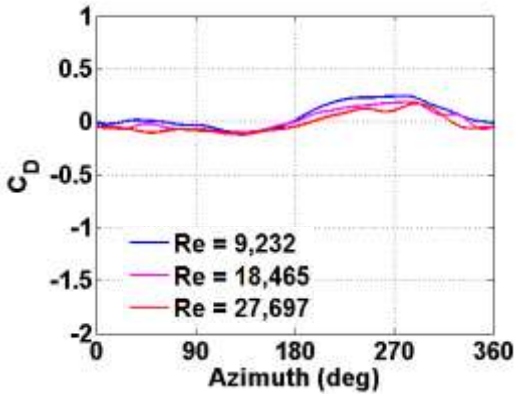

(ii) C_D for ±15° pitching.

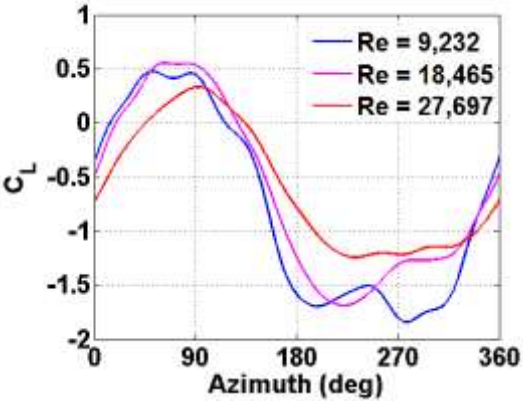

(iii) C_L for ±30° pitching.

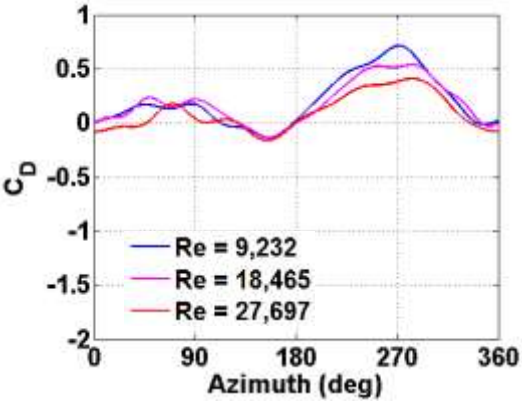

(iv) C_D for ±30° pitching.

Fig. 56: Lift and drag coefficients versus azimuth for 15° Top/ 45° Bottom and 35° Top/ 25° Bottom asymmetric pitching.

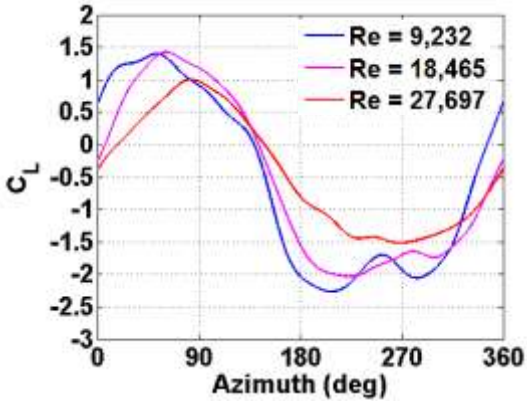

(v) C_L for ±45° pitching.

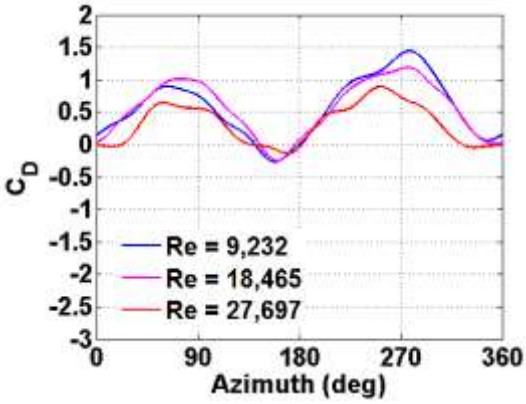

(vi) C_D for ±45° pitching.

Fig. 56 (continued)

In the ±30° pitching case, the Re = 18,465 case results in maximum lift and drag in the upper half of the cycle (Fig. 56 (iii – iv)). However, the Re = 9,232 case appears to dominate the lift and drag in the lower half. This is reflective of the dynamic stall process being distinctive in the upper and lower halves of the azimuth. In the previous sections, it was found that the dynamic stall process differs in the two halves due to an interplay of blade pitch angle and virtual camber. For the ±45° pitching case, the same pattern is seen where the Re = 18,465 case produces the greatest lift and drag in the upper half, and the Re = 9,232 case produces the greatest lift and drag in the lower half (Fig. 56 (v – vi)). From these results, it is evident that the Reynolds number also effects the dynamic stall process, and thus, the force produced by the blades.

CHAPTER VI

CONCLUSIONS

This thesis provides an in-depth understanding of the unsteady aerodynamic mechanisms on a cyclorotor blade operating at ultra-low Reynolds numbers (Re~18,000). This is accomplished by utilizing a combination of force and flowfield measurements in conjunction with CFD simulations. This is the first time the instantaneous blade fluid dynamic forces on a cyclorotor blade were measured, which, along with PIV-based high resolution flowfield measurements around the blade at different azimuthal locations, revealed the key fluid dynamic mechanisms acting on the blade. A 2D CFD analysis of the cyclorotor was developed, which correlated well with experiments for both the force and flowfield. Studies were performed with static pitch, and dynamic blade pitching for symmetric and asymmetric kinematics. Direct comparison of the static and dynamic pitch experimental results helped isolate the unsteady aerodynamic phenomena from the steady effects.

Specific conclusions from this study are as follows:

1. Large dynamic virtual camber induced by the inherent flow curvature and blade pitch rate caused asymmetry in lift and drag coefficients between positive and negative pitch for both the static and dynamic pitching cases.
2. The unsteady blade force coefficients were almost double the static ones clearly indicating the role of unsteady aerodynamic mechanisms on the force production on cyclorotor blades. This explains the ability of a cyclorotor to produce large

thrust at relatively lower rotational speeds, which was a key inference from the previous performance studies.

3. For the dynamic case, the blade lift coefficient monotonically increased even up to ±45° pitch amplitude due to dynamic stall phenomenon, which kept the flow attached until higher pitch angles. On the other hand, for the static case, the flow separated from the leading edge after around 15° with a large laminar separation bubble (LSB) and eventually completely separating at higher pitch angles.
4. The CFD flow solution and PIV measured flowfield correlated very well and both showed the formation and shedding of strong leading edge or dynamic stall vortices, especially at higher pitch amplitudes, which is the reason for the stall delay and force enhancement.
5. Dynamic stall processes in the upper and lower halves of the circular blade trajectory were completely different because of the reversal of the virtual blade camber from upper to lower half.
6. The measured resultant forces were mostly normal to the chord for the dynamic pitch cases indicating that the pressure force, as opposed to viscous force, is dominant on a cyclorotor blade (even at these ultra-low Reynolds numbers).
7. The power required for blade rotation (rather than pitching power) is the significant component of the total power required for dynamic pitching cyclorotor blade.
8. The cyclorotor figure of merit (*FM*) drops at higher pitch amplitudes due to higher dynamic drag coefficients.

9. For asymmetric pitching, the 35° Top/ 25° Bottom case required the least power, evidenced by the large lift in the upper half, and relatively small drag produced in the lower half. The 15° Top/ 45° Bottom case, on the other hand, required the most power. This was apparent in the lower half, especially, where the drag was 4 times that of the drag for the 35° Top/ 25° Bottom case. It was concluded that asymmetric pitching with higher pitch at the top and lower pitch at the bottom could counteract the inherent virtual camber effect and significantly improve the performance of a cyclorotor.
10. The CFD predicted forces and flowfield correlated well with the measured forces and PIV measured flowfield for asymmetric pitching. There were some discrepancies in the lower half where CFD seemed to overpredict the forces. The reasons for this are still being investigated.
11. Reynolds number effects dynamic stall processes and thus the force produced by the blades.

REFERENCES

1. Pines and Bohorquez, "Challenges Facing Future Micro-Air Vehicle Development," *Journal of Aircraft*, Vol. 43, No. 2, April 2006, pp. 290-305.
2. Hein, B., and Chopra, I., "Hover Performance of a Micro Air Vehicle: Rotors at Low Reynolds Number," *Journal of American Helicopter Society*, Vol. 52, No. 3, July 2007, pp. 254–262.
3. Benedict, M., "Fundamental Understanding of the Cycloidal-Rotor Concept for Micro Air Vehicle Applications," Ph.D Thesis, Department of Aerospace Engineering, University of Maryland College Park, December 2010.
4. Benedict, M., Ramasamy, M., Chopra, I., and Leishman, J. G., "Performance of a Cycloidal Rotor Concept for Micro Air Vehicle Applications," *Journal of the American Helicopter Society*, Vol. 55, No. 2, April 2010, pp. 022002-1 - 022002-14.
5. Benedict, M., Ramasamy, M., and Chopra, I., "Improving the Aerodynamic Performance of Micro-Air-Vehicle-Scale Cycloidal Rotor: An Experimental Approach," *Journal of Aircraft*, Vol. 47, No. 4, July-August 2010, pp. 1117 – 1125.
6. Benedict, M., Jarugumilli, T., and Chopra, I., "Experimental Optimization of MAV-Scale Cycloidal Rotor Performance," *Journal of the American Helicopter Society*, Vol.56, No.2, April2011,pp.022005-1 -022005-11.
7. Benedict, M., Jarugumilli, T., and Chopra, I., "Effect of Rotor Geometry and Blade Kinematics on Cycloidal Rotor Hover Performance," *Journal of Aircraft*, Vol. 50, No. 5, 2013, pp. 1340 – 1352.

8. Benedict, M., Jarugumilli, T., Lakshminarayan, V. K., and Chopra, I., "Effect of Flow Curvature on the Forward Flight Performance of a MAV-Scale Cycloidal Rotor," *AIAA Journal*, Vol. 52, No. 6, 2014, pp. 1159 – 1169.
9. Lind, A. H., Jarugumilli, T., Benedict, M., Lakshminarayan, V. K., Jones, A. R., and Chopra, I., "Flowfield studies on a micro-air-vehicle-scale cycloidal rotor in forward flight," *Experiments in Fluids*, Vol. 55, November 2014, pp. 1 – 17.
10. Jarugumilli, T., Benedict, M., and Chopra, I., "Wind Tunnel Studies on a Micro Air Vehicle-Scale Cycloidal Rotor," *Journal of the American Helicopter Society*, Vol. 59, No. 2, April 2014, pp. 1 – 10.
11. Benedict, M., Mattaboni, M.,Chopra, I., and Masarati, P.,"Aeroelastic Analysis of a Micro-Air-Vehicle-Scale Cycloidal Rotor in Hover," *AIAA Journal*, Vol. 49, No. 11, November 2011, pp. 2430 – 2443.
12. Benedict, M., Gupta, R., and Chopra, I., "Design, Development and Open-Loop Flight Testing of a Twin-Rotor Cyclocopter Micro Air Vehicle," *Journal of the American Helicopter Society*, Vol. 58, No. 4, October 2013, pp. 1 – 10.
13. Elena, S., Hrishikeshavan, V., Benedict, M., Yeo, D., and Chopra, I., "Development of Control Strategies and Flight Testing of a Twin-Cyclocopter in Forward Flight," Proceedings of the 70th Annual National Forum of the American Helicopter Society, Montreal, Quebec, Canada, May 20–22, 2014.
14. Benedict, M., Mullins, J., Hrishikeshavan, V., and Chopra, I., "Development of a Quad Cycloidal-Rotor Unmanned Aerial Vehicle," *Journal of the American Helicopter Society*, Vol. 61, No. 2, April 2016, pp. 1 – 12.

15. Zachary, H., A., Benedict, M., Hrishikeshavan, V., and Chopra, I., "Design, Development, and Flight Test of a Small-Scale Cyclogyro UAV Utilizing a Novel Cam-Based Passive Blade Pitching Mechanism," *International Journal of Micro Air Vehicles,* Vol. 5, No. 2, June 2013, pp. 145 – 162.
16. Lakshminarayan, V. K., "Computational Investigation of Microscale Coaxial Rotor Aerodynamics in Hover," Ph.D. Thesis, Department of Aerospace Engineering, University of Maryland College Park, 2009.
17. Pulliam, T., Chaussee, D., "A Diagonal Form of an Implicit Approximate Factorization Algorithm," *Journal of Computational Physics,* Vol. 39, No. 2, 1981, pp. 347–363.
18. Van Leer, B., "Towards the Ultimate Conservative Difference Scheme V. A Second-Order Sequel to Godunov's Method," *Journal of Computational Physics,* Vol. 135, No. 2, 1997, pp. 229–248.
19. Roe, P., "Approximate Riemann Solvers, Parameter Vectors and Difference Schemes," *Journal of Computational Physics,* Vol. 135, No. 2, 1997, pp. 250–258.
20. Koren, B., "Multigrid and Defect Correction for the Steady Navier–Stokes Equations", Proceedings of the 11th International Conference on Numerical Methods in Fluid Dynamics, Willamsburg, VA, June 1988.
21. Turkel, E., "Preconditioning Techniques in Computational Fluid Dynamics," *Annual Review of Fluid Mechanics,* Vol. 31, 1999, pp. 385–416.

22. Spalart, P.R., Allmaras, S.R. “A One-equation Turbulence Model for Aerodynamics Flows,” Proceedings of the 30th AIAA Aerospace Sciences Meeting and Exhibit, Reno, NV, January 6–9, 1992.
23. Halder, A., Walther, C., and Benedict, M., “Unsteady Hydrodynamic Modeling of Cycloidal Propeller,” To appear in the Proceedings of the Fifth International Symposium on Marine Propulsors, Helsinki, Finland, June 12 –15, 2017.